Doctoral Dissertations and Master's Theses

Summer 7-2021

Additively Manufactured Dielectric Elastomer Actuators: Development and Performance Enhancement

Stanislav Sikulskyi
Embry-Riddle Aeronautical University

Follow this and additional works at: https://commons.erau.edu/edt

Part of the Structures and Materials Commons

Scholarly Commons Citation

ADDITIVELY MANUFACTURED DIELECTRIC ELASTOMER ACTUATORS:

DEVELOPMENT AND PERFORMANCE ENHANCEMENT

By

Stanislav Sikulskyi

A Dissertation Submitted to the Faculty of Embry-Riddle Aeronautical University

In Partial Fulfillment of the Requirements for the Degree of

Doctor of Philosophy in Aerospace Engineering

July 2021

Embry-Riddle Aeronautical University

Daytona Beach, Florida

ADDITIVELY MANUFACTURED DIELECTRIC ELASTOMER ACTUATORS:
DEVELOPMENT AND PERFORMANCE ENHANCEMENT

By

Stanislav Sikulskyi

This Dissertation was prepared under the direction of the candidate's Dissertation Committee Chair, Dr. Daewon Kim, Department of Aerospace Engineering, and has been approved by the members of the Dissertation Committee. It was submitted to the Office of the Senior Vice President for Academic Affairs and Provost, and was accepted in the partial fulfillment of the requirements for the Degree of Philosophy in Aerospace Engineering.

DISSERTATION COMMITTEE

Daewon Kim Digitally signed by Daewon Kim Date: 2021.08.04 12:05:57 -04'00'	**Marwan Al-Haik** Digitally signed by Marwan Al-Haik DN: cn=Marwan Al-Haik, o=Embry-Riddle Aeronautical University, ou=Aerospace Engineering, email=alhaikm@erau.edu, c=US Date: 2021.08.04 21:19:27 -04'00'
Chairman, Dr. Daewon Kim	Member, Dr. Marwan Al-Haik
Sirish Namilae Digitally signed by Sirish Namilae Date: 2021.08.04 13:55:38 -04'00'	**Mandar D. Kulkarni** Digitally signed by Mandar D. Kulkarni Date: 2021.08.04 15:09:16 -04'00'
Member, Dr. Sirish Namilae	Member, Dr. Mandar Kulkarni
Eduardo A. Rojas Digitally signed by Eduardo A. Rojas Date: 2021.08.04 12:32:10 -04'00'	**Foram Madiyar** Digitally signed by Foram Madiyar Date: 2021.08.04 15:32:46 -04'00'
Member, Dr. Eduardo Rojas	Member, Dr. Foram Madiyar
Sirish Namilae Digitally signed by Sirish Namilae Date: 2021.08.05 09:54:06 -04'00'	08/05/2021
Graduate Program Coordinator, Dr. Sirish Namilae	Date
Maj Mirmirani Digitally signed by Maj Mirmirani Date: 2021.08.05 12:22:29 -04'00'	08/05/2021
Dean of the College of Engineering, Dr. Maj Mirmirani	Date
Lon Moeller Digitally signed by Lon Moeller Date: 2021.08.05 13:17:11 -04'00'	08/05/2021
Senior Vice President for Academic Affairs and Provost Lon Moeller, J.D.	Date

ACKNOWLEDGEMENTS

ABSTRACT

The recently emerging and actively growing areas of soft robotics and morphing structures promise endless opportunities in a wide range of engineering fields, including biomedical, industrial, and aerospace. Soft actuators and sensors are essential components of any soft robot or morphing structure. Among the utilized materials, dielectric elastomers (DEs) are intrinsically compliant, high energy density polymers with fast and reversible electromechanical response. Additionally, the electrically driven work principle allows DEs to be distributed in a desired fashion and function locally with minimum interference. Thus, a great effort is being made towards utilizing additive manufacturing (AM) technologies to fully realize the potential of DE soft actuators and sensors. While soft sensors have received more attention and development due to their simpler implementation, DE actuators (DEAs) set stricter AM and electrode material requirements. DEAs' layered structure, compliant nature, and susceptibility to various defects make their manufacturability challenging, especially for non-trivial biomimetic soft robotics geometries. This dissertation comprehensively analyzes DE materials' transition into a soft actuator using AM to facilitate effective DEA soft actuator fabrication. Closely interrelated fabrication techniques, material properties, and DEA geometries are analyzed to establish a fundamental understanding of how to implement high-quality DEA soft actuators. Furthermore, great attention is paid to enhancing the performance of printed DEAs through developing printable elastomer and electrode materials with improved properties. Lastly, performance enhancement is approached from the design point of view by developing a novel 3D printable DEA configuration that actuates out-of-plane without stiffening elements.

TABLE OF CONTENTS

LIST OF FIGURES

Figure   Page

LIST OF TABLES

ABBREVIATIONS

2.5D	two and a half dimensional
3D	three dimensional
4D	four dimensional
AC	alternating current
AM	additive manufacturing
$BaTiO_3$	barium titanate
BC	boundary conditions
BoPET	biaxially-oriented polyethylene terephthalate
CCTO	copper calcium titanate
CG	carbon grease
CNT	carbon nanotube
DC	direct current
DE	dielectric elastomer
DEA	dielectric elastomer actuator
DIW	direct ink writing
DLP	digital light processing
DMSO	dimethyl sulfoxide
EAP	electroactive polymers
EG	ethylene glycol
FDM	fused deposition modeling
FEM	finite element methods
FOM	figure of merit

LCD	liquid crystal display
MEK	methyl ethyl ketone
MUDEA	multilayer unimorph dielectric elastomer actuator
P(VDF-TrFE-CFE)	polyvinylidene fluoride terpolymer
PAni	polyaniline
PDMS	polydimethylsiloxane
PE	polyethylene
PEDOT	poly(3,4-ethylene-dioxythophene)
PEDOT:PSS	poly(3,4-ethylene-dioxythiophene):poly(styrenesulfonate)
PEG	poly(ethylene glycol)
PET	polyethylene terephthalate
PMMA	poly(methyl methacrylate)
PPy	polypyrrole
PTFE	polytetrafluoroethylene
PTh	polythiophene
RTV	room temperature vulcanizing
SD	standard deviation
SLA	stereolithography
SLS	selective laser sintering
SWCNT	single-wall carbon nanotube
TPE	thermoplastic elastomers
TPU	thermoplastic polyurethanes
UV	ultraviolet

1. Introduction

This chapter explains the motivation behind the research done on additive manufacturing (AM) of dielectric elastomer actuators (DEAs). It sets the main goals in achieving high-quality and high-performance printed soft actuators.

1.1. Motivation

Actuators are an integral part of any mechanical field. The growing demand for actuators can be deduced from their global market, which currently trends double every eight years. Hydraulic, pneumatic, electromagnetic, and piezoelectric actuators constitute a vest majority of the market. Nevertheless, in recent decades, such fields as aerospace, defense, robotics, manufacturing, and biomedical show great interest in novel technologies that can potentially revolutionize the market and lead to qualitatively new types of devices and applications. Such technologies as soft actuators and soft sensors are mainly essential for the development of recently emerged concepts of morphing structures, human-robot interaction, biomimetics, etc. (Hines, Petersen, Lum, & Sitti, 2017; Rus & Tolley, 2015).

As discussed further in the literature review of the present work, soft sensors have so far received greater interest and implementation due to their simpler transition from stiff to compliant behavior compared to actuators. Meanwhile, soft actuators can be considered an even more significant and bulkier component of functional systems, as observed from biological creatures (Rogers, 2013). A wide range of research on soft actuators has been conducted on topics related to the design of novel soft actuators, material properties, force optimization, motion, stiffness control, and applications. However, despite the considerable research interest in soft actuators, very few

technologies have been practically implemented or commercialized. The main reason

behind low implementation and commercialization is that soft actuators are expected to

perform the tasks of traditional actuators while providing outstanding performance,

satisfying reliability, long-term and stable electro-mechanical properties (John, Nadia,

Sami, & Culley, 2016; J. Kim et al., 2019). While providing unprecedented capabilities

for the mentioned concepts, soft actuators rely on advances in different areas, including

materials, manufacturing, design, modeling, and control. Considering the close

interrelation of the first three areas, they need to be studied together to establish a

fundamental understanding of how to implement high-quality DEA soft actuators.

1.1.1. Materials

An apparent requirement for a soft actuator material is its low resistance to applied

deformation. As such, soft actuators can easily undergo large deformation and experience

high strains. Thus, stretchability is a requirement often conjugated to compliance. These

two requirements severely limit the variety of appropriate actuator technologies,

particularly the conventional types. Therefore, some smart materials have gained much

attraction due to their actuation capability while being intrinsically compliant and

stretchable (J. Kim et al., 2019). Another benefit of utilizing smart materials is the ability

to miniaturize the design of the actuator without losing, or even gaining, actuation

efficiency. DEA is one of the most promising candidates suitable for soft actuators

application thanks to its highest energy density among compliant and stretchable smart

materials, fast and reversible electro-mechanical response, intensive development, and

prospective commercialization (Hines et al., 2017; Q. M. Zhang & Serpe, 2017). Hence,

DEA is chosen as a soft actuator material in this research. As DEA consists of two

materials, compliant dielectric and electrode, investigating the effects of both materials on DEA performance and improving the properties of the materials is a critically important task.

1.1.2. Manufacturing

The interest in additive manufacturing of soft actuators in this research, mainly AM of DEAs, is due to the enormous demand for rapid prototyping of soft actuators, which is attributed to several reasons. Firstly, as soft actuators are utilized in various applications, their design varies considerably across these applications. This fact requires the fabrication technique to be flexible and capable of manufacturing actuators of a broad design range. Secondly, being a novel, dynamic field, soft actuators heavily rely on experimental work, e.g., fabricating numerous designs for a single application to validate the results or find the optimum design. Thus, the fabrication technique also needs to be efficient in producing variations of actuator designs with minimum to no changes to the manufacturing process. Lastly, DEA is one of the most promising performance-wise but hard-to-fabricate smart materials due to its layered structure and softness. The vast majority of current fabrication methods for DEA soft actuators are done by hand, leading to limited and unpredictable performance (Gupta, Qin, Wang, Godaba, & Zhu, 2019; Shintake, Cacucciolo, Floreano, & Shea, 2018).

All three requirements can be fulfilled to a great degree with a reliable AM methodology that can produce high-quality soft actuators with repeatable performance. In addition, electric stimulus enables soft actuators (and sensors) to utilize multiple DEAs to function locally with minimum interference. Being able to precisely deposit materials,

AM printing unveils new possibilities for genuinely biomimetic soft actuators with embedded and distributed actuation-sensing systems (Gul et al., 2018).

Impartially, certain limitations are prone to every manufacturing technique. Thus, it is crucial to reveal these limitations for various AM methods for DEA fabrication and establish the approaches to improve manufacturing quality. Knowing the limitations, one could wisely choose and modify the selected AM technique to expedite one's research.

1.1.3. Design

While the manufacturing process plays a dominant role in producing high-quality soft actuators, DEA design considerations are also important. Appropriately designed DEA should be easily and accurately fabricated through specific AM methods and apparatus, considering the limitations, resolutions, and possible defects of various nature.

As further discussed in the literature review, the main goal of AM to result in the completed product (soft actuator) contradicts the so-called "prestretch" that most DEA configurations utilize for boosting their performance and enabling some applications. Thus, the development of existing and designing new configurations that operate without prestretch is the main scope of additively manufactured DEA-based soft actuators.

1.1.4. Modeling

Accurate prediction of device behavior allows optimizing its design for maximum performance. Modeling complex actuator design made of untrivial material can be overcomplicated analytically or time-consuming numerically. In some cases, utilization of a much simpler model is possible with a marginal error. Determining appropriate modeling techniques, focusing on their efficiency, for additively manufactured DEAs can accelerate the development of the latter.

1.2. Objectives

Based on the explained motivation as well as the literature review presented in Chapter 2, this section sets the goals for this research. Considering the initial state of DEA AM, this dissertation aims to establish the main aspects of high-quality additively manufactured DEAs, including fabrication methodology, DEAs' dielectric and electrode materials performance and manufacturability, new configurations of additively manufactured DEA soft actuators, and their modeling. For each aspect of 3D printed DEAs, the research's primary objectives can be formulated as follows:

- *Manufacturing.* Conduct a comprehensive analysis of currently utilized and potential AM methods and additively manufactured DEAs reported in the literature. Reveal the significant flaws and reasons behind the poor implementation of the printed DEAs. Describe, correlate, and evaluate methods to overcome manufacturing, material, and design defects to improve printed DEA implementation and performance.

- *Dielectric material.* Enhance the electromechanical performance of 3D printed DEAs through the improvement of dielectric elastomer properties. First, determine the most appropriate approaches to improve the dielectric material of 3D printed DEAs considering their manufacturing process, application, and operation conditions. Then, implement the selected approach and investigate its effects on DE material and 3D printed DEA actuation performance.

- *Electrode material.* Review the literature on stretchable electrodes and current progress on compliant electrodes designed or suitable to a certain degree for 3D printed DEAs application. Then, considering various effects of electrode

properties on DEA performance, design a printable electrode material that compromises 3D printed DEA actuation to the smallest possible extent.

- *DEA configuration.* Design a novel 3D printed DEA configuration with the aim to increase actuation capabilities of additively manufactured soft actuators, particularly in terms of deformation.

2. Review of the Relevant Literature

This chapter reviews current progress in DEAs technology, dielectric and electrode materials, DEA conventional and additive manufacturing, and their configurations and applications. Based on the review, important conclusions are drawn throughout the chapter to specifically address the research subjects and prepare the reader for the study's methodology and results.

2.1. DEA Smart Material

DEAs represent a class of electroactive polymers (EAP) and are materials that possess properties appropriate for soft actuators (Guo-Ying, Jian, Li-Min, & Xiangyang, 2017). DEAs are studied broadly owing to their significant deformation capability, moderate force capacity, and considerable specific actuation energy density (Kovacs, During, Michel, & Terrasi, 2009). Common single-layer DEA can be described as a capacitor consisting of two compliant electrodes and dielectric elastomer in between, as demonstrated in Figure 2.1.
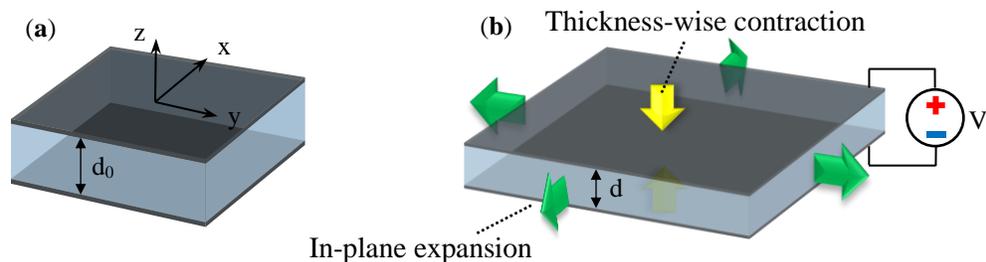
Figure 2.1 Dielectric elastomer actuator in (a) passive and (b) actuated states.

When a DC voltage is applied to the electrodes, positive and negative charges attract each other, concentrating near the surfaces of electrodes and producing electrostatic

forces that squeeze the elastomer [3]. The magnitude of the produced electrostatic, or Maxwell, pressure can be found as follows (R. Pelrine et al., 2000):

$$p = \varepsilon_0 \varepsilon_r E^2 = \varepsilon_0 \varepsilon_r \left(\frac{V}{d}\right)^2 \tag{1}$$

where ε_0 is the vacuum permittivity constant, ε_r is a relative dielectric permittivity of the DE material, E is an applied electric field, V is an applied DC voltage, and d is a DE thickness in the current (deformed) state. The maximum amount of electric field applied to DEAs is limited by DE material dielectric (or breakdown) strength E_B. Typical DE materials have a dielectric strength of a 10^2 kV/mm order. Therefore, to generate an electric field that causes considerable deformations of compliant DEA materials, kV order of magnitude voltage is typically applied to 10-100 µm thick DE films.

Due to the electrodes' attraction, the elastomer shrinks thickness-wise due to its compliance and considerably expands in-plane direction due to its incompressible nature. Utilizing this operation principle, acrylic DEAs have shown relative area strain over 200% (Pelrine R & Joseph, 2000), kilogram-order actuation force (Mihai Duduta, Hajiesmaili, Zhao, Wood, & Clarke, 2019; Kovacs, Düring, Michel, & Terrasi, 2009), and 19.8 J/kg energy density (Mihai Duduta et al., 2019). Besides these achievable characteristics, DEAs possess fast, controllable, and reversible electromechanical response that gives them self-sensing capabilities (M. Duduta, Clarke, & Wood, 2017; Maffli, Rosset, Ghilardi, Carpi, & Shea, 2015; Rosseta, Gebbersa, O'Brien, & Shea, 2012).

The outstanding electromechanical characteristics and multifunctional capabilities led to extensive utilization of DEA for various applications, including soft grippers, soft robots, active lenses, artificial muscles, and soft sensors (Figure 2.2). As seen in the

figure, DEAs have various appearance, which are called configurations, to perform

certain types of actuation most effectively.
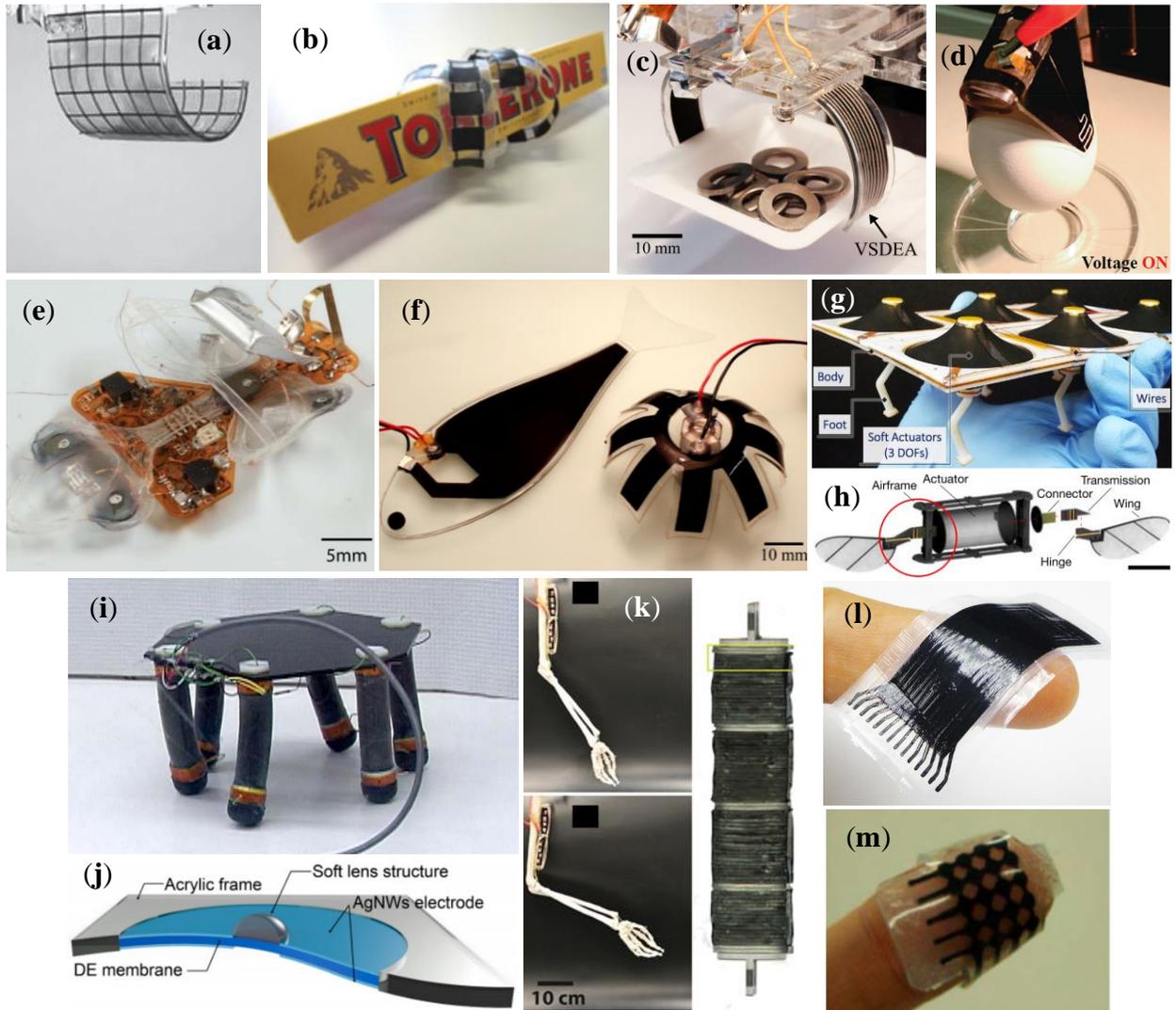
Figure 2.2 Current application of DEA in soft grippers employing: (a) fiber reinforcement (Shian, Bertoldi, & Clarke, 2015), (b) minimum energy structures (O. Araromi, Gavrilovich, et al., 2015), (c) low-melting-point alloy (Shintake, Schubert, Rosset, Shea, & Floreano, 2015), and (d) electroadhesion (Shintake, Rosset, Schubert, Floreano, & Shea, 2016); soft robots: (e) autonomous (Ji et al., 2019), (f) underwater (Shintake, Shea, & Floreano, 2016), (g) crawling hexapod (Nguyen, Phung, Nguyen, Jung, & Choi, 2017), (h) controlled flight insect micro robot (Y. Chen et al., 2019), and (i) walking (Pei, Rosenthal, Stanford, Prahlad, & Pelrine, 2004); (j) active lenses (Yun et al., 2015); (k) artificial muscles (Mihai Duduta et al., 2019); (l, m) soft sensors (Kadooka, Imamura, & Taya, 2016b; Koo et al., 2006).

2.2. DEA Configurations

To enhance or alter DEA deformation, various configurations of the actuator can be used. Prestretched DEA is the most early and used configuration that enables utilization of stored strain energy in the prestretched DE film, maintains in-plane fashion of the expansion (no out-of-plane warping or buckling of the DE film), decrease DE film thickness, and sometimes improves electromechanical stability of the actuator. Thus, prestretched DEAs are usually used where a radial deformation or electrode area change is needed. To increase the out-of-plane contraction or achieve out-of-plane elongation, stacked or rolled configurations are used, respectively. These configurations are typically categories by considerable blocked force (Benslimane M Y & Tryson, 2010; Carpi, Salaris, & Rossi, 2007; Kovacs, Düring, et al., 2009). However, most effective way to achieve large deformations is through bending.
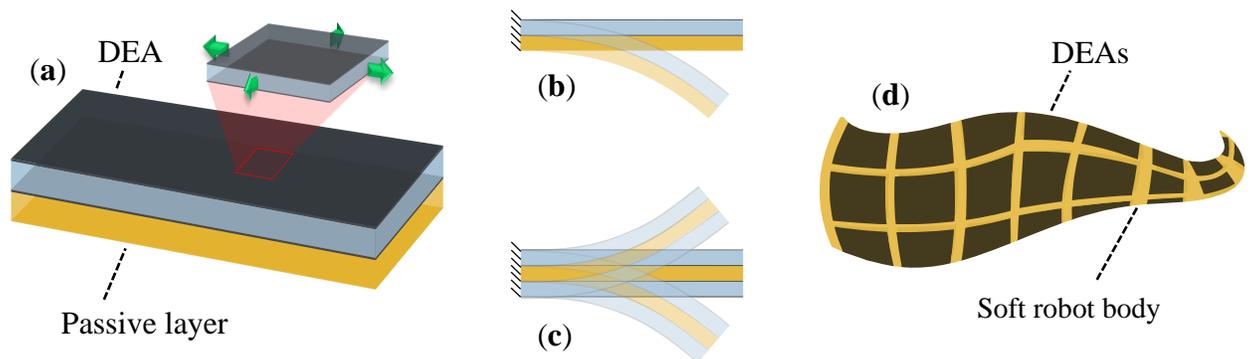
Figure 2.3 (a) Unimorph DEA configuration; bending of (b) unimorph and (c) bimorph DEA actuators; (d) concept of multimorph biomimetic soft robot with distributed DEAs.

There are multiple approaches to translate DEA's thickness-wise contraction and in-plane expansion into the out-of-plane motion. Some of these approaches, in descending popularity, are unimorph/bimorph (Figure 2.3) (Mihai Duduta, Wood, & Clarke, 2016;

Franke et al., 2020), discretely stiffened actuators (Lai, Bastawros, & Hong, 2012; Shian

et al., 2015), preload mechanisms (Luan, Wang, & Zhu, 2010; Phung, Nguyen, Jung,

Nguyen, & Choi, 2020) (including inflatable DEAs (Ha, Yuan, Pei, Pelrine, & Stanford,

2006; Keplinger, Li, Baumgartner, Suo, & Bauer, 2011)), buckling (Chen, Liu, & Zhu,

2019; Son et al., 2012), multistable (Zhao et al., 2016), origami structures (J. Li, Godaba,

Zhang, Foo, & Zhu, 2018), and special DEA configurations (Hajiesmaili & Clarke, 2019;

Sikulskyi, Yu, et al., 2021). The approaches are further described in Table *2.1*.

Table 2.1 Current methods to produce out-of-plane DEA actuation.

Approach	Description
Unimorph (continuous stiffening)	It is one of the most utilized methods to produce bending. A unimorph actuator consists of an active layer, e.g., DEA, that tends to expand in-plane and a passive layer that only provides stiffness, causing unsymmetrical actuation (variable-through-thickness strain) and bending about the common neutral axis.
Frames (discrete stiffening)	The passive (stiffening) layer in a unimorph actuator can be replaced with discrete stiffeners. A wider range of motions can be obtained by varying the stiffeners' design, e.g., orientation.
Special DEA configuration	Another way to produce bending through the variable induced strain is to stack DEA layers of different sizes and patterns. While the method is arguably the most effective in reaching sizeable out-of-plane deformation, the desired complex shapes can be obtained as no stiffening elements, besides the stacked DEA layers, are introduced into the actuator.
Buckling	Out-of-plane deformation can also be achieved by buckling of either a thin DEA or special DEA-driven structures.
Multistable structures	In-plane DEA actuation can be utilized to switch between the minimum potential energy (stable) states of various multistable structures.
Preload mechanisms (cone actuator)	DEA can be prestretched into a conic shape so that its actuation leads to an increase in cone height. Single- and double-cone configurations often utilize a mechanical spring or rigid separator, respectively, to prestretch DEA films.
DEA-driven origami	Larger deformations and unique motions can be achieved using origami structures capable of outstanding morphing and driven by locally attached or distributed DEAs.

The nature of the soft robots limits the methods that utilize rigid frames or additional mechanisms. One of the main advantages of 4D-printed DEA soft robots is the simplification of the manufacturing process by minimizing of production stages, while increasing precision. Therefore, bending configurations are selected according to their acceptable manufacturability through AM methods, workability without further assembly and modification, and minor stiffening.

A considerable portion of the aforementioned configurations necessitate actuators that are fabricated and operate with prestretch. Typically, a dielectric film is prestretched, and then electrodes are applied on both sides. However, it is desirable that AM results in the final product without further modification. Additionally, as both electrode and elastomer layers are deposited during 4D printing, the process limits the possibility to prestretch the printed DEA. This limitation depends on the stretchability among other strain-dependent properties of the material, particularly for the electrode. Despite new AM approaches promise fabrication of prestretched DEAs of certain configurations, no operating product was demonstrated to date (Coulter, Coulter, Marks, & Ianakiev, 2018; Coulter, Coulter, Papastavrou, & Ianakiev, 2018). Therefore, actuator configurations that operate without prestretch are the main focus of additively manufactured DEAs.

As a result, unimorph/bimorph actuators are the most common type of fully printed bending DEAs. These actuators utilize a combination of passive and active DEA layers that create unsymmetrical actuation causing the whole structure to bend about the common neutral axis. Unimorph actuators have DEA layers only on one side of the passive layer, while bimorph actuators have both sides of the passive layer covered with DEAs. For the application of soft robotics, the passive layer's role is typically played by

the robot's soft body to produce bending motion. Furthermore, a unimorph/bimorph concept can be extended to a biomimetic soft robot body with distributed embedded DEAs. Stacking DEA layers forms a multilayer unimorph DEA (MUDEA). In contrast to a regular stacked DEA, increasing the number of DEA layers, and hence thickness, in the unimorph actuator results in a greater blocking force. As the thickness builds up both actuation force and stiffness, optimizing the total DEA thickness (through the number of printed DEA layers) is a way to maximize actuator's deflection capability.

2.3. DEA Modeling

This section introduces the fundamental concepts of modeling and performance estimation of DEAs. Actuation characteristics of DEAs depend on the actuator configuration, geometry, and material properties. Therefore, the effects of these three aspects on the DEA soft robot performance are addressed in this section.

2.3.1. General DEA Modeling

As discussed in the introduction, actuation of most of the DEA configurations originates from the thickness-wise contraction and in-plane expansion of DE layers. The electrodes' voltage-induced attraction in DEAs is evaluated in terms of Maxwell pressure (Equation 1). The amount of deformation is dictated by the DEAs' material properties, i.e., both electrode and DE layers, boundary conditions (BCs), and external loadings. Different types of BCs and loadings often require different modeling approaches (T. Lu et al., 2012). Therefore, modeling usually starts with the unconstrained and unloaded case for which material properties are the only consideration.

In general, compliant and stretchable DEA materials exhibit nonlinear viscoelastic behavior; however, the amount of viscous and nonlinear elastic components can vary

greatly for different materials. Several mathematical models have been developed to describe these types of behavior. To accurately predict actuator behavior, a material model needs to be chosen according to the material's degree of viscoelasticity and actuator operation, e.g., short- and long-term actuation or actuation frequency. Advanced models describe actuator behavior more accurately, but their utilization can be complicated by unavailability or inability to obtain necessary material properties. In contrast, linear material models are simple to use, but they need to be applied only when nonlinearity or operational strain is not considerable.

Printed DEAs typically operate in a non-prestretched mode and therefore relatively low strain. Additionally, as most materials utilized for printing DEAs are silicone elastomers, which possess more linear and elastic behavior than acrylic elastomers that are frequently used for DEAs (Madsen, Daugaard, Hvilsted, & Skov, 2016), linear material models are often applied and provide sufficiently accurate results for 4D printed DEAs.

For instance, Equation 2 shows a simple thickness-wise strain formula often used to characterize DEA performance. While it is possible to assume an undeformed DE thickness, d_0, for the calculation of strains less than 10% (Qiu, Zhang, Plamthottam, & Pei, 2019), Equation 3 is more used as the general strain solution of the linear model (R. E. Pelrine, Kornbluh, & Joseph, 1998).

$$\varepsilon_{z0} = -\frac{p}{Y} = -\frac{\varepsilon_0 \varepsilon_r}{Y}\left(\frac{V}{d_0}\right)^2 \tag{2}$$

$$\varepsilon_z = -\frac{2}{3} + \frac{1}{3}\left(f(s_{z0}) + \frac{1}{f(s_{z0})}\right) \tag{3}$$

$$\text{where} \quad f(s_{z0}) = \left[\frac{1}{2}\left(2 + 27s_{z0} + \sqrt{-4 + (2 + 27s_{z0})^2}\right)\right]^{1/3}$$

where Y is DE Young's modulus, d_0 is the initial thickness of DE film (before actuation).

For larger strains or highly nonlinear materials, the linear model cannot guarantee reliable results. Therefore, nonlinear modeling of DEAs is necessary in these cases. As elastomers are composed of slightly cross-linked long and flexible polymers, they generally exhibit an S-shape stress-strain relation with three distinct regions (Figure 2.4). The first region is characterized by initially higher but decreasing stiffness as material's deformation occurs primarily due to polymer chains' rotations about their bonds. The second region, usually the largest one, has a lower and more constant incline due to polymer chains' continuous spring-like unfolding. Finally, the third region is characterized by a drastic increase in stiffness as the polymer chains get straighter, subjected to tension, and unveil their true stiffness (Suo, 2010; White & De, 2001).
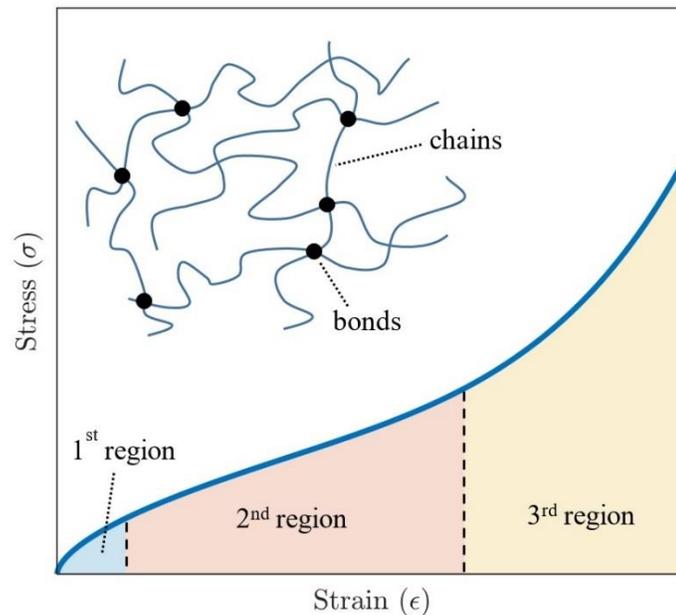
Figure 2.4 A S-shaped stress-strain curve of a typical compliant elastomer.

To fit such behavior, numerous hyperelastic models have been developed. In general, the approach defines a strain energy function for a material that can be differentiated to determine stress and compared to the applied stress (Maxwell pressure) to find deformations. Each hyperelastic model proposes its strain energy function based on different assumptions. The functions are dependent on deformation invariants and a different number of material properties coefficients obtained through curve fitting of the materials experimentally tested. The higher-order models (more coefficients in the strain energy function) typically provide higher accuracy but might require more sophisticated material tests to determine the model coefficients. Some commonly used models include Neo-Hookean (Treloar, 1975), Mooney-Rivlin (Rivlin & Taylor, 1948), Ogden (Ogden & Hill, 1972), Yeoh (Yeoh, 1990), Arruda-Boyce (Arruda & Boyce, 1993), and Gent (Gent, 1996). For example, Neo-Hookean is a one-parameter model and can model the first two regions of the elastomer's S-shape stress-strain relation. Therefore, it is usually accurate for low and moderate strains. Other models have higher orders and can fit the S-shape curve with the acceptable tolerance at larger strains.

Some applications can require long-lasting actuation. For these cases, material viscosity effects on DEA performance need to be accounted for (Brochu & Pei, 2010; Rosenblatt-Weinberg, 2013). Accordingly, linear or hyperelastic models are extended to modeling the viscoelastic behavior of DEAs (Kollosche, Kofod, Suo, & Zhu, 2015; Wissler & Mazza, 2005a).

Once DEA thickness contraction is determined through one of the models, in-plane expansion of the actuator can be easily calculated assuming material's incompressibility

(Equation 4) in terms of strains and stretches (R. E. Pelrine et al., 1998; Wissler & Mazza, 2005b):

$$\varepsilon_x = \varepsilon_y = \frac{1}{\sqrt{1 + \varepsilon_z}} - 1 \qquad \text{or} \qquad \lambda_x = \lambda_y = \frac{1}{\sqrt{\lambda_z}} \tag{4}$$

where ε_x, ε_y, and ε_z are strains along x-axis, y-axis (in-plane) and thickness, respectively, and λ_x, λ_y, and λ_z are corresponding stretches.

2.3.2. Unimorph and Bimorph DEAs

A general analysis of unimorph and bimorph actuators can be analyzed using a similar smart material actuator. Being one of the earliest studied smart materials, piezoceramic-based bending actuator can provide insight into the activation response under external stimulus (Q.-M. Wang & Cross, 1998). As such, the tip deflection of cantilever unimorph and bimorph actuators can be calculated according to Equations (5) and (6), respectively:

$$\delta_{uni} = \frac{3L^2}{2t} \cdot \frac{2AB(1 + B)^2}{A^2B^4 + 2A(2B + 3B^2 + 2B^3) + 1} \cdot \varepsilon_{act} \tag{5}$$

$$\delta_{bi} = \frac{3L^2}{2t_p} \cdot \frac{2AB^2(1 + B)}{A^2B^4 + 2A(2B + 3B^2 + 2B^3) + 1} \cdot \varepsilon_{act} \tag{6}$$

where L is the actuator's cantilever length, t is the total thickness of the actuator, t_p is the passive layer thickness, $A = Y_p/Y_a$ is the Young's moduli ratio of passive to active layers, $B = t_p/t_a$ is the thickness ratio of a passive layer to each active layer, ε_{act} is strain of the active layer (originally the piezoelectric strain, which is substituted by the DEA strain). Therefore, this actuator model utilizes a linear material strain while accounting for geometrical nonlinearities in the cantilever beam. The last feature is

important as DEA unimorph actuators typically generate deformations far beyond the

Euler-Bernoulli beam limits.
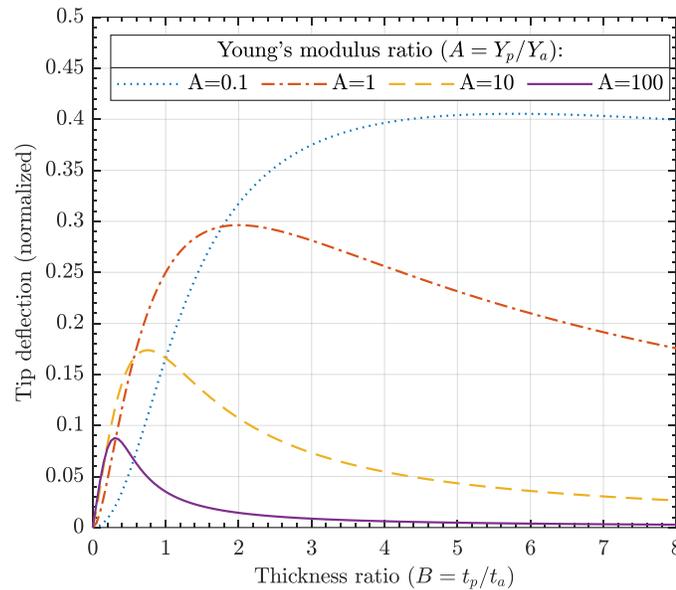
Figure 2.5 Effect of substrate thickness and stiffness on unimorph DEA bending (the normalized tip deflection is represented by a middle component of Equation 5 (Q.-M. Wang & Cross, 1998), independent of actuator length, total thickness, and DEA strain).

Figure 2.5 shows the existence of the optimum passive-to-active thickness ratio of

unimorph DEA. The same result was demonstrated experimentally and numerically

(FEM) by Araromi *et al.* (Oluwaseun A. Araromi & Burgess, 2012), along with an

extension to MUDEAs. Therefore, one of the main goals of unimorph actuator modeling

is to determine the optimum DEA and passive layer thicknesses for particular materials.

The DEA can then be represented as a stacked DEA of the same total thickness to lower

the driving voltage of MUDEA.

A hyperelastic Neo-Hookean material was utilized with a nonlinear Euler-Bernoulli

beam model to analyze a fully printed unimorph DEA (Haghiashtiani, Habtour, Park,

Gardea, & McAlpine, 2018). Nevertheless, the actuator's deflection capability made of thick layers of very compliant materials was predicted with a considerable error. It was concluded that time-dependent material properties and neglected transverse shear effect in the beam model are the major sources of error. Indeed, the shear effect was shown to be an important factor in the actuation of unimorph DEAs (Oluwaseun A. Araromi & Burgess, 2012).

To account for a time-dependent deformation, a linear material model was complemented by a viscous component (Kadooka et al., 2016a). Even for a DEA made with a relatively stiff DE material (Y=390 MPa), the derived linear viscoelastic model showed a considerable deviation for a short-term actuation but matched the long-term actuation.

Overall, considering unimorph DEAs' ability to generate large deflections through small strains, it is important to treat the actuators as nonlinear beams while materials nonlinearity becomes a secondary source of error. Considering potential three-dimensional DEA soft robot structures, accounting for the transverse shear effect during bending becomes crucial.

2.4. Dielectric Elastomers (DE)

Dielectric elastomer is a core element of DEA and largely affects the main parameters and final performance of the actuator. Namely, the dielectric relative permittivity and the thickness of the dielectric elastomer are the only two design parameters that determine the Maxwell pressure. Moreover, DE material properties and film thickness determine voltage limitation for electrical breakdown of the actuator. Consequently, most of the work to improve actuator performance is accomplished on DE material.

In general, there are many types of materials that can be used as dielectric elastomers. Most common are silicones, acrylic elastomers, and natural rubber, which are chosen based on the desirable electro-mechanical properties and application of the final DEA. Among them, silicones are of the highest interest for morphing structures applications. Being relatively compliant, they possess quite stable time and temperature-dependent behavior, lower viscous losses than acrylics, high fatigue properties, low Mullins softening and ageing effects (Figure 2.6) (Madsen et al., 2016). One of the groups of silicones most commonly utilized for DEAs is polydimethylsiloxane $(CH_3)_3SiO[Si(CH_3)_2O]_nSi(CH_3)_3$ (PDMS).
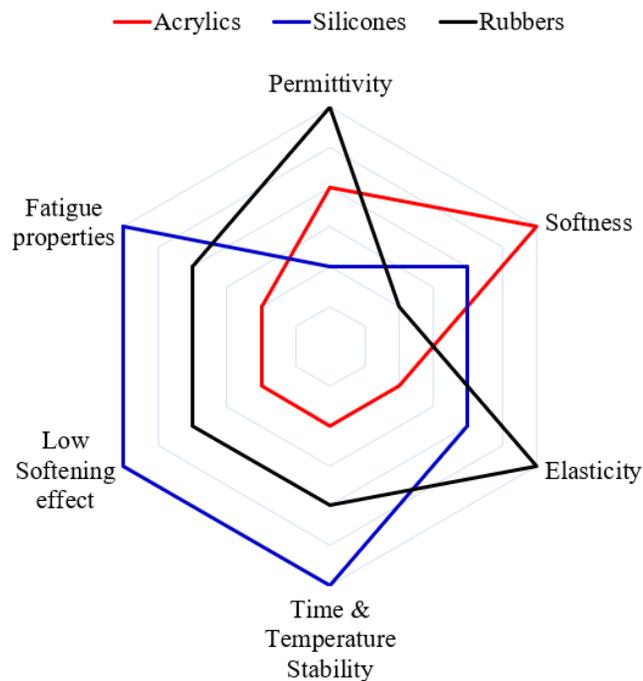
Figure 2.6 Property diagram for acrylics, silicones, and rubbers as DE materials.

Moreover, acrylics can often outperform silicones when operating in a prestretched state (J. Huang, Shian, Diebold, Suo, & Clarke, 2012). As current AM methods remove

prestretch from the equation, application of silicones becomes more advantageous. Furthermore, designing and controlling systems with stable material properties is much more practical. The drawback of silicones is their lower dielectric permittivity (between 2 and 3) compared to natural rubber and acrylics (up to 8). One of the approaches to increase silicone permittivity is adding highly conductive or dielectric fillers to form a particulate dielectric composite. The final permittivity depends of the type of filler, amount of filler, and dispersion method, and can change in a wide range of 3-300 (Madsen et al., 2016).

Lately, novel silicones have been developed to achieve superior dielectric and mechanical properties, however, they are not yet available as commercial materials (Mayumi et al., 2019; Shintake, Matsuno, Baba, & Takeuchi, 2019).

2.4.1. DE Material Selection

For 3D printed DEAs, dielectric and conductive materials are chosen based on their performance and technological properties. Performance-wise, a simple approach of figures of merit (FOMs) is well established. Assuming materials to be linearly elastic, FOMs allow uncomplicated comparison of various DE materials. Various FOMs can be used for different DEA objectives (Table *2.2*). It should be noticed that these FOMs still neglect electrode stiffness and represent the performance for various objectives of individual-unconstrained DEAs. Nevertheless, these FOMs can be used in the initial material selection for unimorph actuators or DEA soft robots.

Lastly, DEA materials' stretchability and strain-dependent properties are typically considered for DEA operating at moderate and high strains. While material properties' dependence on strain can be easily applied to the FOMs, it is often not required for

printed DEAs operating without prestretch. Therefore, printed DEAs can utilize a wider range of materials by relaxing requirements for stretchability and strain-dependent properties.

Table 2.2 Figures of merit (FOMs) for dielectric materials.

Equation	DEA objective
$FOM = \dfrac{\varepsilon_r E_B^2}{Y}$	Maximum actuation strain (Sommer-Larsen & Larsen, 2004)
$FOM = \varepsilon_r E_B^2$	Maximum blocked force
$FOM = \dfrac{\varepsilon_r}{Y}$	Maximum actuation strain per unit of applied voltage (Della-Schiava et al., 2018)
$FOM = \varepsilon_r$	Maximum blocked force per unit of applied voltage (Della-Schiava et al., 2018)

2.5. DEA Electrodes

Dielectric elastomer material largely determines the performance and main characteristics of the actuator. Due to the heavy focus on dielectric elastomers, there is a noticeably smaller amount of research conducted on a compliant electrode specifically for DEA application. However, electrodes are an integral component of electrically responsive actuation systems as they are responsible for delivering and properly distributing electrical stimuli.

When looking at soft actuators, electrodes need to be soft and stretchable while serving their main purpose of conducting electricity. Stretchability ensures electrode's structural integrity and conductivity are maintained when actuator is highly deformed. Various applications, such as soft sensors, require flexibility or stretchability, but not necessarily compliance, for their applications (S. Huang, Liu, Zhao, Ren, & Guo, 2019; Jeerapan & Poorahong, 2020; Ma, Kong, Pan, & Bao, 2020). Thus, stretchable electrodes

received great attention and are described in numerous reviews and research papers for their performance (Hong, Lee, & Kim, 2019; Matsuhisa, Chen, Bao, & Someya, 2019; Sim, Rao, Ershad, & Yu, 2020), applications (Wu, 2019), and printability (Kraft, Molina-Lopez, Son, Bao, & Murmann, 2020). As they satisfy the necessary condition for desired functions, stretchable electrodes were generally sought after for initial development and proof of concept of soft actuators (Kaneto, 2016; N. Lu & Kim, 2014). While having stretchability as an intrinsic property of the electrode enabling it to function, actuator performance is still limited due to the electrode's stiffening effect. Focusing on reducing the electrode's stiffening effect, i.e., increasing its compliance, enables realization of maximum actuation deformation. Moreover, recent studies have shown that the effective voltage across the DE membrane is lower for thick and less conductive electrodes (J. Zhang, Liu, & Chen, 2020). Thus, the ability of conductive materials to be coated in thin layers through AM is another printability factor considered in this work.

While electrode compliance, printability, and conductivity are the focus of present research, other important electrode properties are worth mentioning and keeping in mind when selecting and modifying the conductive compliant material for DEA electrodes. These properties are adhesion to selected elastomers, viscous losses, fatigue characteristics (both mechanical and electrical), and aging effects.

As DEA research has been dominantly focused on actuator designs, configuration, and elastomer material rather than electrode, and neglecting electrode effects in DEA modeling in most cases, authors tend to choose electrode materials that are easier to handle and process but that not necessarily provide the best DEA performance (Rosset & Shea, 2013). Most utilized types of conductive materials for DEA electrodes include

conductive grease (carbon, silver etc.) and loose conductive particles (carbon black, graphite, graphene, carbon nanotubes (CNT) etc.). For example, carbon grease (CG) became the most popular option for single-layer DEAs. It is easy to apply manually and does not introduce additional stiffness into the actuator but has relatively low conductivity, e.g., 0.006-0.02 S/cm for MG Chemicals commercial products (Chemicals, 2015). While low electrode sheet resistance can be achieved by applying a relatively thick layer of CG, e.g., 0.1-0.5 mm, much thinner electrodes are desired for high-performance and stacked actuators. Additionally, major drawbacks such as lack of longevity are observed, precluding them from applications demanding long-term, stable operation. While loose conductive particles allow fabricating stacked DEAs to a greater degree than conductive greases, they suffer from similar issues with long-term performance.

To overcome the drawbacks of conductive greases and loose particles, numerous new electrodes materials were developed. Most of these electrode materials are produced through two major approaches, utilizing polymers with conductive fillers (conductive composites) or intrinsically conductive polymers.

The first group of electrodes are polymers filled with conductive particles, e.g., silicone filled with carbon-based (CNTs, graphene, graphite) or metallic particles (wires, flakes, and powders). This group of electrodes have a wide range of conductivity, compliance, and high time-dependent stability (Sengupta, Bhattacharya, Bandyopadhyay, & Bhowmick, 2011). The characteristics of conductive particles such as type, shape and amount as well as greatly influence the properties of the electrode. Furthermore, methods used to evenly distribute these particles in the elastomeric base or produce a conductive

network with a segregated structure impact the resulting electrode (Pang, Xu, Yan, & Li, 2014). Namely, larger amounts of fillers generally make electrodes more conductive. However, the electrode becomes stiffer and less stretchable which are the main drawbacks of these types of conductors. The type of fillers determines the range of potentially reachable conductivity and other properties. Lastly, specific surface area is a crucial parameter in determining the percolation threshold, the minimum amount of fillers required to make a polymer conductive (W. Zhang, 2007). As a result, a larger amount of three dimensional particles, e.g., graphite (Sengupta et al., 2011) and metal powder (Mamunya, Valeriy, Pissis, & Lebedev, 2002), is needed to reach conductivity as compared to two dimensional fillers, e.g., graphene (Papageorgiou, Kinloch, & Young, 2015) and metal flakes (W. J. Kim, Taya, & Nguyen, 2009). One dimensional particles, e.g., CNTs (Spitalsky, Tasis, Papagelis, & Galiotis, 2010) and metal wires (Cui, 2019), have the lowest percolation threshold (Rosset & Shea, 2013).

The best performance in terms of conductivity in this class of electrodes is demonstrated by one-dimensional, high aspect ratio particles. For instance, single-wall CNT (SWCNTs) dispersed in PDMS can reach a stable conductivity over 100 S/cm at weight fraction of 15.8 wt.% (Sekitani et al., 2009). For silver nanowires in styrene-butadiene-styrene (SBS), stable conductivity value over 9000 S/cm was reported at weight fraction of 18 wt.% (S. Choi et al., 2015). However, the highest values of conductivity are obtained with longer fibers, particularly up to 70 µm for silver wires, and 1 mm for CNTs, which often hinders the implementation of additive manufacturing. To further improve percolation characteristics, different combinations of fillers are used.

For example, PDMS filled with CNTs and silver flakes can reach a conductivity value of 3100 S/cm at just 6 wt.% of CNTs and 2.6 wt.% of silver flakes (Chun et al., 2010).

The second method involves utilization of intrinsically conductive polymers. In their raw form, they do not tend to possess sufficient combination of electro-mechanical properties needed for soft actuators. Thus, conductive polymers are typically modified by adding plasticizers and dopants, blending with other compliant and stretchable polymers, undergoing some physical manipulations, forming hydrogels, or being further chemically altered. Due to the variety of modification approaches, conductive polymers have great potential and flexibility in achieving desired combination of properties. There is a number of materials currently studied, such as polypyrrole (PPy), polyaniline (PAni), polythiophene (PTh), poly(3,4-ethylene-dioxythophene) (PEDOT), etc. (Kaur, Adhikari, Cass, Bown, & Gunatillake, 2015). However, poly(3,4-ethylene-dioxythiophene):poly(styrenesulfonate) (PEDOT:PSS) is currently one of the most intensively studied polymers for supercapacitors and stretchable devices due to its electrical properties, manufacturability, commercial availability, and further improvement potentials (Fan et al., 2019; Sim et al., 2020; Sun et al., 2015). Specially treated films of PEDOT:PSS can reach superior conductivity over 3100 S/cm in a non-deformed state and over 4100 S/cm when deformed to a certain degree. However, they are only stretchable up to 6% (Kayser & Lipomi, 2019) and have reported Young's modulus values varying from 417 MPa to 2.8 GPa (Lang, Naujoks, & Dual, 2009; Oh, Kim, Baik, & Jeong, 2016; Okuzaki & Ishihara, 2003; Y. Wang et al., 2017). While humidity of the testing environment greatly affect PEDOT:PSS stiffness (Lang et al., 2009), the lack of explanation on how Young's modulus is calculated from the experimental data in

numerous studies is also seen as a considerable source of results deviation. To benefit

from PEDOT:PSS application in compliant electronics, several techniques were created

and tested to increase stretchability as a primary goal and consequently lower Young's

modulus (Kayser & Lipomi, 2019).

Out of the many approaches utilized, mixing PEDOT:PSS with hydrophilic compliant

polymers or plasticizer have shown to be the most effective at improving the desired

mechanical properties while maintaining the homogeneous structure of the electrode.

When mixed with compliant polymers, such as poly(ethylene glycol) (PEG), and

ethylene glycol (EG), elastic modulus was lowered from 1.1 GPa to approximately 145

MPa with a stretchability up to 22% and conductivity of 176 S/cm (P. Li, Sun, &

Ouyang, 2015). Although plasticizers usually outperform polymers in improving the

mechanical properties of PEDOT:PSS for compliant electronics, they tend to be more

hazardous to the environment. Some plasticizers decrease Young's modulus only to 20-

50 MPa and increase stretchability far more than 100% with conductivity of above 1000

S/cm at most of the strain range (Y. Wang et al., 2017). For most DEA applications, such

high stretchability is not required, however the Young's Modulus should be as low as

possible. Therefore, plasticizers such as Triton X-100 are preferable as it lowers the

elastic modulus down to 0.9 MPa while increasing stretchability to 55% and maintaining

conductivity of 53 S/cm (Oh et al., 2016).

A closer look at the literature on stretchable electrodes reveals few more gaps besides

lacking compliance. Firstly, mechanical characteristics, particularly stiffness, are not

studied thoroughly enough at various strains. This is particularly important for DEA soft

actuators capable of large deformation. Secondly, material properties that are not directly

related to conductive material performance but can affect its handling and fabrication quality are often overlooked or discussed to a small degree. Thus, this research aims to investigate several simple and promising approaches for compliant and stretchable electrodes, particularly in improving the compliance, and thoroughly characterize material stiffness and manufacturability properties.

Rapid prototyping is a stipulation that is typically associated with novel and dynamically advancing fields, such as soft robotics and biomimetics. As AM is a common rapid prototyping approach, printability is an extremely desired and sought-after quality of soft actuator materials. Particularly for DEAs, contact dispensing and inkjet printing are the most utilized AM methods (Kim & Sikulskyi, 2021). Despite printing conductive composites with these two AM methods is possible, their dispensing nature is susceptible to clogging the nozzle when printing microscale elements of soft actuators. Thus, the focus of this study is narrowed down to conductive polymers and their modifications.

Yet, there is no appropriate electrode material figure of merit (FOM) for soft actuator application. However, the benefits of stretchable, compliant, conductive, and thin electrodes for actuation have been shown in the literature (J. Zhang et al., 2020). Stretchability determines the actuator's workability and is dictated by the actuator's application, while compliance and conductivity are material properties that influence the actuator's performance. Therefore, Table *2.3* includes recent progress on stretchable and compliant to moderately compliant conductive materials with Young's modulus, Y < 50 MPa, and conductivity, σ > 0.1 S/cm, to demonstrate a current state of compliant and stretchable electronics.

Table 2.3 Compliant and stretchable electrodes commonly used, recently designed or potentially suitable for DEAs.

(Ref)	Composition	Conductivity, S/cm	Stretchability, %	Young's modulus, MPa
(Chemicals, 2015)	Carbon grease	0.006-0.02	n/a	negligible
(Rossiter, Walters, & Stoimenov, 2009)	Silver grease	10^{-3}	n/a	negligible
(Mihai Duduta et al., 2016)	Loose CNT electrode	-	n/a	-
(Luo, Li, Du, Zhou, & Zhu, 2019)	PDMS / PEDOT:PSS / 10 wt.% Triton X-100 / 14 wt.% EG	0.8[a]	70	0.05
(Dauzon et al., 2019)	PEDOT:PSS / 80 wt.% Zonyl / 5 wt.% DMSO	25	Nor reported	~30
(Bele et al., 2018)	PDMS / 50 wt.% Carbon black	0.2	382	0.288
(Y. Wang et al., 2017)	PEDOT:PSS / additives	410	110	35
(Oh et al., 2016)	PEDOT:PSS / Triton 80 wt.%	55	55	~0.9

[a] converted from sheet resistance.

2.6. Manufacturing

As a layered structure of intrinsically different materials, fully printed DEAs set additional requirements for fabricating process and material selection but widens the variety of manufacturable actuator configurations and devices. This subsection provides common considerations for various aspects of fabricating fully printed DEAs.

2.6.1. Conventional Methods

Numerous approaches have been utilized to produce DEA components. Uniformly thin elastomer films are fabricated through prestretching industrially pre-made films (R. Pelrine et al., 2000), spin coating (Lotz, Matysek, & Schlaak, 2011), blade-casting (also

called screen printing) (S. T. Choi, Kwon, & Bauer, 2013; Rosset, Araromi, Schlatter, & Shea, 2015), die casting (Chortos, Hajiesmaili, Morales, Clarke, & Lewis, 2020), spraying (O. A. Araromi et al., 2011), and pad-printing (Poulin, Rosset, & Shea, 2015). Meanwhile, compliant electrodes are accomplished by brushing (Rosset & Shea, 2013; Shigemune et al., 2018), spraying (Lotz et al., 2011), transferring (Mihai Duduta et al., 2019; Mihai Duduta et al., 2016), blade-casting (Cacucciolo et al., 2019), and pad-printing (O. Araromi, Rosset, & Shea, 2015; Rosset et al., 2015).

From analyzing actuation mechanisms of DEAs, certain distinctions between electrode and elastomer roles can be drawn. While electrodes' shape and orientation with respect to each other dictate the directions of attractive (electrostatic) forces, elastomer's properties define the magnitude of these attractive forces and the amount of deformation they can cause. Therefore, the DEA fabrication process focuses on accurate patterning of electrodes and producing uniform high-quality elastomers to maximize the degree of theoretical performance implementation in the fabricated actuator.

Prestretching of industrial elastomer films is one of the first techniques that demonstrated DEA's high deformation capabilities. Spin coating and blade-casting non-polymerized elastomer into films, which can be prestretched or assembled into stacked actuators (Mihai Duduta et al., 2019), are the most utilized techniques in the field. These two methods provide more flexibility than using industrial films when selecting and modifying elastomer material while achieving improved film evenness for maximum DEA performance (Madsen et al., 2016). The rest of the methods demonstrated capabilities to produce some unique DEA designs, like pad-printed DEA with the 3 μm

thick dielectric elastomer; however, they cannot be described as common techniques (Poulin et al., 2015).

From early DEA studies until now, conductive particles, e.g., carbon-based, have been serving as compliant and stretchable electrodes. Based on their loose form or the carrier they are suspended in, a corresponding fabrication method can be utilized. To achieve certain electrode patterns, most techniques coat electrodes through specially prepared masks, while pad-printing can apply only certain pre-designed electrode patterns. Considering recent active development of compliant and stretchable electrodes, the capability to coat various material compositions often becomes the main requirement for the fabrication process. Nevertheless, the even thickness remains an important aspect for electrodes to produce actuation by evenly distributing electrical charges and for the DEA stacking process.

Therefore, capabilities to utilize a wide range of materials for fabricating DEAs while precisely patterning electrodes and uniformly distributing DE layer are the main objectives of the AM.

2.6.2. AM Methods

4D printing of DEAs is in the early stages of development. Therefore, it is desired to select the appropriate AM techniques to be easily adopted and further modified as needed. The main requirements for AM methods fabricating DEAs include capabilities to produce even films with the thickness of order 10^0-10^2 μm using various materials suitable for DEAs and soft robotics. Considering the dynamically developing field of DEAs, switching between DEA designs and materials with minimum adjustments is desired to accelerate 4D printing of DEA soft robots.

As demonstrated by the early studies, fused deposition modeling (FDM) and stereolithography (SLA) capabilities in printing DEA bi-material layered structures are limited. FDM can stack layers of alternative materials but typically has a printed slice thickness greater than desired for the DE and electrode layers. SLA is capable of producing thin films; however, it lacks the simplicity in switching printed materials.

Instead, dispensing techniques can accomplish both these tasks. In general, dispensing can be performed in a contact and non-contact fashion. The non-contact techniques in turn are divided into two approaches, dynamic drop-on-demand (inkjet) and jet-forming dispensing. The difference between these methods is in the energy (speed) of the material leaving the nozzle, which defines whether a drop or a jet will form.

Widely utilized for various DEA-based devices, inkjet printing demonstrated capabilities to coat very thin films with high manufacturing efficiency (Baechler, Gardin, Abuhimd, & Kovacs, 2016). By adjusting the drop size (tip orifice size), dispensing waveform, frequency and number of printed layers, continuous traces and uniform films can be produced (McCoul, Rosset, Schlatter, & Shea, 2017). However, inkjet printing requires a narrow range of printed material properties, particularly low viscosity (0.5-40 mPa·s) and sufficient surface tension (16-70 mN/m) (Çabuk, Wegener, Gruber, Seidel, & Maas, 2020; He, Yang, Qin, Wen, & Zhang, 2017; McCoul et al., 2017; Mikkonen, Puistola, Jönkkäri, & Mäntysalo, 2020; Schlatter et al., 2020; Schönfelder et al., 2021). This limits the fabrication of films using typical DE materials to a large degree. Therefore, inkjet printing is mostly utilized to fabricate electrodes using low-viscosity conductive inks. Nevertheless, recent studies report that modified PDMS inks enable fabrication of both dielectric and electrode components of DEAs through inkjet printing

(McCoul et al., 2017; Mikkonen et al., 2020). Following this strategy, it has been demonstrated that complex soft devices with embedded and distributed DEAs can be fully printed successfully by utilizing inkjet AM (Schlatter et al., 2020).

Polyjet technique is an industrial modification of the inkjet printing that uses photopolymers in the range of higher viscosities. Being able to coat DE layers with the desired thickness, polyjet printing pioneered AM of DEAs. This technique attained extensive development over the last decade resulting in an impressive resolution and quality of three-dimensional printed parts. An option to print easily removable supportive material allows for more complex fabricated geometries. Material-wise, polyjet can print materials with the compliant currently comparable with flexible FDM filaments like thermoplastic elastomers/polyurethanes (TPE/TPU). Additionally, polyjet systems featuring digital material options are capable to mix up to three materials while printing (Pandey, 2014). Nevertheless, the application of such advanced systems for fully printed DEAs has not been reported yet. The major obstacle for polyjet DEA printing implementation is seen in the high price of AM systems and thus, they're predominantly commercial rather than research oriented. In addition, polyjet-compatible conductive materials are poorly presented and require further considerations. Nevertheless, the technique seems to be promising to fully print complex three-dimensional DEA soft robots.

Another non-contact printing technique has been developed from conventional spraying of electrode and elastomer layers. Aerosol jet printing is an AM method that sprays atomized micron-scale droplets of materials with a focused spray beam of a controlled size. This feature enables maskless printing of various sizes, from 10 μm to

several millimeters width lines (Wilkinson, Lukic-Mann, Shuttleworth, Kay, & Harris, 2019; Wilkinson, Smith, Kay, & Harris, 2019). Similar to conventional spraying, very thin films can be produced; however, moderate thickness (of order 10^1-10^2 μm) printed in multiple depositions is required for uniform films (O. A. Araromi et al., 2011). Aerosol jet printing can utilize a relatively wide range of material viscosities (1-10^3 mPa·s), covering both electrode and elastomer DEA materials (Sebastian et al., 2016; Sebastian et al., 2020). Typical defects and limitations, such as trapped air bubbles and manufacturing time, need to be addressed to fabricate stacked DEAs and soft robot bodies.

Contact dispensing (sometimes called Direct Ink Writing (DIW)) is a technique successfully employed by researchers today (Church, 2020). The material is typically pushed from a reservoir, e.g., syringe, through a dispensing needle directly on the substrate or previously printed layer, similarly to FDM. Most common dispensing systems are driven by electrical motors or pneumatic systems. The latter is considered to provide a better printing quality but typically is more expensive. While printing much thinner layers than FDM, contact dispensing is much more susceptible to the printing surface unevenness. Great attention needs to be paid to using flat leveled printing substrates. However, the main advantages of the contact dispensing and the reason behind their outstanding utilization for fully printed DEAs are printed material versatility and relative easiness of adjusting printing parameters for new/modified materials. In contrast to polyjet or SLA printing, contact dispensing does not require special-cured (UV sensitive) material and can utilize any material curing mechanism. Nonetheless, addition cure silicones, including room temperature vulcanizing (RTV), and UV light curable materials are primarily used in contact dispensing. Compared to inkjet printing, contact

dispensing can use a much wider range of material viscosities and solvents (if needed),

which can only be limited by the equipment. Thus, contact dispensing enables printing

almost any compatible electrode and dielectric materials. For a hard-to-manufacture

smart material, flexibility in selecting materials regardless of their curing mechanism and

pre-cured viscosity is a significant advantage. Similarly to polyjet printing, contact

dispensing enables manufacturing of three-dimensional structures suitable for soft robot

bodies but has also proved capability to fully print DEAs and embed them within

compliant materials. Finally, thanks to advancements in printable electronics, contact

dispensing can print conductive traces (lines) as small as 25 µm in width (Sertoglu,

2020). For DEA soft robots with distributed actuation and sensing systems, smaller

electrode traces mean that more space within the soft robot can be utilized by DEAs and

other components.

Other AM methods including FDM, selective laser sintering (SLS), conventional

SLA, digital light processing (DLP) SLA, and liquid crystal display (LCD) SLA can be

utilized for printing moderately soft three-dimensional robot bodies (Table *2.4*) (Gul et

al., 2018; Zolfagharian et al., 2016). The number of flexible materials that lately appeared

on the 3D printing market and research field, e.g., for FDM (Pitaru et al., 2020) and SLA

(Bhattacharjee, Parra-Cabrera, Kim, Kuo, & Folch, 2018), suggest further improvement

in applicability of these methods. Therefore, these methods can be combined with those

capable of fabricating DEAs to accomplish the task of embedding DEAs into soft robots.

Combining different AM techniques for DEA soft robot fabrication brings new

compatibility and AM system integration challenges. Among the possible combinations,

integration of FDM with inkjet or contact dispensing techniques is an easily formed synergy for complex three-dimensional DEA soft robots.

Overall, despite slower printing, larger printing thickness (if no solvents are used), and substrate-dependent thickness quality, contact dispensing is the most flexible ready-to-use technique. Both inkjet and polyjet printing techniques have potential to effectively fabricate high-quality DEAs. While inkjet application can be 2.5-dimensional actuators/devices with low voltage demands (because of the micron scale DE layers), polyjet has a potential for the easiest and fastest fabrication of complex three-dimensional DEA soft robots with moderate layer thicknesses. By promising faster printing process of high-quality (uniform thickness) DEAs, these methods require more adjustments compared to contact dispensing, especially regarding the materials modification. Meanwhile, contact dispensing and inkjet printing so far are the only two techniques that demonstrated fully printed DEAs.

Table 2.4 AM methods considered for DEA soft actuators fabrication.

AM method	Materials	Thickness	Advantages	Disadvantages	Application for DEA soft actuators
FDM	Flexible filaments (TPE, TPU) $Y > 10$ MPa	>100 µm	Well established technique	Thickness unevenness, high properties anisotropy	Moderately soft robot bodies
SLA	Flexible photopolymers $Y > 10$ MPa	>50 µm	High resolution and uniformity	Lack of soft materials, post-processing parts	Soft robot bodies
DLP/ LCD	Flexible photopolymers $Y > 1$ MPa	>50 µm	Faster than SLA	Less detailed (accurate) than SLA	Soft robot bodies
SLS	Flexible polymers (TPU) $Y > 10$ MPa	>60 µm	Well established technique	Lack of powder DEA-appropriate materials	Moderately soft robot bodies
Inkjet	Soft materials in the form of low viscosity inks with sufficient surface tension	10^0-10^1 µm	Fast, more independent of printing bed flatness	Limited material selection, tedious printing parameters adjustment	Fully printed 2.5-dimensional DEA soft robots
Polyjet	Flexible photopolymers $Y > 1$ MPa	16-10^2 µm	Prints materials more viscous than inkjet (DE layers)	Prints slower and thicker layers than inkjet, less affordable equipment, parts might require post-processing	Fully printed 3-dimensional DEA soft robots
Aerosol jet	Relatively wide range of soft materials, including inks, moderately viscous polymers and particulate nanocomposites with any curing mechanism	10^1-10^2 µm	Utilizes most of the material used in inkjet and polyjet printing with versatile curing	Prone to air bubble defects, slow in printing diluted materials through numerous depositions	Fully printed 2.5-dimensional DEA soft robots

Table 2.4 AM methods considered for DEA soft actuators fabrication (cont.).

AM method	Materials	Thickness	Advantages	Disadvantages	Application for DEA soft actuators
Contact dispensing	Wide range of soft materials, including inks, gels, pastes, and particulate composites with any curing mechanism	10^1-10^3 μm (10^0 μm thickness can be microdispensed by adding solvents)	Can be utilized more easily to fabricate robots' 3D soft bodies by printing with highly viscous materials	For thin films, thickness evenness is susceptible to printing bed flatness, slower than non-contact techniques	Fully printed 3-dimensional DEA soft robots

2.6.3. Partially Printed DEAs

The first analysis of AM techniques for fabricating DEA was made by Risner in 2008 (Risner, 2008). This work discussed applicability of fused deposition modeling (FDM), inkjet printing, and contact pneumatic dispensing in regard to utilized material and typically printed structures. To a certain extent, the study concluded that FDM can produce auxiliary structures for DEA devices but not the DEAs' thin layers. Silicone films and structures were fabricated by the latter two methods, but their actuation was not demonstrated.

Therefore, the first study that demonstrated operating DEAs with AM-produced elastomer films is often presented across the literature as the first implementation of 3D printed DEAs (Rossiter et al., 2009). In this study, a 90 μm elastomer film was printed utilizing a non-contact dynamic dispensing technique, polyjet printing. Polymer films were printed together with the auxiliary structures that allowed assembling two parts into a cone-like antagonistic actuator and thus prestretch the films. Prior to the assembling, films were covered on both sides with silver grease to serve as compliant electrodes. The actuator demonstrated its working capability and applicability of AM to fabricated DEA components. While not focusing on discussing the fabrication process, the researchers emphasized the importance of three-dimensional biomimetic structures and the suitability of DEAs for soft robotic applications.

The following attempt to utilize AM for DEAs used SLA to demonstrate its capability for multi-step printing (Creegan & Anderson, 2014). A 1.8 mm thick disk consisting of two layers of differently colored photopolymer was printed. Overall, SLA was proved to have limited capabilities in manufacturing structures typical for DEAs. Furthermore,

swapping materials' baths and cleaning the printing part complicates the manufacturing process, especially for printing stacked DEAs.

While AM of DE layers faced numerous obstacles, printing electrodes on pre-fabricated dielectrics was successfully implemented in a number of studies through non-contact dynamic drop dispensing (more commonly called drop-on-demand inkjet printing or simply inkjet printing) (Schlatter, Rosset, & Shea, 2017; Schmidt, Polasik, Lediaev, & Hallenberg, 2005; Shrestha, Lu, & Lau, 2018; Wilson et al., 2019). Using low-viscosity dissolved dispersions of conductive particles in silicone carriers, micron and submicron thickness electrodes were typically printed. AM of electrodes on prefabricated DE films involves flipping DEAs to print electrodes on both sides that can lead to the misaligned electrode pattern (Wilson et al., 2019). Thus, the latent manual operations are still a concern with partially printed DEAs and especially for their stacking.

An approach to partially print stack DEAs was recently demonstrated (Chortos et al., 2020). A pattern of vertical electrodes with connections was printed through a contact dispensing technique, framed, and die casted with a low-viscosity elastomer. As a result, a 10-layer stacked DEA was partially printed and demonstrated 9% thickness strain at 25 V/μm electric field. Although resulting in an operating stacked DEA, the direction of printing and the need in manual operations (elastomer die casting) limit the approach to achieve high-quality DEAs with moderate driving voltage.

Therefore, a need for approaches to fully fabricate actuators, i.e., both dielectric elastomer layers and electrodes, through AM is evident.

2.6.4. Fully Printed DEAs

Despite all complexities of fully printed DEAs, the promising electromechanical characteristics and prospective capability to produce geometrically non-trivial biomimetic soft robots with embedded distributed actuation/sensing systems have led to considerable interest in AM of DEAs over the last decade (Figure 2.7).

In the first published work on a fully printed DEA, a rectangular single-layer actuator was fabricated through aerosol jet printing (Sebastian et al., 2016). A thicker than 60 μm elastomer (Elastosil P7670 silicone) was sprayed in two depositions and thin electrodes (reduced graphene oxide ink) were sprayed in six depositions on a silicone substrate. It was reported that most of fabricated DEAs were able to actuate at voltages up to 3.1 kV. However, the actuation was not quantified.

One of the first research works reporting 4D printing of DEA soft robots through contact dispensing still involved intermediate manual steps, but demonstrated additively manufactured prestretched DEAs (Jiyu, 2016). Using various elastomer materials and contact dispensing systems (motor-driven and pneumatic) as well as characterizing printed elastomer films, fully printing DEAs through contact dispensing was pioneered. For the electromechanical DEA testing, a 215 μm elastomer film (KE-1283 silicone) was printed using pneumatic contact dispensing on top of a non-stick polyethylene film liner of 3M VHB acrylic tape, peeled off and prestretched. Carbon grease was printed as 1 mm thick electrode layers on both sides of the prestretched 3D printed elastomer film. While about 12% of thickness deformation was achieved in actuation testing, a thickness variation of 10-25% was reported across the elastomer films.
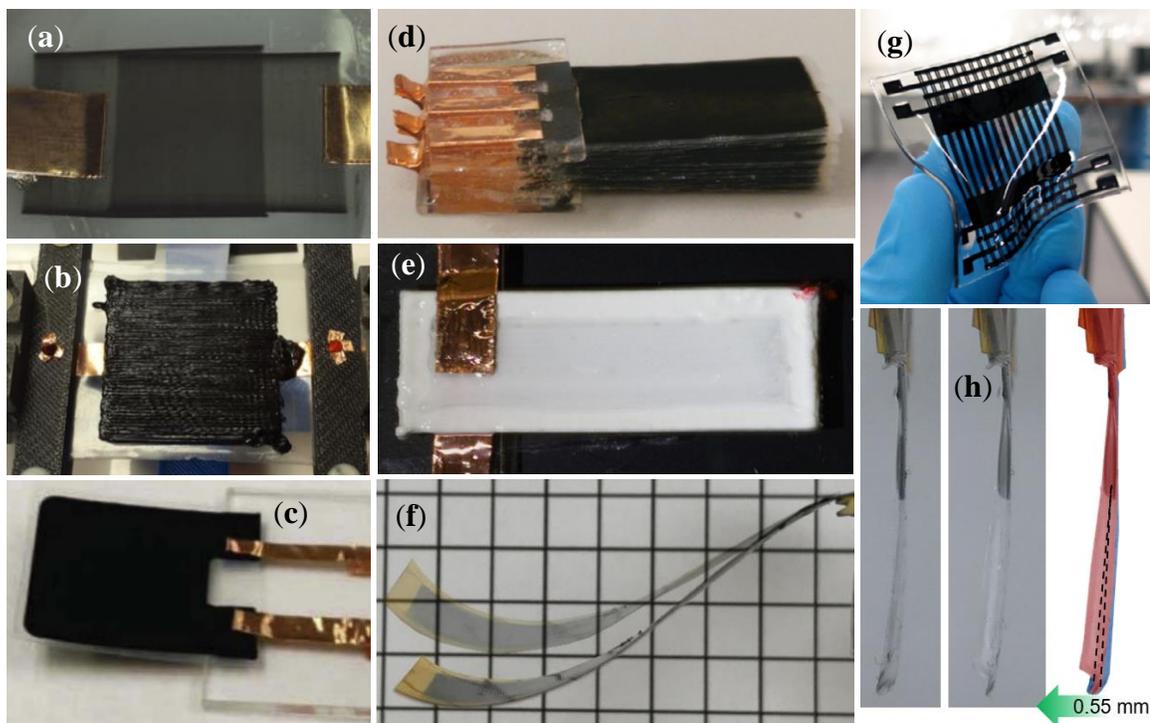
Figure 2.7 Fully 4D printed DEAs: (a) single-layer non-prestretched(Sebastian et al., 2016), (b) single-layer prestretched (Jiyu, 2016), (c) MUDEA (10 DE layers) (Kadooka et al., 2016a), (d) assembled MUDEAs (2 DE layers each) (Imamura et al., 2017), (e) & (f) unimorph (Haghiashtiani et al., 2018; Sikulskyi et al., 2020), (g) pump based on zipping actuation (Schlatter et al., 2020), (h) bending without passive layer (Sikulskyi, Yu, et al., 2021). (a) and (g) are fabricated through aerosol jet and inkjet printing, respectively; the rest are printed through contact dispensing.

Following studies on fully printed DEAs focused on the unimorph actuator configuration to produce large deformations through bending without DEA prestretch. Due to the capability of contact dispensing to print various materials, it was quickly applied to stack layers of DEAs. Therefore, the first fully printed unimorph actuator was of the stacked type (Kadooka et al., 2016a). Actuators with up to 10 DE layers made of polyvinylidene fluoride terpolymer P(VDF-TrFE-CFE) and silicone/carbon nanotubes (CNT) composite electrodes were fabricated on top of a 3M 810 scotch tape as a passive layer through the developed printing process. Moreover, materials' compatibility, wettability, and effects of various printing parameters on DEA quality were discussed.

The low electric field reached during the testing (Table *2.5*) can be explained by the defects in the thin DE layers (15 μm). Furthermore, stacked DEAs are prone to even lower dielectric strength measured by the first breakdown in one of the layers due to the transducer's increased total area. The small thickness of DE layers was driven by utilized DE material, which usually needs to be dissolved in a large amount of solvent, such as methyl ethyl ketone (MEK) or dimethyl sulfoxide (DMSO), to be printed (Srinivasaraghavan Govindarajan et al., 2021).

The developed fabrication process was utilized by the researchers to produce numerous unimorph actuators with two DE layers and a printed poly(methyl methacrylate) (PMMA) passive layer (Imamura et al., 2017). The DE material was dissolved even more, i.e., 5.55 wt.% vs. previously used 10 wt.% solution in MEK. Despite the further reduced thickness of the dielectric layers (10.6 μm), about 85% of fabricated DEAs could withstand the same applied voltage of 550 V. Thus, the reached electric field was greatly increased by limiting the number of layers to two and lowering DE material viscosity. Moreover, the reported performance deviations were 10% for the tip deflection and 15% for the blocked force (Kadooka, 2017). The actuators were then assembled into variable stiffness actuators that utilized the electrostatic chucking effect for soft grippers. Several things can be learned from these two studies. Firstly, printing dielectric and electrode layers using low-viscosity solutions allows for improved thickness uniformity across the actuator and printing repeatability, important to prevent premature breakdown, especially in printed stacked DEAs. Secondly, dielectric and electrode layers' comparable thicknesses simplify stacking the actuator. Finally, low driving voltage allows for easy interconnection of electrode layers and separation of

oppositely charged electrode connections to eliminate printing additional elements and insulation.

An attempt to fabricate a stacked DEA with elastomer DE and passive layer (from now on, "compliant passive layer") was shortly undertaken (Klug, Solano-Arana, Mößinger, Foerster-Zuegel, & Schlaak, 2017). While no actuation was shown, a 100 μm printed compliant passive layer followed by two 40 μm electrodes and two 80 μm elastomer layers were printed using a modified motor-driven printer. Prior to printing the stacked layers, a 30 μm elastomer film was printed and evaluated for thickness uniformity using a contact profiler. It was shown that viscous materials tend to possess higher thickness at the printing head travel edges due to the printing speed profile.

The following study on AM of DEAs focused on a unimorph actuator with a single DE layer and implemented various techniques and actuator design aspects that can potentially benefit the fabrication of various DEA configurations (Haghiashtiani et al., 2018). These techniques and aspects include a printed and compliant passive layer, UV curable elastomer and electrode materials, improved DE-electrode adhesion through employing a UV curing agent, hydrogel for compliant, printable, and thick electrodes, and dielectric composite for improved DE properties. In agreement with the discussed DEA modeling, a compliant passive layer made of Loctite 5084 silicone possessed a higher thickness (313 μm) to provide a sufficient structural asymmetry to the unimorph actuator. Despite the actuator's large overall thickness, it achieved considerable actuation deformation thanks to the material's compliance. While the thick DE layer (516 μm) should have minimized the defects' effects, its non-uniformity can be observed from the shown fabrication process. As a result, a relatively low electric field to material's

breakdown strength ratio (similar to the previous study) was reached. The uneven thickness of the DE layer was likely formed because of the lower layer's poor surface flatness. While the elastomer offset layer was printed around the thick electrode (458 μm) to level the actuator for the following layer, printing two materials in level with a smooth connection in-between is challenging and usually requires compatible materials and a sophisticated AM system. Finally, the application of UV light curing and improving adhesion between materials was accomplished and evaluated. Overall, by investigating numerous techniques and materials, the study demonstrated the effectiveness of some and unveiled challenges of others.

By analyzing conducted studies, it can be concluded that the DE film's quality plays a critical role in reaching a high electric field that can lead to a larger deformation. Remaining the goal of low driving voltage, a minimum elastomer's thickness needs to be chosen such that the utilized AM technique and apparatus provide appropriate film uniformity and avoid degrading DEA performance.

To address the low reachable electric field applied to the 4D printed DEAs, elastomer thickness uniformity needs to be the aim of DEA design and fabrication. It was shown that utilization of an advanced microdispensing AM system and modified conductive polymer materials allows to produce uniform layers and thin electrodes, considerably improving DEA performance (Sikulskyi et al., 2020). The electrode consisted of an aqueous solution of conductive polymer PEDOT:PSS doped with surfactant plasticizer Triton X-100. A high water content (~95 wt.%) resulted in a greatly decreased thickness during curing. Thin electrodes eliminate the need in the offset elastomer layers, simplifying the printing process and maintaining flatter surfaces for depositing the

following layers. Employing this principle, a single-layer unimorph DEA was printed on a stiff substrate (Kapton tape). Having a 100 μm DE layer, the actuator reached a twice higher electric field and similar tip deflection compared to the previous studies. Despite providing the improved manufacturability of single layer DEAs and their actuation, thin electrodes limit the possibility of stacking DEAs and require printing several layers for electrode connections with a voltage source.

The first demonstration of DEA's fully inkjet printing was shown by Schlatter, *et al.* (Schlatter et al., 2020). The printing was performed using three materials: electrode and elastomer for DEAs and sacrificial material for patterning fluid channels of the fabricated electromechanical devices. Materials were adjusted to enable inkjet printing of each layer directly on the previous one without any special treatment. The finished devices possessed 30 μm silicone (Sylgard 184) films and patterned electrodes with small features. More importantly, a large electric field was achieved in the printed DEA. Assuming that all the dielectric liquid leaves the channel during the actuation, electrodes' separation would be 60 μm (two 30 μm silicone films). In this case, an electric field of about 76% of the breakdown strength was reached at an applied voltage of 3.8 kV, making the printed devices the most high-quality DEAs to date.

Meanwhile, to facilitate 4D printing of DEAs, the applicability of a more affordable dispensing apparatus was investigated (Mekonnen et al., 2021). While a limited actuator quality with the 100 μm DE layer was observed, applying the thin electrodes for thicker DE layers showed a considerable improvement in the performance of a unimorph actuator with a compliant passive layer. The printed compliant passive layer was fabricated from the same material, i.e., the same stiffness, but double the DE layer's

thickness. Thus, the study illustrated the ability of DEAs to deform a relatively thicker soft body as a step towards biomimetic robots.

Lastly, as AM opens new rapid prototyping possibilities, it can be employed for potential DEA soft robotic application concepts and designs. Consequently, one novel approach to generate bending deformation without passive elements utilizes contact dispensing (Sikulskyi, Yu, et al., 2021). This allowed for a microdispensing pneumatic apparatus to coat thin auxiliary elastomer layers (<40 µm) and specially patterned electrodes (8-10 µm) along with small electrode traces.

The major aspects of the to-date fully printed DEAs as well as the reached electric fields are summarized in Table *2.5*. Despite the limited number of fully printed DEAs, their comparison allows drawing some correlation between the utilized AM methods, apparatus, configurations, materials, and quality of the actuators.

Table 2.5 Fully printed DEAs.

(Ref.)	Dispensing apparatus[a]	DEA configuration	DE material (thickness)	Electrode material (thickness)	Deformation @ voltage (E/E_B)[b]
(Jiyu, 2016)	Customized Fab@Home (motorized & pneumatic)	Prestretched (single-layer) before printing electrodes	PDMS KE-1283 (215 μm)	Carbon grease (1 mm)	12% thickness actuation @ 7.6 kV (-)
(Sebastian et al., 2016)	Optomec (Aerosol jet)	Non-prestretched (single-layer)	PDMS Elastosil P7670 (>60 μm)	Reduced graphene oxide ink (-)	Visible area expansion @ 3.1 kV (-)
(Kadooka, Imamura, & Taya, 2016a)	Musashi Engineering SHOTminiΩx 3-axis robot & ML-808GX dispenser (pneumatic)	Unimorph (10 DE layers, stiff passive layer)[c]	P(VDF-TrFE-CFE) (15 μm)	MWCNT/PDMS (12 μm)	Tip deflection: 0.5 mm @ 550 V (9.2% E_B)
(Imamura, Kadooka, & Taya, 2017)		Unimorph (2 DE layers, printed stiff passive layer)	P(VDF-TrFE-CFE) (10.6 μm)	MWCNT/PDMS (18.7 μm)	Tip deflection: ~1.5 mm @ 550 V (13% E_B)
(Klug, F. et al., 2017)	Customized "Ultimaker Original+" (motorized)	Unimorph (2 DE layers, printed soft** passive layer)	PDMS (80 μm)	Graphite (40 μm)	(no actuation)
(Haghiashtiani, G. et al., 2018)	Fisnar 3-axis robot & Nordson EFD dispenser (pneumatic)	Unimorph (single-layer, printed soft passive layer)	PDMS Loctite 5039/ Semicosil 912 with BaTiO₃ (516 μm)	Ionic hydrogel ink (304-458 μm)	Tip deflection: 9.2 mm @ 5.44 kV (12.9% E_B)[d]
(Schlatter, Grasso, Rosset, & Shea, 2020)	Jetlab 4XL (Inkjet)	Fluidically driven (single-layer with elastomer consisting of 2 layers with a dielectric fluid in-between)	PDMS Sylgard 184 (2x30 μm)	Carbon black/PDMS (2.5 μm)	Operating @ 3.8 kV (75.9% E_B assuming no fluid remaining between DE layers during actuation)

Table 2.5 Fully printed DEAs (cont.).

(Sikulskyi, Yu, Rojas-Nastrucci, Park, & Kim, 2020)	nScript 3Dn Series (pneumatic)	Unimorph (single-layer, stiff passive layer)	PDMS Sylgard 184 (100 μm)	PEDOT:PSS/ Triton X-100 (<20 μm)	Tip deflection: 9 mm @ 2.4 kV (27% E_B)
(Mekonnen, Sikulskyi, Ren, Holyoak, & Kim, 2021)	HYREL 30M (motorized)	Unimorph (single-layer, printed soft passive layer)	PDMS Sylgard 182 (340 μm)	PEDOT:PSS/ Triton X-100 (15 μm)	Tip deflection: 6.2 mm @ 6.5 kV (21.3% E_B)
(Sikulskyi, Yu, Rojas-Nastrucci, & Kim, 2021)	nScript 3Dn Series (pneumatic)	Folding electrodes (single-layer, no passive layer)	PDMS Sylgard 184 (238 μm)	PEDOT:PSS/ Triton X-100 (8-10 μm)	Tip deflection: 0.55 mm @ 5.2 kV (24.5% E_B)

[a] The utilized AM method is contact dispensing (motorized or pneumatic) unless specified differently.

[b] E/E_B is the maximum electric field applied to the actuator relative to DE's breakdown strength. The applied electric field is calculated considering DE's decreased thickness during the actuation, i.e., using the current configuration strain equation for linear DEA materials (Equation 3).

[c] A passive layer is called stiff if its Young's modulus is more than one order of magnitude higher than of the DE layer. Otherwise, the passive layer is called soft.

[d] Breakdown strength is estimated based on an average value of the two mixed elastomers considering the studied effects of barium titanate nanoparticles on elastomer dielectric composite (Sikulskyi, Mekonnen, El Atrache, Divo, & Kim, 2021).

2.6.5. Summary of AM Methods for 3D Printed DEAs

By analyzing various AM methods utilized for fabricating DEAs, dispensing techniques, particularly contact dispensing, inkjet, and polyjet printing, possess capabilities to fully fabricate DEA soft actuators of various designs.

Contact dispensing is currently the most ready-to-use and flexible in terms of materials technique for 3D printed DEAs. The major drawback of contact dispensing is its dependence on the quality of the substrate or the previously printed layer, which affects the uniformity of produced films and leads to smaller reachable electric fields.

Inkjet printing was initially utilized only for fabricating thin DEA electrodes due to its specific material rheological requirements. However, recent studies have shown the fabrication of both elastomer and electrodes for fully printed DEA devices with complex 2.5D geometry. Despite some limitations and challenges of the method, such as thorough adjustments of material rheology and printing parameters, fully printed DEAs with the highest reached electric field was achieved. Therefore, inkjet printing is perceived as potentially the best method to fabricate high-quality 2.5D DEA with low driving voltage.

Despite a poor implementation of polyjet technique for printing DEAs, it is seen as the most promising technology for biomimetic soft robots with complex geometry and higher driving voltage than inkjet-printed DEAs. It can utilize a much wider range of materials than inkjet printing, producing moderately thin films and 3D structures with multiple materials while being independent of the substrate quality. It is concluded that polyjet printers' price is the major obstacle to its application, while there is practically no choice of electrode materials. Considering the successful commercialization of the technique, these aspects are currently being investigated.

2.7. Methodology

The study covers various aspects of fully printed DEAs such as actuator design and modeling; materials selection, modification, and testing; AM methods; actuator testing; novel DEA configuration. The analysis utilizes analytical, numerical, and experimental approaches, with the large focus on the latter due to the novelty of the field, numerous variables, and the need for result validation. In the following four chapters, the objectives of this dissertation are approached as described below.

- *Chapter 4 – AM of DEAs.* As discussed, current 3D printed DEAs suffer from various defects leading to premature breakdown. This chapter further discusses these defects and provides possible solutions in a recommendation manner through correlating AM methods, material manufacturability and processing, and DEA design. To validate the fidelity of the analysis, contact dispensing AM method is used to fabricate a uniform DEA soft actuator according to the stated recommendations. The actuator is tested in a cantilevered mode and compared to the current 3D printed unimorph actuators. To make the material-independent comparison between the actuators, it is performed based on electric field relative to the used dielectric elastomer's breakdown strength.

- *Chapter 5 – Dielectric Elastomer Composite.* Dielectric elastomer mixed with highly dielectric or conductive particles is one of widely utilized approaches to boost dielectric elastomer performance. To avoid lowering DE breakdown strength and clogging the printing nozzle, three-dimensional highly dielectric particles are selected as fillers for DE composites. The composites prepared with several dielectric fillers are characterized for the parameters important for DEA

application as well as used to 3D print a soft unimorph actuator with the optimized composite DE.

- *Chapter 6 – Compliant Electrode for DEA.* As a starting point, replicate a moderately compliant electrode formulation based on an intrinsically conductive polymer, validate its printability, and verify AM recommendations described in Chapter 3. To obtain a better performing DEA electrode, further softening of the electrode material is needed while maintaining conductivity and stretchability at the level sufficient for 3D printed DEAs. Several methods are employed in the chapter, including maximizing the amount of plasticizer, doping the electrodes with solvents that do not degrade used dielectric elastomer, and forming hydrogels. The effect of final improved electrode is demonstrated on 3D printed unimorph DEAs.

- *Chapter 7 – Novel Bending DEA Configuration.* As per literature review, application of bending DEAs is one of the approaches to increase deformation capabilities of 3D printed DEAs operating at lower actuation strains and without prestretch. To increase actuation deformation of 3D printed bending DEAs by eliminating the stiffening elements in configurations such as unimorph/bimorph actuators, a novel approach to utilize electrostatic pressure is proposed and studied in the chapter. Numerical parametric study is conducted to understand the relation between the design of the novel configuration and out-of-plane motion capabilities. Finally, the numerically designed bending DEA is 3D printed and tested to validate the concept.

3. AM of DEAs

This chapter presents the major work accomplished on 3D printing of DEAs, including single-, multilayer, and composite DEAs, printed through various contact dispensing apparatus.

3.1. AM Considerations for DEAs

This section draws the major AM consideration for DEAs and classifies them based on their sources in the following subsections. Based on the consideration, a general printing procedure can be illustrated (Figure 3.1).
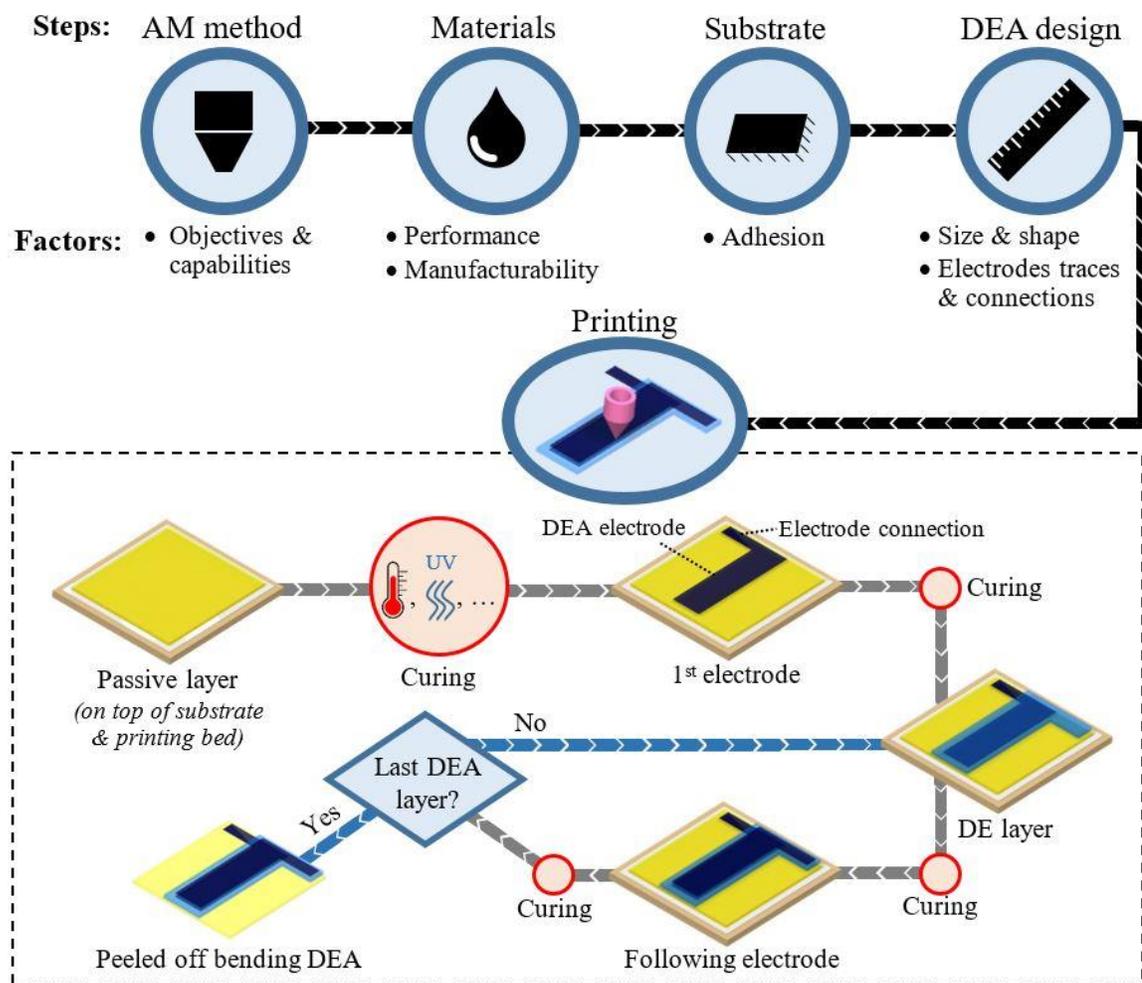
Figure 3.1 General procedure for fully printed unimorph DEA soft actuators.

3.1.1. Materials

From the manufacturability perspective, material selection can be limited by the chosen AM technique as shown in Table *2.4*. As such, inkjet materials need to be mixed with nonvolatile solvents and surfactants, polyjet materials are mostly limited to those commercially available, while contact dispensing remains the most flexible in terms of material selection. However, other technological aspects must be considered when choosing DEA materials. These aspects include material compatibility and tendency to manufacturing defects.

DEA material incompatibility can occur during the printing process in the form of wettability or solubility. The wettability issue is caused by the fact that DE materials are mostly hydrophobic and numerous conductive inks are hydrophilic. Chemically modifying electrode materials or treating cured dielectric surfaces with plasma are among commonly utilized approaches (Shrestha et al., 2018). Proper wettability is one of the key factors for adhesion between the DEA layers and therefore, for actuators' long-term performance. Solubility happens when electrode and dielectric materials can dissolve each other, e.g., when both materials have elastomer bases thinned with a solvent. If the concentration of solvent in materials is too high, a newly coated layer can partially dissolve the previous layer degrading its thickness uniformity and possibly interfering further curing. In contrast, the right amount of solvent will not considerably dissolve the previous layer but may improve adhesion between the printed layers.

Defects are another source of poor DEA quality. While electrode defects usually degrade actuator performance, defected dielectric often leads to its failure. The major material-wise sources of premature breakdown in dielectrics are air bubbles and foreign

particulate, e.g., dust in DE layers. As for conventional DEA manufacturing, a clean environment is vital for DE films to be dust-free. Thus, material degassing is a common procedure in thin film fabrication. This can be accomplished during the mixing process in various types of centrifugal mixers, by means of vacuum or both. The degassing time mainly depends on elastomer viscosity and the desired thickness of the printed DE layer. Material transfer into the printer reservoir could also trap air into the silicone. For this reason, utilization of special equipment, such as vacuum syringe chargers, or secondary degassing of the material loaded in the syringes, is preferred. Another common defect comes from materials shrinkage during curing. It can lead to various actuator shape alteration, e.g., a widthwise curvature in unimorph actuators. Such a defect results in model-experiment mismatch, especially at lower electric fields. At higher applied field, the effect weakens and almost disappears (Imamura et al., 2017). Nevertheless, DE and electrode materials with low shrinkage are preferred.

Lastly, utilization of particulate composites for DE and especially electrodes is not a rare occasion. Unevenly dispersed large particles result in variable material properties and flow rate, causing uneven thickness and clogging printing tips. Based on their size, particles can be dispersed during mixing with the matrix (high-speed or planetary mixing) or by sonication.

3.1.2. Substrates

Peeling off printed parts without damaging them is a critical fabrication step, particularly for thin films made of compliant materials. An approach of weakening adhesion between the substrate and printed elastomer is widely utilized. Using non-stick surfaces such as polytetrafluoroethylene (PTFE) and various film liners of double-sided

tapes as printing substrates, moderately thin and compliant parts can be peeled off. While most silicones have relatively high stretchability and strength, electrode layers are typically more fragile. Therefore, additional considerations must be used for this peeling off process. It is especially true if elastomer layers are not thick and stiff enough to limit the overall part's deformation during the peeling off process below the electrode material's stretchability limit. As a solution, various chemical treatment methods have demonstrated improving film release in the case of thinner and more compliant parts or highly adhesive substrates (S. Vudayagiri & Skov, 2014).

For unimorph actuator configuration, several examples of fully printed DEAs utilize various tapes (e.g., Scotch, Kapton, PE, PET, Mylar) as printing substrates that restrict excessive deformation during the peeling due to their high stiffness (Kadooka et al., 2016a). These tapes are then used as stiff passive layers. When printing thin DEA layers on various tapes, especially on films with no adhesive layer, utilization of a vacuum plate is a useful feature. For actuators with compliant printed (typically relatively thick) passive layers, the peeling can be performed by utilizing chemical treatment, non-stick films (Sikulskyi, Yu, et al., 2021), or sometimes without special measures (Mekonnen et al., 2021).

3.1.3. DEA Design Considerations

DEA and soft robot designs also affect their fabrication processes. The main considerations are the thickness of DE layers, design size (area occupied on the printing bed), soft robot geometry, and degree of actuation/sensing distribution.

Most common defects in DE films include uneven thickness and dust particles. Thickness uniformity is dictated by a fabrication technique and equipment accuracy and

is typically evaluated to a certain absolute value. Dust is defined as an air-suspended particles below 75 µm in diameter (ISO, 2020). Inside the facilities with a normal air filtration system, dust particles rarely exceed 5 µm (Fisk, Faulkner, Sullivan, & Mendell, 2000). Therefore, the risk of a premature breakdown grows with the decrease of the dielectric film thickness. It can be concluded that the minimum DE thickness must be chosen according to the utilized AM method, apparatus, and dust environment. This will enable 4D printing of high-quality DEAs with consistent performance, i.e., such that they can reach high electric fields with known probability. It should be noted that dust diameter is not the actual size but the particle aerodynamic diameter which is "the diameter of a hypothetical sphere of density 1 g/cm^3 having the same terminal settling velocity in calm air as the particle in question, regardless of its geometric size, shape, and true density" (WHO, 1999). Hence, the dust effect on DEA breakdown strength can often be underestimated by neglecting actual dust particles' size and shape. Utilization of an air filtration system removing particles an order of magnitude smaller than DE thickness is preferred.

The upper thickness boundaries of electrode and DE layers are limited by material viscoelastic properties, particularly shear storage modulus (Schaffner, Rühs, Coulter, Kilcher, & Studart, 2017), that do not allow materials to spread during fabrication. All other things being equal, lower viscosity materials are preferred during printing to level the thickness. Lastly, printing each layer in one go can be preferred when the material has a high solvent content. On such occasions, successive printing of the same material can dissolve previously coated layers and cause an uneven thickness. The rest of the considerations affect certain AM methods. DEA area-wise size is important for contact

AM methods. As the printing area increases, maintaining an appropriate gap between the printing tip and substrate demands improved printing bed's flatness and levelness.

Soft robot geometries that include complex three-dimensional structures with curved elements limit the variety of appropriate AM techniques. Contact dispensing of viscous materials can be utilized for moderately curved surfaces depending on a printer's number of axis. Polyjet printing is capable for this task using support material. Nevertheless, the fabrication of DEAs on horizontal flat surfaces is highly preferred.

Lastly, distributed actuation/sensing and local operation are intrinsic properties of biomimetic soft robots. Being electrically driven, DEAs require electrodes to be connected by traces which leaves less space for DEAs themselves. Moreover, considering high driven voltages, these traces need to be isolated from each other and electrodes. Preferably, a utilized AM method should accurately fabricate small features for smaller electrode traces and their proper isolation by DE material.

3.1.4. Multilayer Unimorph DEA (MUDEA)

As AM techniques are layer-by-layer fabrication processes, extending manufacturing of a single-layer DEA to stacked actuators seems to be easier than for conventional fabrication. In fact, 4D printing stacked DEAs requires several technological challenges to be solved.

Thickness uniformity is one of the most important factors affecting stacked DEA fabrication. Serving as a substrate for printing following layers, an uneven printed layer can further magnify the defect. Contact AM methods are particularly susceptible here.

Currently, fully printed stacked DEAs possess comparable electrodes and DE thickness, which simplifies similarly charged electrodes' interconnection. Meanwhile,

across the literature, electrodes are often fabricated much thinner for maximum effectiveness (Mihai Duduta et al., 2016; Kovacs, Düring, et al., 2009). To avoid stacking layers of conductive materials for electrode connections, possible solutions are the utilization of different electrode materials or printing approaches, e.g., printing comparable thickness electrode connections but dissolving the same electrode material for actuator electrodes.

Besides the factors that enable the fabrication of stacked DEAs, manufacturing process time is of great interest. While some fabricated stacked DEAs possess from hundreds to over a thousand layers (Mihai Duduta et al., 2019; Kovacs, Düring, et al., 2009), multilayer actuators are stacked by a much smaller number of layers within the order of 10 (Mihai Duduta et al., 2016). Dispensing AM techniques consist of printing, curing, and auxiliary processes. While printing speed is a matter of a particular dispensing method, the curing and auxiliary processes can be shortened. Namely, UV curable materials are preferred to quickly solidify to the degree when the following layers can be printed. The final curing can then follow the last printed layer. Auxiliary processes, for instance, can include plasma surface treatment for improved wettability and material bonding. Thus, material modifications are preferred over auxiliary steps between printing layers.

3.2. Printing High-Quality Single-Layer Unimorph DEA (UDEA)

To validate the importance of described AM considerations, a unimorph DEA-based actuator was manufactured and tested (Sikulskyi et al., 2020). Printing was performed in a lab environment utilizing commercial PDMS to address dust particles and material imperfection defects to a certain extent. The selected two-component PDMS (rubber

base, Part A, and curing agent, Part B) was Sylgard 184 due to its low viscosity in order to even the film thickness after printing, fast curing at increased temperatures, and favorable electromechanical properties, particularly low Young's modulus (Y=1.2 MPa when mixed in the standard 10:1 ratio) and high breakdown strength (E=100 V/µm when mixed in the standard 10:1 ratio).

According to the manufacturer's instructions, manual mixing is sufficient for Sylgard 184. However, the material mixed in such a way that it contained visible, sub-millimeter air bubbles unless cured at higher temperatures, which further reduced the silicone's viscosity and removed said air bubbles. To further reduce the air bubble defects in the silicone, several techniques were applied. The first technique was mixing Sylgard 184 components in a planetary mixer, THINKY ARM-310 (Laguna Hills, CA, United States), for simultaneous mixing and degassing. This processing was performed for 30 sec at 2000 rpm and resulted in 5 to 20 µm diameter bubbles that are considerable for typical DEA elastomer films thickness (10^2-10^3 µm) (Figure 3.2a). The second technique employed a vacuum to reduce the air content in the material. Part A and Part B of the silicone were manually mixed and placed into the vacuum oven at -660 mmHg for 10 min at room temperature. The resultant bubbles' diameters were in a range of 1-5 µm with a mean value below 2 µm (Figure 3.2b). A similar performance was achieved by applying a vacuum to a material mixed in the planetary mixer for 30 sec at 2000 rpm. While effectively degassing the material, a vacuum technique is time-consuming and limits the utilization of materials with relatively short handling time in 3D printing. Therefore, the third mixing process was tested where Part A (the viscous rubber base) was degassed in the planetary mixer for 3 min at 2000 rpm. Then it was left to cool down

to room temperature before adding the curing agent, Part B, and mixed for another 30 sec at 2000 rpm. A comparable effect in terms of air bubbles was achieved with the reduced processing time from 10 to 3 min (Figure 3.2c).
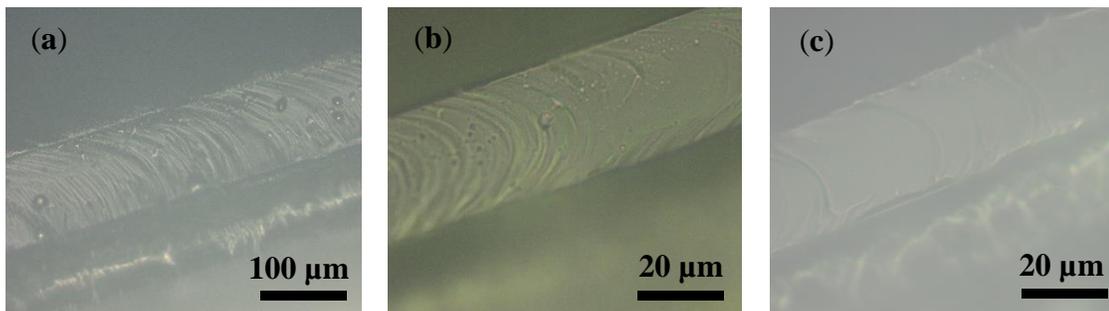
Figure 3.2 PDMS (Sylgard 184) films degassed by (a) planetary mixing for 30 sec at 2000 rpm, (b) vacuuming for 10 min at -660 mmHg, and (c) planetary mixing the rubber base for 3 min and then mixed material for 30 sec at 2000 rpm.

Single-layer unimorph actuators were fabricated according to the following procedure:

- Kapton tape with Young's modulus of 2.5 GPa and a thickness of 25.4 µm was placed on top of the printing bed and served as a substrate for the printing of consequent DEA layers. Electrodes (~10 µm) and elastomer (~100 µm) layers were printed with short curing cycles in between (Figure 3.3(a1-a5)).

- Final curing is performed after all layers are printed (Figure 3.3(a6)).

- Kapton with the cured DEA on top of it was peeled off from the printer bed (Figure 3.3(b)) and brought to the final shape by cutting off excessive Kapton (Figure 3.3(c)).

A state-of-the-art contact microdispensing printer, nScrypt 3Dn Series with a 125 µm diameter ceramic printing tip and Smartpump pneumatic dispensing system, was utilized

to additively manufacture the actuator, due to its capability to print uniform thin layers of viscous materials Figure 3.4.
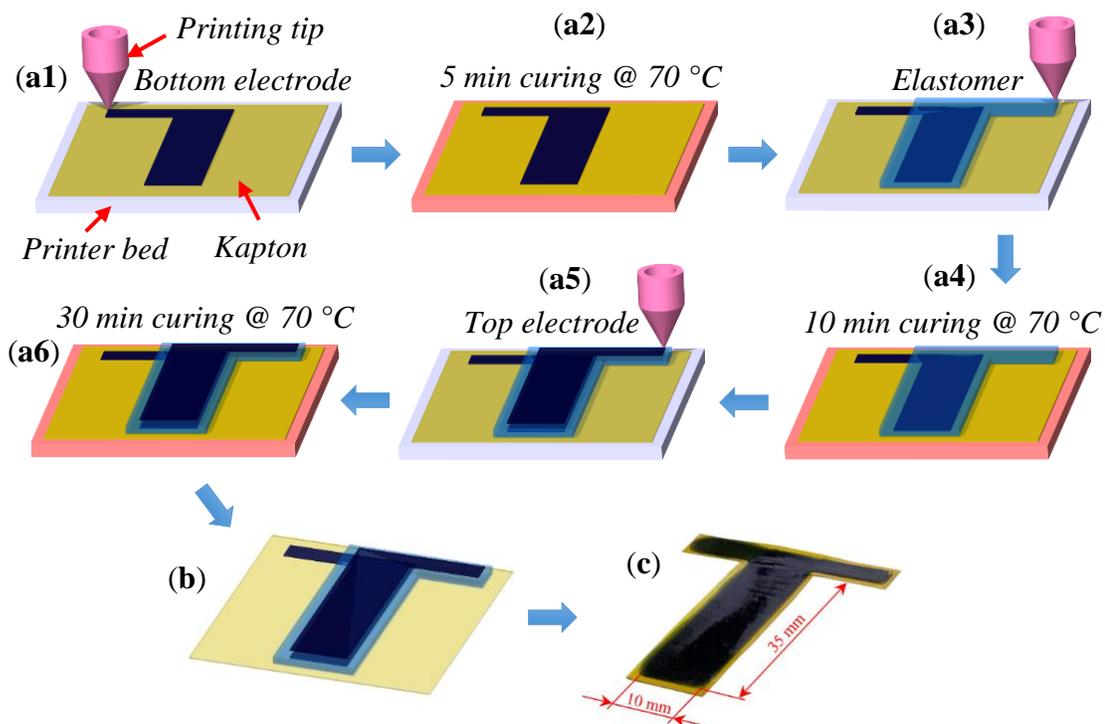
Figure 3.3 DEA unimorph actuator (a1) - (a6) printing layer sequence, (b) after printing, (c) final appearance.
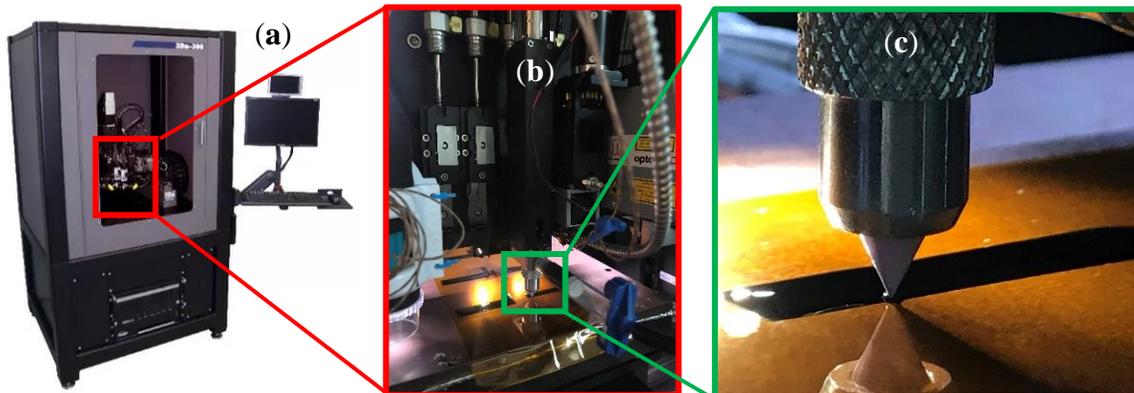
Figure 3.4 (a) nScrypt 3Dn Series microdispensing printer utilized for printing high-quality DEAs with its (b) Smartpump pneumatic dispensing head and (b) printing ceramic tip.

Printing parameters used for the actuator fabrication are stated in Table *3.1*. The printer's head valve opening was adjusted when printing the actuators until the elastomer thickness of about 100 µm was reached. The valve opening parameters are not reported in the table due to their dependents on many operational factors during each printing session. The resultant unimorph actuators were analyzed for thickness uniformity (Figure 3.5). As a result, up to 9% of thickness variation was found across several batches of printed DEAs utilizing the procedures described above.

Table 3.1 nScrypt 3Dn Series parameters for printing the DEA.

	Printing height, µm	Printing speed, mm/s	Pressure, psi	Wet thickness, µm	Dry thickness, µm
Electrode	100	30	1.3	~ 200	10
Elastomer			4.7	90	90
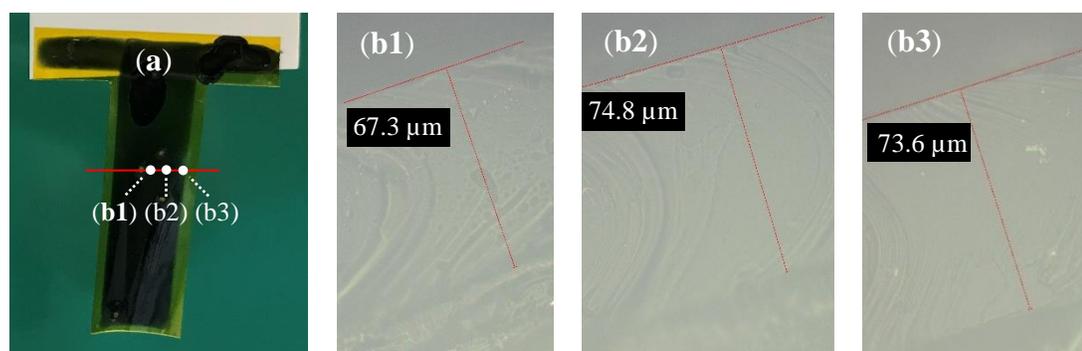
Figure 3.5 (a) 3D printed DEA and (b1-3) its cross-section thickness.

The actuators were cantilevered at the edge close to electrode connections with Kapton tape side facing down in the testing. Voltage was applied with a 200 V step using amplifier TREK® 20/20CH-S. Figure 3.6 shows the unimorph actuator, with the elastomer layer of 90 µm, in rest and deformed state at 2.4 kV applied validating electrode's feasibility. The applied voltage corresponds to 29 V/µm of the electric field,

which is 32% of breakdown strength, E_{BD}, of Sylgard 184 when mixed in 15:1 ratio (Vaicekauskaite, Mazurek, Vudayagiri, & Ladegaard Skov, 2019). Compared to previously 3D printed DEAs, about two and a half times improvement was achieved in terms of the achievable electric field relative to the DE breakdown strength (Figure 3.7).

One of the initial tests detected the actuator's design flaw as the actuators burned due to a voltage arc between the top and bottom electrodes at the left connection, where electrodes are closest to each other (Figure 3.3). Thus, some portion of this connection was covered with the elastomer as well to increase the space gap between the electrodes for all further printed actuators.

Figure 3.6 Unimorph actuator bending due to the DEA (with the 90 µm elastomer) actuation on a 5 mm grid background.
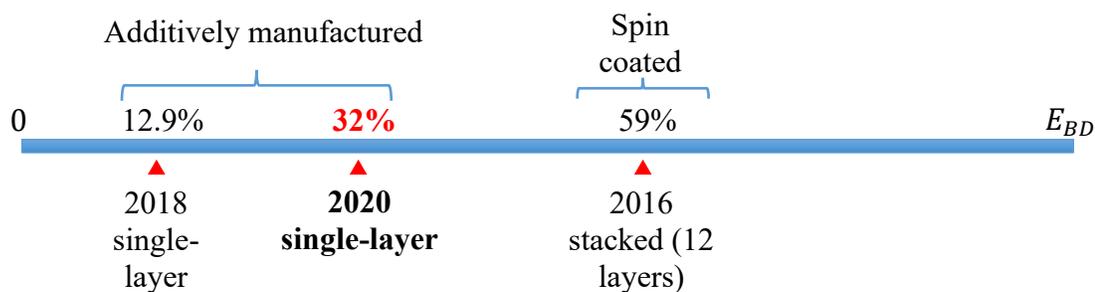
Figure 3.7 Comparison of the reached electric field during DEA actuation test relative to the dielectric elastomer breakdown strength across the literature.

3.3. Printing Multilayer Unimorph DEA (MUDEA)

The same methodology was applied to fabricating MUDEAs. The resultant actuator had two 65 µm DE layers and three 10 µm electrodes (Figure 3.8). Thanks to its high water content, electrode material could connect the first and the third similarly charged electrodes directly without additional design alterations. Further increase in layer number of the MUDEA with thin electrodes requires additional considerations as discussed in subsection 3.1.4. Printed MUDEAs showed a lower electric field achieved, $0.259E_{BD}$, than the single-layer actuator. However, compared to reported 3D printed MUDEAs, current samples achieve doubled performance in the relative electric field (Figure 3.9).
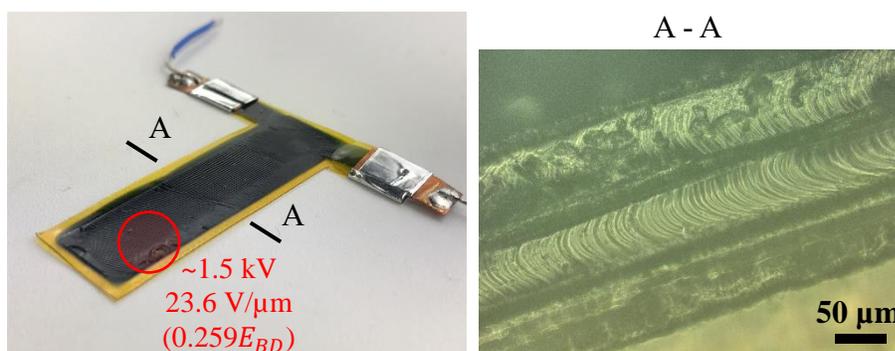
Figure 3.8 Fabricated and tested MUDEA and its cross-section.
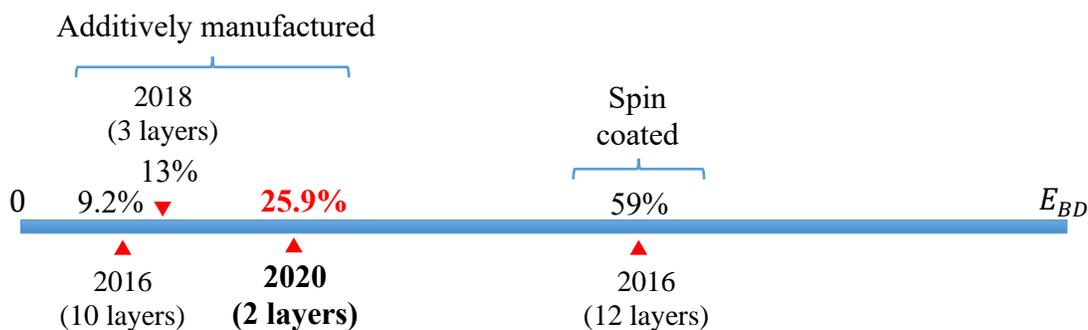
Figure 3.9 Comparison of the reached electric field during MUDEA actuation test relative to the dielectric elastomer breakdown strength across the literature.

3.4. Application of an Affordable Contact Dispensing Printer for Printed DEAs

High-precision 3D printing apparatuses, suitable for high-quality DEA fabrication, typically have a high price limiting them from the extensive application to DEA prototyping. Thus, besides state-of-the-art contact dispensing and inkjet printers and potentially applicable polyjet printers, affordable contact dispensing printers capable of printing with a wide range of materials are of great interest for DEA prototyping. Therefore, HYREL 30M printer with motor-driven contact dispensing heads (SDS-10 and SDS-30) was employed to investigate performance 3D printed DEAs fabricated using a more affordable apparatus (Figure 3.10).
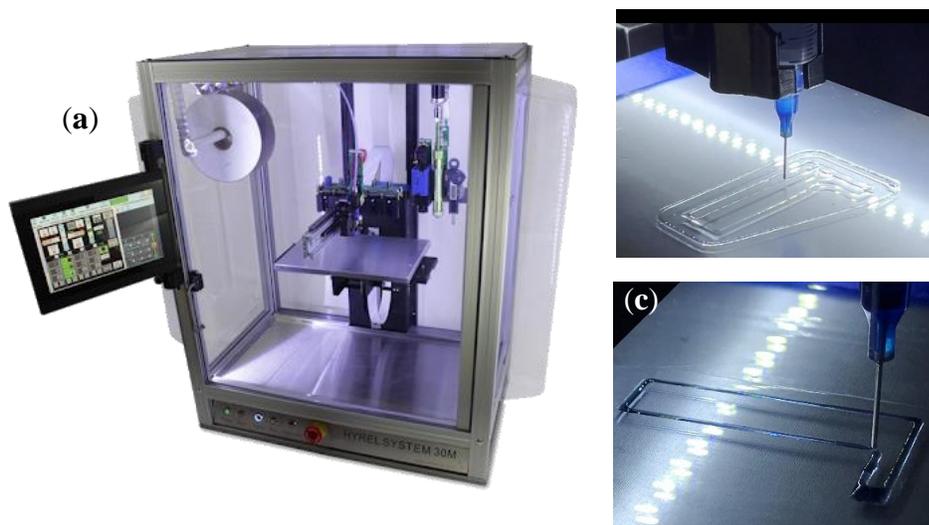
Figure 3.10 (a) HYREL 30M printer printing (b) elastomer and (c) electrode DEA materials using motor-driven contact dispensing heads.

The initial printing of DEAs unveiled several challenges associated with a simpler contact dispensing apparatus:

- Printed DEAs with about 100 µm thick elastomer layers did not result in consistently operative DEAs validating the importance of special apparatus for

printing DEAs with thin DE layers. To compensate for decreased thickness uniformity of DE layer, its thickness was increased to about 300 µm.

- Several substrates were tested. For instance, previously utilized Kapton with its strong adhesive layer required considerable peeling angle, which damaged printed DEAs. Notably, the increased thickness of DE layers resulted in larger strains at the top and bottom of DEA when bent during the peeling off. Biaxially-oriented polyethylene terephthalate (BoPET), or Mylar, was used as a thin film without an adhesive layer that was stretched equiaxially and taped on the corners of the printing bed. The utilization of Mylar made the release of the printed DEA from the printing bed effortless. However, stretching Mylar on the printing bed is an additional manual operation that does not provide repeatable results and limits DEA design optimization. In contrast, printing the passive layer reduces the number of manual operations, controls the stiffness and thickness of the passive layer for a more flexible optimization, and ensures similar adhesion between the layers. Furthermore, it was observed that with the increased thickness of DE layer and consequently increased thickness of the printed passive layer, a damage-free release of the printed actuators from various surfaces, e.g., glass or Teflon, is possible without additional surface treatment or printed material adhesion modifications.

- Lastly, in contrast to electrodes printed using the high-end nScrypt contact dispensing printer, electrodes material could not be coated in a uniform film using HYREL 30M printer. This is attributed to the uniformity of electrode material flow rate that can create initial non-uniform thickness in the coated film that

initiates electrode material to accumulate into the droplets due to its high surface tension and previously printed hydrophobic elastomer layer. To compensate for the non ideal uniform flow rate, the previously printed elastomer layer was treated with air plasma to increase the hydrophilicity of the elastomer layer. This technique resulted in uniform electrode films.

The actuators with increased DE thickness consistently deformed in the actuated state; however, they showed a limited performance compared to the previously shown actuators printed using the advanced contact dispensing printer (Figure 3.11a). Furthermore, the examined thickness profile of the printed actuator (Figure 3.11b) demonstrated a significant variation of thickness across the width of the actuator, which happened due to the low-viscosity elastomer material spread.
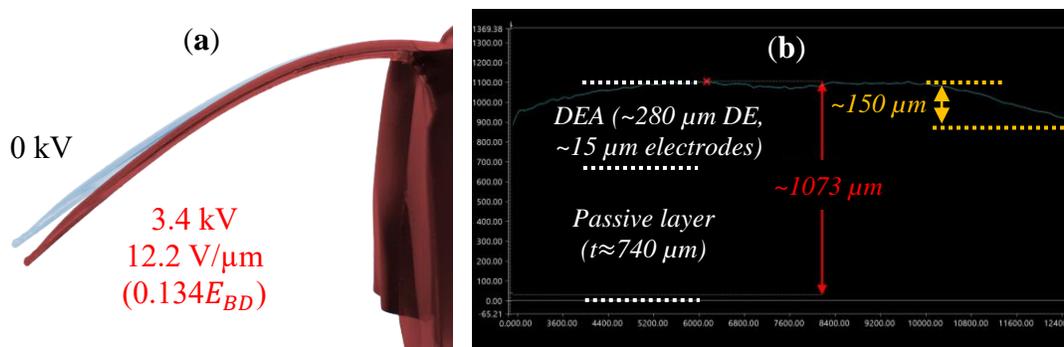
Figure 3.11 Unimorph DEA with increased DE layer thickness (a) during actuation and (b) its thickness profile.

As previously stated, the utilization of low-viscosity materials is essential for obtaining uniform films through the dispensing processes. To mitigate the material spread of the utilized low-viscosity elastomer, the width of passive and DE layers was increased and later cut to the desired shape, as shown in Figure 3.12(a-b). The actuation tests (Figure 3.12c) showed almost doubled performance and the need for controlling material

spread when printing DEAs with thick DE layers using an affordable contact dispensing apparatus.
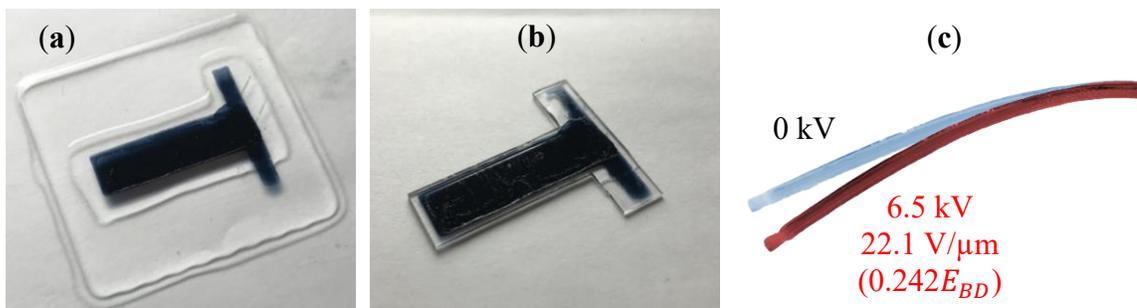
Figure 3.12 Unimorph DEA with an enlarged area of passive and DE layers for improved thickness uniformity (a) as printed using HYREL 30M, (b) cut to the design, and (c) actuated.

Table 3.2 HYREL 30M parameters for printing the DEA.

	Dispensing needle gauge	Printing height, μm	Printing speed, mm/s	Wet thickness, μm	Dry thickness, μm
Electrode	22	150	15	~ 200	10
Elastomer	18	350		300	300

3.5. Summary of AM of DEAs

A unimorph actuator was printed using contact dispensing according to the derived AM methodology. Notably, when an advanced contact dispensing system printed actuators with thin electrodes, a relatively low viscosity, degassed, and moderately thin commercial elastomer, the electric field reached the value of 32% of the elastomer breakdown strength. This value is at least two and a half times larger than for other single-layer actuators printed through contact dispensing within the literature.

Validating the need for additional considerations and printing/design improvements, MUDEAs fabricated through a similar procedure decreased their performance compared

to the single-layer actuator. Besides utilizing various types of electrode materials for printing DEA electrodes and their connection to the power source, material spread, if it occurs for the printed layer thickness, needs to be accounted for each layer.

The issue of material spread becomes critical when utilizing an affordable contact dispensing apparatus. It was shown that increased thickness of DE layers is essential for printing DEAs using a less sophisticated apparatus to achieve considerable electric field and actuation. For both thicker DE layers and MUDEAs, a potential solution is seen in printing the contour using another material to create a boundary for the desired actuator shape. To effectively maintain its shape and block DE material spread, the contour material should possess high storage shear modulus.

4. Dielectric Elastomer Composite

Integrating nano- to micro-sized dielectric fillers to elastomer matrices to form

dielectric composites is one of the commonly utilized methods to improve the

performance of dielectric elastomer actuators (DEAs). Barium titanate ($BaTiO_3$) is

among the widely used ferroelectric fillers for this purpose; however, calcium copper

titanate $CaCu_3Ti_4O_{12}$ (CCTO) has the potential to outperform such conventional fillers.

Despite their promising performance, CCTO-based dielectric composites for DEA

application are studied to a relatively lower degree. Particularly, the composites are

characterized for a comparably small particle loading range, while critical DEA

properties such as breakdown strength and nonlinear elasticity are barely addressed in the

literature. Thus, in this study, CCTO was paired with PDMS, Sylgard 184, to gain a

comprehensive understanding of the effects of particle loading and size on the dielectric

composite properties important for DEA applications. The dielectric composites'

performance was described through the figures of merit (FOMs) that consider materials'

Young's modulus, dielectric permittivity, and breakdown strength. The optimum amounts

of the ferroelectric filler were determined through the FOMs to maximize composite

DEA performance. Lastly, electromechanical testing of the prestretched CCTO-

composite DEA validated the improved performance over the plain elastomer DEA, with

deviations from prediction attributed to the studied composites' nonlinearity.

4.1. Background on Composite DEAs

Owing to their outstanding electromechanical characteristics, dielectric elastomer

actuators (DEAs) have become one of the most intensively studied and developed

electroactive polymers (EAP) (Hines et al., 2017). A common DEA can be described as a

parallel plate capacitor with compliant electrodes and a compliant dielectric elastomer in between. When voltage is applied to the electrodes, the pressure generated by electrostatic attraction compresses the elastomer through the out-of-plane direction and expands the entire actuator in the in-plane direction. To estimate the performance of DEA, a commonly accepted figure of merit (FOM) is used (Sommer-Larsen & Larsen, 2004),

$$FOM = \frac{3\varepsilon_r \varepsilon_0 E_B^2}{Y} \qquad (7)$$

where ε_r, ε_0, E_B, and Y are the dielectric elastomer's relative permittivity, vacuum permittivity, breakdown strength, and Young's modulus, respectively. The FOM assumes the elastomer to be linearly elastic with dielectric properties independent of strain to ease DEA performance estimation.

As per Equation (7), the FOM entirely depends on DEA elastomer material properties, with acrylic and silicone elastomers being the most widely used to achieve high actuation performance. While acrylic DEAs usually provide larger actuation deformation due to higher relative permittivity and compliance, silicone DEAs possess more stable time- and temperature-dependent properties, longer lifetime, and often higher specific energy density. These properties make silicone a more suitable elastomer material for practical implementation and prospective DEA commercialization (Madsen et al., 2016). Although currently available commercial silicones can produce DEAs with reliable and consistent characteristics, industrial implementation requires elastomers that produce higher actuation forces and deformations. Thus, several methods, such as adding highly dielectric (Barber et al., 2009; Zhou & Jiang, 2020) and conductive fillers (Panahi-Sarmad, Zahiri, & Noroozi, 2019), blending elastomers with polymers (Vaicekauskaite et

al., 2019), as well as chemically modifying elastomers (Shintake et al., 2019; Yu, Madsen, Hvilsted, & Skov, 2015) are used to improve silicones' dielectric and mechanical properties. Although an increase in permittivity can be attained using these methods, other material properties, namely higher Young's modulus and lower breakdown strength, can unfavorably affect the actuation performance. Nevertheless, in dielectric composites, these negative drawbacks can be mitigated through an optimized amount of evenly dispersed particles.

Table 4.1 Properties of bulk $BaTiO_3$ and CCTO materials.

Filler	Relative Permittivity (−)	Young's Modulus (GPa)	Breakdown Strength (V/µm)	Electrical Conductivity (S/cm)
$BaTiO_3$	6000 (Madsen et al., 2016)	67 (Sakakibara et al., 1994)	2–24 [a] (Branwood, Hurd, & Tredgold, 1962; Scott et al., 1994; Tunkasiri & Rujijanagul, 1996)	$1–2.5 \times 10^{-9}$ (Ertuğ, 2013a, 2013b)
CCTO	10,000–100,000 (Ahmadipour, Ain, & Ahmad, 2016; Subramanian, Li, Duan, Reisner, & Sleight, 2000)	256 (Ramírez et al., 2010)	0.05–0.2 [a] (Cheng et al., 2012; T. Li, Chen, Chang, Hao, & Zhang, 2009; Tang, Wu, Huang, & Li, 2017)	5×10^{-8} [b]

[a] Values vary based on crystal size, purity, and testing ceramic film porosity.
[b] Calculated from the data in (Samarakoon, Govindaraju, & Singh, 2019).

Among traditionally utilized fillers, titanium-based ferroelectric particles have demonstrated the ability to increase elastomer's permittivity (Madsen et al., 2016). Barium titanate ($BaTiO_3$) is a particularly successful and commonly employed filler in dielectric composites due to its high relative permittivity, averaging around 6000 (Jung rag, Han, & Lee, 2009; Lotz, Matysek, Lechner, Hamann, & Schlaak, 2008). However, calcium copper titanate $CaCu_3Ti_4O_{12}$ (CCTO) recently received exceptional attention

attributed to its immense dielectric permittivity, which varies between 10,000 and 100,000 for pure materials and as high as 400,000 with chemically doped modifications (Ahmadipour et al., 2016). Unlike $BaTiO_3$, CCTO-based composites are relatively unexplored for DEA application. Some studies investigated the effects of filler loading on polymer composites by using single sized CCTO particles (Babu, Singh, & Govindan, 2012; Duan et al., 2016; Romasanta et al., 2012; Sindhu Vudayagiri et al., 2014; Wan et al., 2017; J. Wang, Chao, Li, Feng, & Zhao, 2016; Y. Y. Zhang et al., 2019), while others investigated the effect of particle size by using fixed weight fraction (G. Wang et al., 2015; Y.-Y. Zhang et al., 2019). Furthermore, to the authors' knowledge, only one study on filler loading, up to 9 wt.%, in CCTO/PDMS composites presents the breakdown strength as a critical parameter for DEAs (Sindhu Vudayagiri et al., 2014). In general, consistent results were not observed for filler loading effects in most cases within the studied range. However, for maximum CCTO/PDMS dielectric composite performance, extended range of filler loadings and different particle sizes need to be studied to identify optimum particle loading. Therefore, this work aims to provide a more comprehensive analysis of CCTO-based composites for DEA applications by meticulously studying particle loading effects (for a wide range of filler loading before anticipated mechanical percolation thresholds (Fralick, Gatzke, & Baxter, 2012)) for different particle sizes (specific surface area). Composites are characterized through the FOMs accounting for the main DEA properties, including the breakdown strength. Additionally, $BaTiO_3$ particles are used as a benchmark for dielectric composites. To adequately analyze experimental results, properties of bulk $BaTiO_3$ and CCTO are collected in Table *4.1*. To illustrate the effectiveness of CCTO-based DEAs, the optimum filler loadings are

determined for various DEA applications by the FOMs and validated through biaxial electromechanical testing. Finally, as DEAs can operate at high strains (e.g., in prestretched configurations), composites' nonlinear elasticity is addressed through their tangent moduli to quantify the stiffness reinforcement at various particle loadings and strains.

4.2. Materials and Methods

Primary materials for dielectric composites are listed below:

- PDMS, Sylgard 184 (Dow Inc., Midland, MI, United States, part #4019862), number average molecular weight of 27,000 (Santiago-Alvarado, Cruz-Felix, Iturbide, & Licona-Morán, 2014), elastomer matrix of dielectric composites. As a widely used commercial PDMS for DEA application, Sylgard 184 was chosen due to its moderate dielectric and mechanical properties, low polydispersity and branching, low pre-cured viscosity (3.5 Pa-sec), and fast curing in the presence of temperature. The latter two properties allow to disperse particles using simple fabrication methods and prevent particles from settling down during the curing process, respectively.

- $BaTiO_3$ (TPL Inc., Albuquerque, NM, United States, HPB-4000), near-spherical particles with a mean diameter of 0.42 μm and tightly packed size distribution (Figure 4.1a), specific surface area of 4 m^2/g, density of 6 g/cm^3, purity of 99.5%, and permittivity of 6000.

- CCTO_#1 (Stanford Advanced Materials Corp., Lake Forest, CA, United States, part #19185478), random morphology, low aspect ratio particles, with a mean

effective diameter of 0.72 µm (Figure 4.1b), specific surface area of 1.74 m^2/g,

density of 4.7 g/cm^3, purity of 99.5%, and permittivity range of 9600–12,000.

- CCTO_#2 (Bonding Chemical, Katy, TX, United States, part #535616), random

  morphology, low aspect ratio particles, with a mean effective diameter of 1.8 µm

  (Figure 4.1c), specific surface area of 0.28 m^2/g, density of 4.7 g/cm^3, purity of

  98.2%, and permittivity range of 9600–12,000.

Supplemental materials for film preparation and actuation test:

- Poly(acrylic acid) (MilliporeSigma, Burlington, MA, United States, part #523925)

  aqueous 35 wt.% solution of poly(acrylic acid) used for a sacrificial layer in the

  film preparation procedure.

- Isopropanol (M.G. Chemicals Ltd., Burlington, ON, Canada, part #824) used for

  dissolving poly(acrylic acid).

- Carbon conductive grease (M.G. Chemicals Ltd., part #846) used as pre-stretched

  DEA electrode material with a resistivity of 117 Ω·cm.
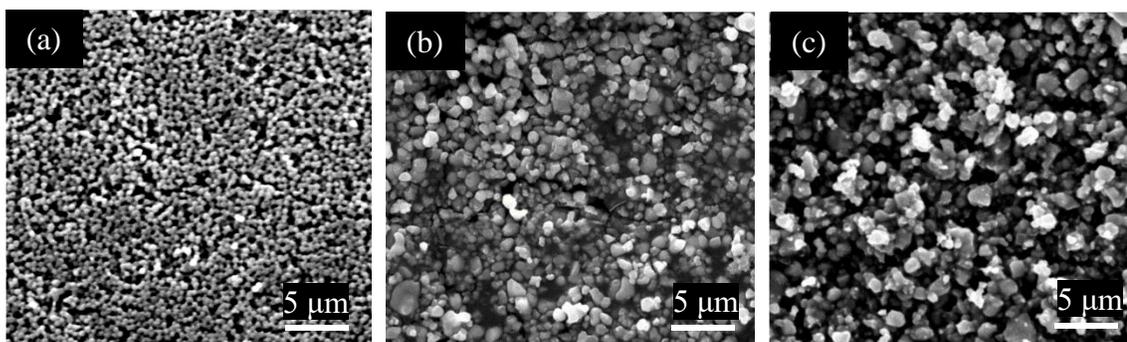
Figure 4.1 SEM images of dielectric particles: (a) BaTiO$_3$ (d$_{avg}$= 0.42 µm), (b) small CCTO (d$_{avg}$= 0.72 µm), (c) large CCTO (d$_{avg}$= 1.8 µm).

As seen in Figure 4.1, both CCTO are considerably more polydispersed compared to

BaTiO$_3$. A more detailed analysis on fillers dispersity is conducted (Figure 4.2) to

illustrate similar degrees of size distribution for CCTO fillers and validate the legality of their comparison based mainly on their size (specific surface area). Considering the relatively small aspect ratios of the CCTO particles, the significance of their shape on the investigated composite's properties was dismissed in the analysis (Fu, Feng, Lauke, & Mai, 2008; Z. Wang, Keith Nelson, Hillborg, Zhao, & Schadler, 2013).
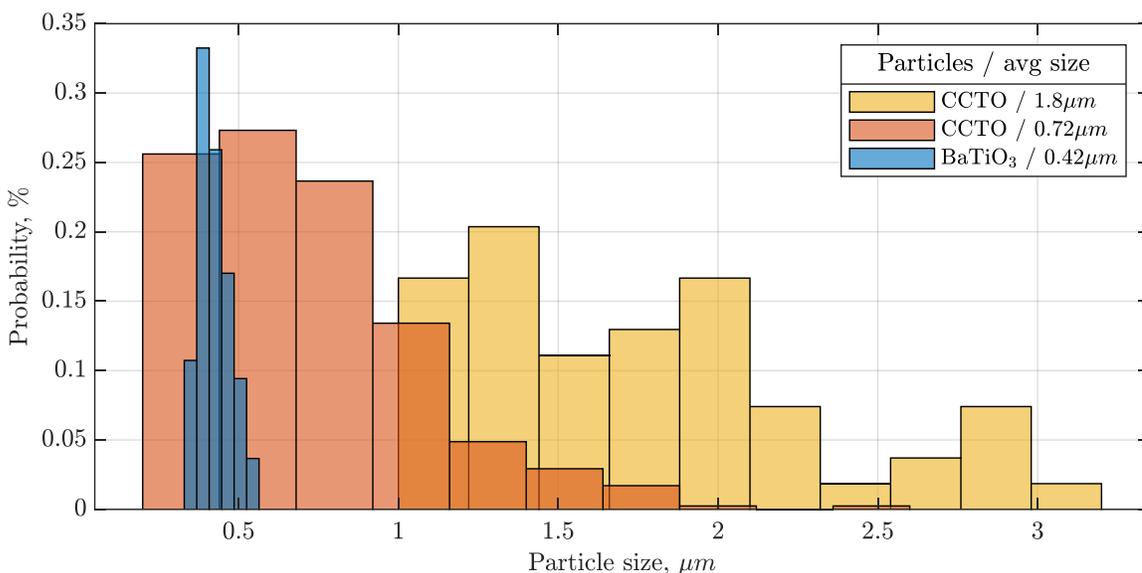
Figure 4.2 Size (effective diameter) distribution of particles used for dielectric composites.

4.2.1. Composites Mixtures and Film Preparation

For each of the three fillers, seven composite films with particle loading of 2, 5, 10, 15, 20, 30, and 40 wt.% were prepared. Initially, particles were mixed with the rubber base of Sylgard 184 (Part A) inside the filtration glove box Cleatech Series 2400 (Orange, CA, United States) and dispersed in using a planetary mixer THINKY ARM-310 (Laguna Hills, CA, United States) for 10 min at 2000 rpm. Then, Sylgard's curing agent (Part B) was added in a 15:1 (A:B) ratio to Part A to improve the FOM of the plain silicone (Vaicekauskaite et al., 2019), but mainly to extend silicone handling time before

curing. The latter made it possible to evenly disperse particles and fabricate high-quality thin composite films by blade casting method according to a well-developed technique (Rosset et al., 2015).

- 125 µm PET films were placed on a vacuum plate to ensure their flatness.

- A sacrificial layer was applied using an applicator, Zehntner ZUA2000, on each PET film. Sigma-Aldrich 35 wt.% poly(acrylic acid) was mixed with isopropanol in a 1:6 ratio to reach 5 wt.% of poly(acrylic acid) in the sacrificial solution.

- As the sacrificial layer dried out, material compositions were applied by manually operating the applicator. By setting the applicator to 500 µm, films with thicknesses of about 320 µm (thick film) were produced for mechanical and dielectric permittivity testing. For breakdown strength and biaxial electromechanical tests, 100 µm thick films (thin film) were produced by setting the applicator to 200 µm. It was noticed that higher application speed for the manually operated applicator provided better thickness evenness of the film.

- Finally, samples were cured in Grieve SA-550 air furnace at 100 ℃ degrees for 45 min and cut into testing coupons.

Prepared nanocomposite films lost almost all their transparency at particle loading of 2–5 wt.%. Thus, both MTI-Instruments DTS-120-40 laser displacement sensor (Albany, NY, United States) and Fowler IP54 disk micrometer (Newton, MA, United States) measured each sample's final thicknesses. When the micrometer was used for nanocomposite films, thickness values were analytically corrected by considering the measured Young's moduli and the compressive force of 5 N.

4.2.2. Material Characterization

Prepared composite films were characterized for the three major properties of DE material according to the procedures described below.

4.2.2.1. Permittivity

Prepared Characterization was performed utilizing well-polished aluminum electrodes, with the precision LCR meter GW Instek LCR-6020 (Montclair, CA, United States) on 50 by 50 mm, 320 µm thick square coupons at 10 Hz. The relative dielectric permittivity values of the coupons were calculated from the experimental values of capacitance as an infinite parallel-plate capacitor, $C = \varepsilon_r \varepsilon_0 A/d$, where C is capacitance, A is electrode area, and d is the distance between electrodes (elastomer thickness). Electrodes and coupon sizes were chosen such that electrode area and composite film thickness provide $\sqrt{A}/d \approx 140$ to minimize field fringe effects (Carpi et al., 2015).

4.2.2.2. Elasticity

Rectangular coupons of 10 by 70 mm (with 60 mm gauge length) were cut from 320 µm thick films. A tensile test was performed using a universal test machine AMETEK CS225 (Berwyn, PA, United States) with a 1 kg load cell ANYLOAD 101AH-1kg (Fairfield, NJ, United States) at an extension rate of 60 mm/min (100% of strain per min).

4.2.2.3. Breakdown Strength

Using a custom setup, 100 µm thick composite films were tested. Films were placed on an aluminum plate that acted as a ground. A 2 mm diameter pin with rounded edges (positive electrode) was placed vertically and touched the top surface of the elastomer film with minimum penetration. The dielectric test was performed by the slow rate-of-rise method via a high-voltage amplifier TREK 20/20CH-S (Denver, CO, United States)

according to ASTM D149. For each new weight fraction of the composite, the voltage was applied in three steps: quickly increased to 50% of the anticipated breakdown strength, then gradually increased to 75% of the anticipated breakdown strength at a rate of 100 V/s, and then at a rate of 20 V/s until breakdown.

4.2.3. Prestretched DEA Testing

Biaxial electromechanical testing was performed on two prestretched, expanding-circle configuration DEAs made of plain silicone and optimum particulate composite. The thin films were manually pre-stretched by 22.5% of biaxial strain by matching pre-marked circles on the film with a rigid circular frame (Figure 4.3). This method provided purely equiaxial prestretch, which was controlled by the size of the marked circle. The amount of prestretch is sufficient to prevent loss of tension due to DEA's expected actuation while it can be easily achieved by manual stretching the film without damaging it. The silicone film was then fixed on the frame. Carbon grease was brushed through the circular mask on both sides of the film to serve as compliant electrodes. The electrodes were then connected to the copper tape electrodes on the rigid frame. The amplifier applied high voltage in the same fashion as in the breakdown strength test. Change in electrode area was monitored to track DEA actuation. Both material and DEA testing were conducted according to the DEA standards (Carpi et al., 2015).

4.3. Results and Discussion

The results of the primary parameters of interest in this study, i.e., material dielectric permittivity, Young's modulus, and breakdown strength, are presented and discussed in sub-sections 5.3.1, 5.3.2, and 5.3.3, respectively. For each particle type, mean experimental values are shown with their standard deviations (SD) and quadratically

interpolated as a function of the particle weight fraction. In sub-section 5.3.4, the data is

collected to analyze FOMs for DEA improved actuation performance. The same

parameters were interpolated for the optimum filler fractions. Results of the pre-stretched

DEA testing are presented and discussed in sub-section 5.3.5. Lastly, the nonlinear

behavior of composites is investigated to reveal the reason behind the difference in

theoretical and experimental FOM results.
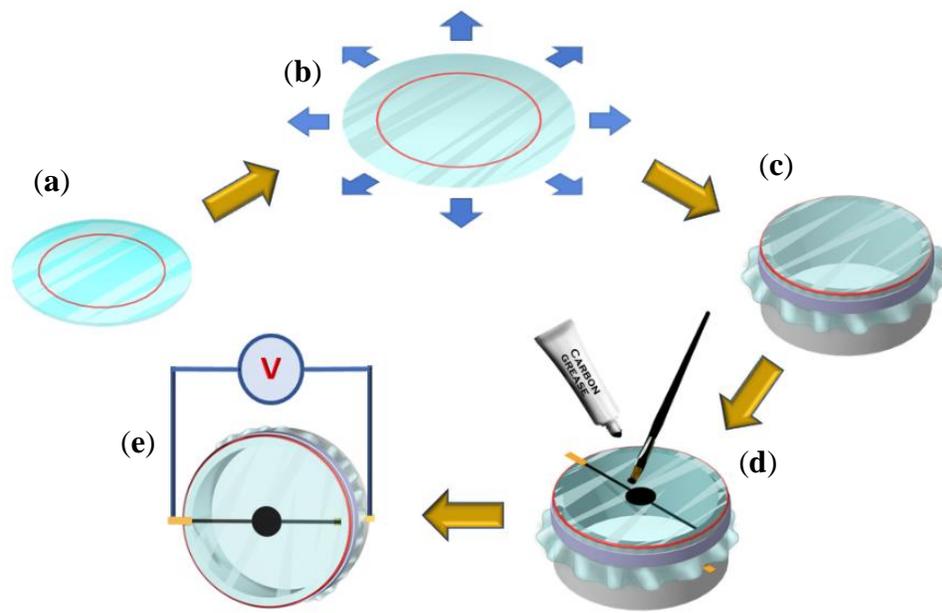
Figure 4.3 Preparation of the prestretched DEA for the expanding-circle configuration DEA electromechanical testing. (a) A circle (sized according to the desired pre-stretch) was marked on a silicone or dielectric composite film, (b) the film was manually pre-stretched until the pre-marked circle matched the circular frame, (c) pre-stretched film was fixed on the frame, (d) carbon grease electrodes were brushed on both sides of the pre-stretched film, (e) voltage was applied to electrodes while monitoring the actuation.

4.3.1. Permittivity

All prepared composites, especially those with CCTO particles, exhibited a near-

linear permittivity increase, typical for composites with relatively low filler loading

(Figure 4.4b).
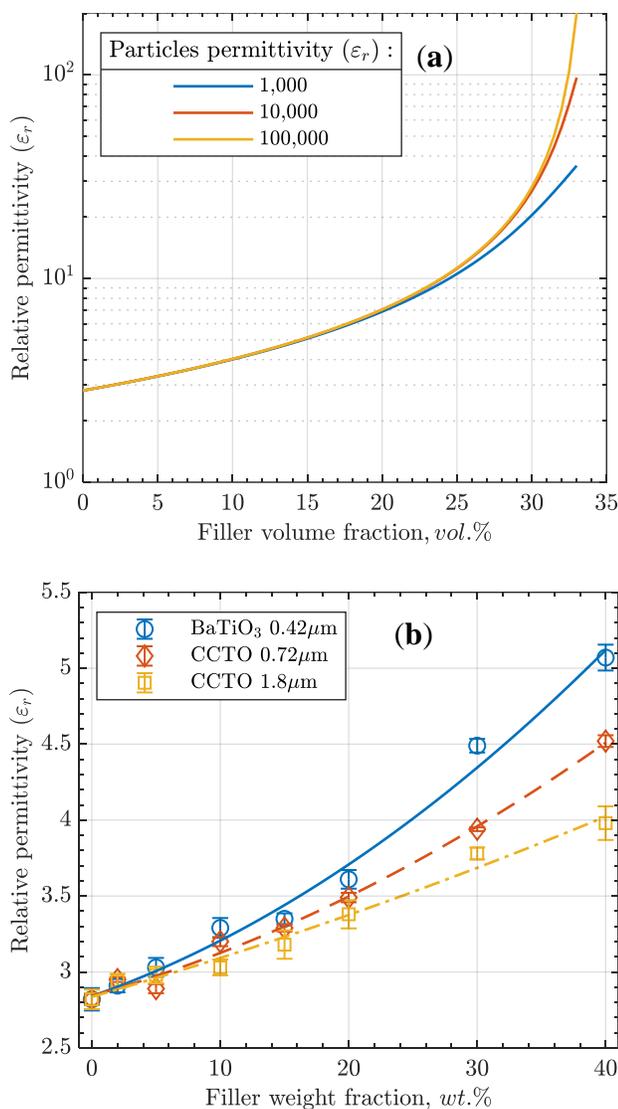
Figure 4.4 (a) Effect of particles' permittivity on the dielectric composite permittivity according to Bruggeman's model (Barber et al., 2009) (for matrix permittivity $\varepsilon_m = 2.8$). At lower volume filler loading, particles' permittivity has a minor effect on the final dielectric composite permittivity (40 wt.% of BaTiO$_3$ and CCTO equates to 10.8 and 12.8 vol.%, respectively). (b) Relative dielectric permittivity per weight fraction of BaTiO$_3$/PDMS and CCTO/PDMS composites. Tested on 50 by 50 mm, 320 µm thick coupons. Each data point represents mean value and SD of 8 coupons tested.

Following the general trend, the small CCTO particles provided higher dielectric

performance than the large particles. Although BaTiO$_3$ bulk material has lower

permittivity than bulk CCTO, their composites exhibited an inverse behavior. As high-

permittivity particles usually unveil their potential at much higher filler loadings based on

Bruggeman's model (Barber et al., 2009) (Figure 4.4a), particle size (specific surface area) can play a dominant role in the final composite properties at lower filler loadings. While $BaTiO_3$'s effect on permittivity in the experiment is congruent with the literature on PDMS/$BaTiO_3$ composites (Nawanil et al., 2019; Sappati & Bhadra, 2020), CCTO's effect is lower than in the known studies (Romasanta et al., 2012; Sindhu Vudayagiri et al., 2014; G. Wang et al., 2015). Mainly, Vudayagiri et al. (Sindhu Vudayagiri et al., 2014) investigated four different PDMS composites of similar permittivity mixed with CCTO. At 9 wt.% of CCTO (particle size was not reported), the improvement in permittivity was 18–48% relative to the plain silicone based on PDMS type. In the present work, the improvement of 13% is achieved for the same particle loading of small CCTO particles when mixed with Sylgard 184. The cause of this variance on the properties of composite can be multiple, including an interface region between the particles and matrix. Therefore, the effectiveness of a filler in composites depends on the interaction between filler and PDMS. This phenomenon and recent models based on it are thoroughly summarized by Barber et al. (Barber et al., 2009).

4.3.2. Elasticity

Figure 4.5 shows the effects of fillers on the composites' Young's moduli. All three curves display increasing trends as the amount of fillers increases, validating the elastomer's stiffness reinforcement. The gradual stiffening validates that none of the composites have reached their mechanical percolation, which is advantageous for DEA's operation. The upward concavity of the curves agrees with the generalized rule of mixture, often used to represent Young's modulus of particulate composites:

$$Y^n = Y_m^n v_m + Y_p^n v_p \tag{8}$$

where Y is composite Young's modulus, v is volume fraction, indices m, p stand for matrix and particles, respectively, n is coefficient varying from -1 to 1 (Hosford, 2009).
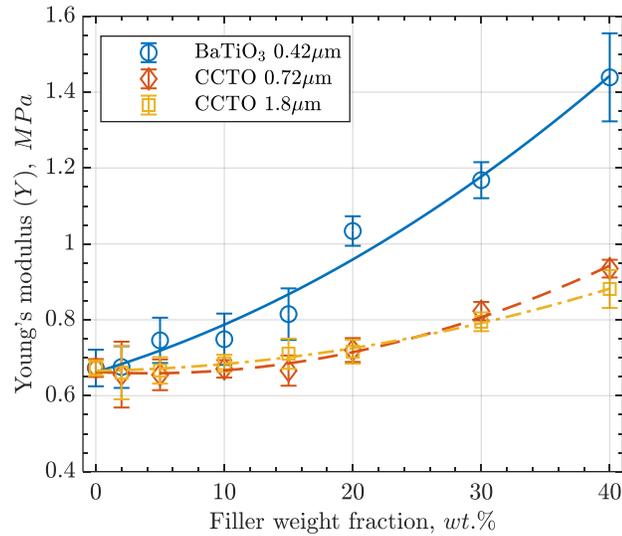
Figure 4.5 Young's modulus of BaTiO₃/PDMS and CCTO/PDMS dielectric composites, calculated from stress-strain curves (*Figure 4.6*). Tested on 10 mm by 70 mm, 320 µm thick coupons; each data point represents mean value and SD of 5 coupons tested.

When comparing composites with small and large CCTO fillers, a minor difference in stiffness was observed as the particle loading increased. This also agrees well with common practice as a number of studies concluded that particle size has no effect on the Young's modulus of microcomposites with filler size greater than 100 nm (Fu et al., 2008). Noteworthy, for both sizes of CCTO, changes in the Young's modulus are barely observed at weight fractions lower than 15 wt.%. Hence, utilization of low particle loadings of CCTO is possible without penalizing composite compliance. This behavior can be observed in several studies where CCTO showed minor stiffening effect at low particle loadings in PDMS (Sindhu Vudayagiri et al., 2014; G. Wang et al., 2015),

polyurethane matrices (Wan et al., 2017), and even a noticeable softening effect in an

epoxy matrix (Dandan Satia, Jaafar, & Julie, 2014).
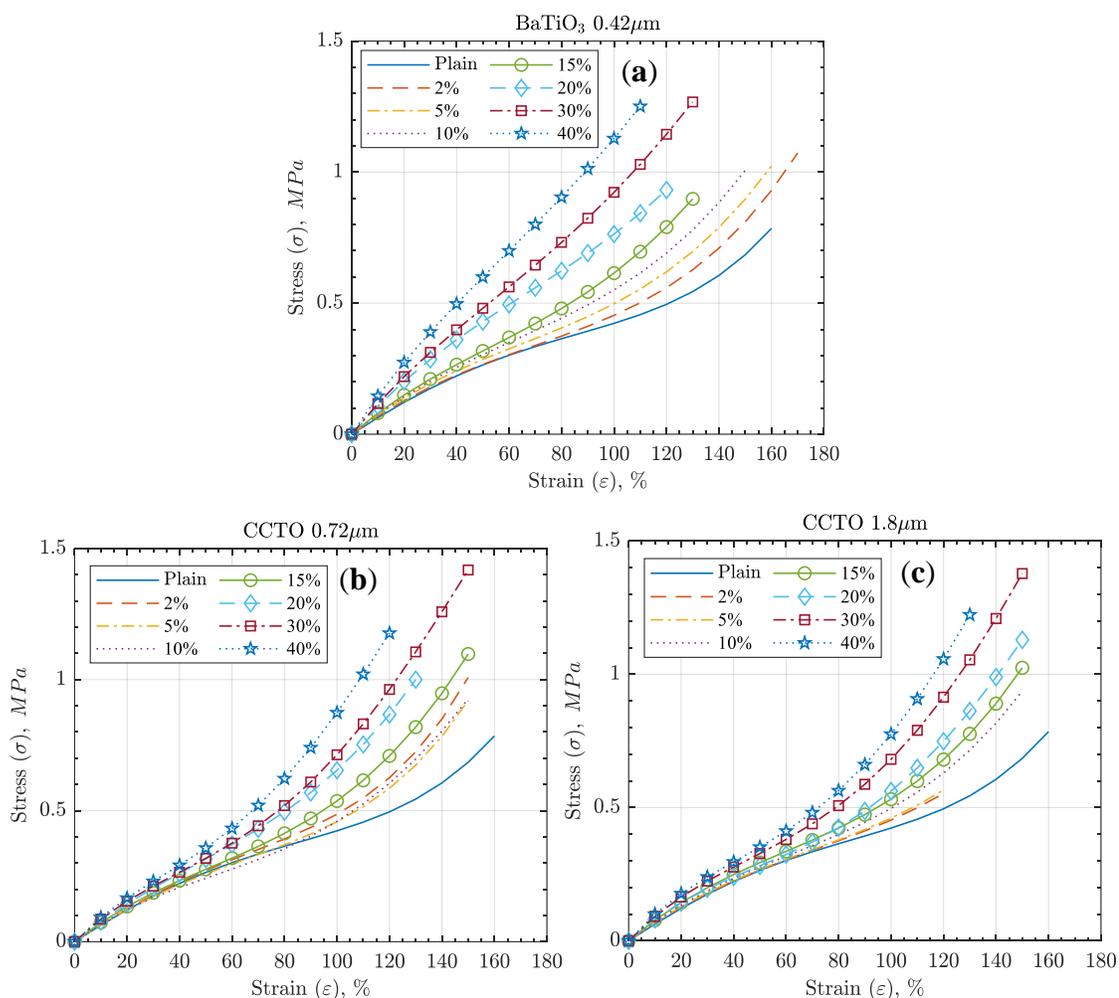
Figure 4.6 Stress-strain curves of the tested PDMS composites with: (a) BaTiO₃, (b) small CCTO, and (c) large CCTO.

Lastly, although bulk CCTO has a higher Young's modulus than bulk BaTiO₃ (Table

4.1), its composites showed a considerably lower stiffening effect than composites with

BaTiO₃. Besides particles' Young's modulus, composite's stiffness can be affected by an

incomplete bonding of particles across their interface area with matrix (H. Teng, 2010).

In a well-dispersed, degassed particulate composite, such debonding can be caused by

stretching a composite with an insufficient particle-matrix interfacial adhesion. Indeed,

preparation of thin tensile coupons usually involves peeling them from a substrate, which

applies some stretching to the samples. Additionally, insufficient adhesion can occur

when hydrophilic dielectric particles are dispersed in a hydrophobic matrix, e.g., PDMS.

4.3.3. Breakdown Strength

The loss of breakdown strength in dielectric composites occurs due to a locally

distorted and enhanced electric field and a path shortening effect of particles. Electric

field is predominantly affected by particles' agglomeration and size and, in the case of

DC breakdowns, the difference in filler's and matrix's electrical conductivities (Barber et

al., 2009).
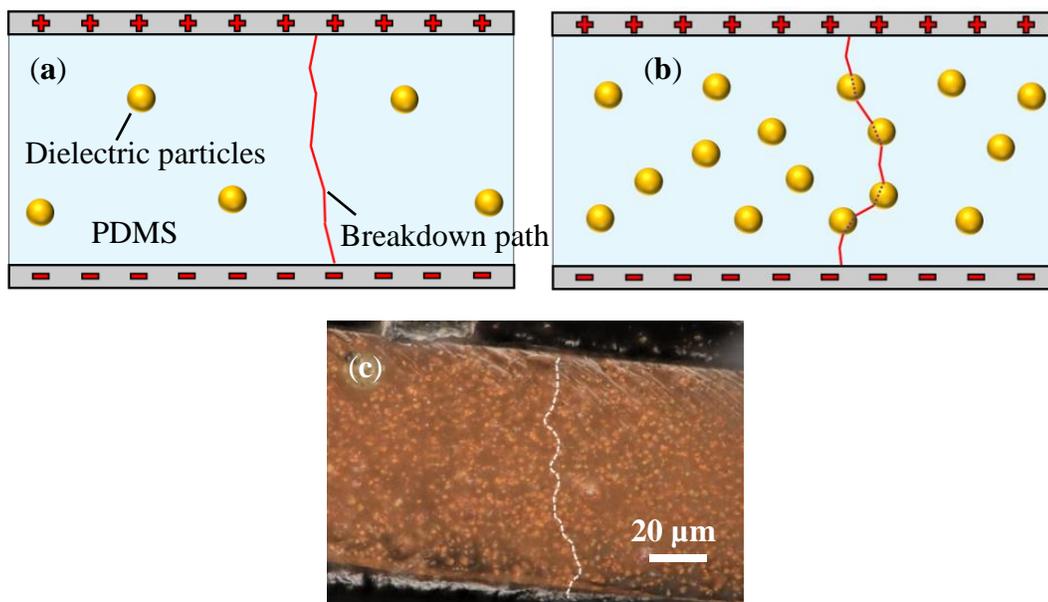
Figure 4.7 (a-b) Potential breakdown paths in dielectric composites illustrated based on the amount of filler particles and (c) estimated path from the actual CCTO/PDMS composite DEA, connecting closely placed particles (image taken with a digital microscope Keyence VHX-7000 Series (Itasca, IL, United States)). In (b), while dotted lines inside the particles do not represent an authentic path of breakdown, the nature of the breakdown strength loss can be illustrated.

When particles are added to the elastomer matrix to form a two-phase dielectric composite, the breakdown path can be shortened, resulting in a lower breakdown strength. Depending on the amount of particles in the composite, the breakdown path can go purely through the elastomer (Figure 4.7a) or involve particles in its path (Figure 4.7b). If particles are conductive or have lower breakdown strength than the matrix, the breakdown path goes through them, shortening the path through the highly insulating PDMS. Consequently, particles' amount, size, aspect ratio, alignment, and breakdown strength can influence the composite's breakdown strength (Cai et al., 2017; Molberg et al., 2010; Z. Wang et al., 2013; Yang, Hu, Chen, & Jinliang, 2016).

Figure 4.8 shows how dielectric strength decreased for all microcomposites with an increase in particle loading. Following the common trend, the composite with small CCTO particles maintained its breakdown strength better than that with large CCTO particles. Due to the small aspect ratio of CCTO particles, the morphology effect on the breakdown strength is neglected. Thus, the difference between the two CCTO-based composites' breakdown strengths is mainly due to the particle size difference.

$BaTiO_3$-based composites showed the highest breakdown strength for most of the particle loading range due to the smaller size, lower conductivity, and higher breakdown strength of the particles (Figure 4.8). Towards the highest filler loading, small CCTO particles showed comparable performance to $BaTiO_3$ particles. Interestingly, CCTO-based composites in the present work maintained breakdown strength noticeably better than those in the referenced study (Sindhu Vudayagiri et al., 2014). The absence of particle size and morphology in the original study restricts a comprehensive deduction of the reason behind this difference. However, some variations in the testing procedure,

specifically applied voltage increase rate and electrode shape, might have contributed to the result's difference.
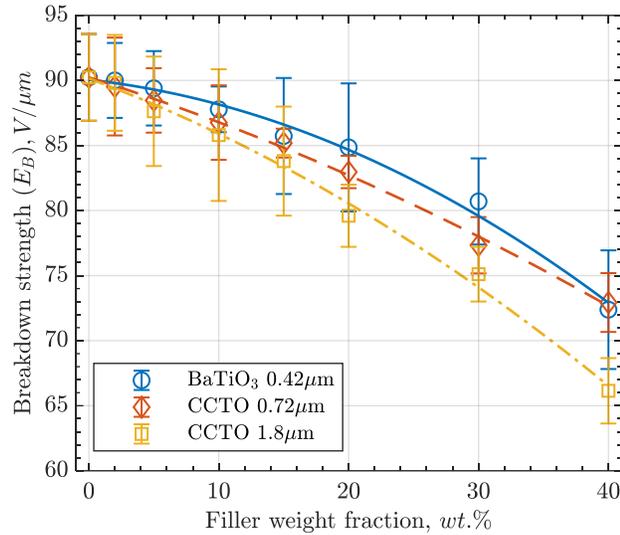
Figure 4.8 Breakdown strength of BaTiO₃/PDMS and CCTO/PDMS dielectric composites. Tested on 100 µm thick films. Each data point represents the mean value and SD of 10 measurements.

4.3.4. Figure of Merit (FOM)

Using the measured composites' properties, DEA FOMs were calculated and normalized with respect to Sylgard 184 (15:1 A to B part ratio). Figure 4.9a shows DEA FOM calculated according to Equation (7), which is based on maximum actuation strain. Figure 4.9b shows a FOM that evaluates actuation strain per unit voltage applied, calculated according to Equation (9):

$$FOM \ (strain \ per \ unit \ voltage) = \frac{\varepsilon_r \varepsilon_0}{Y} \tag{9}$$
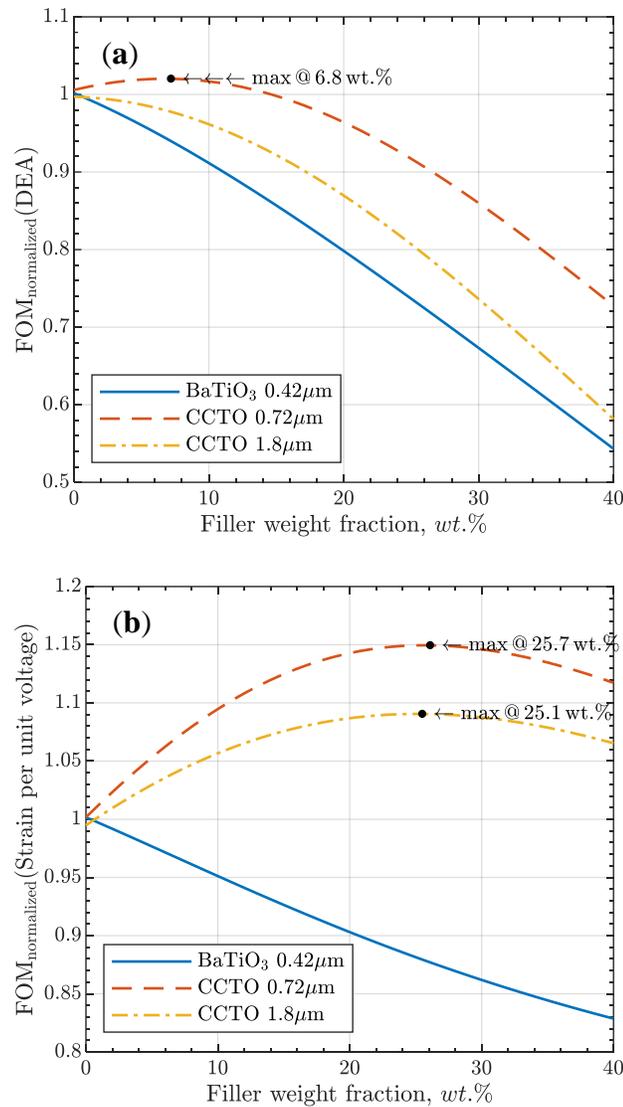
Figure 4.9 FOMs for (a) maximum actuation strain, and (b) actuation strain per unit voltage applied.

As Figure 4.9a shows, only a marginal improvement in maximum actuation strain can be achieved for a DEA with a small amount of selected CCTO particles. However, if a composite DEA with a lower breakdown strength has the same value of FOM (DEA) as the plain silicone DEA, i.e., achieves the same actuation deformation at maximum electric field, the actuation deformation of the composite DEA is achieved at lower voltage. As per Figure 4.9b, considerable improvement in DEA actuation efficiency

(strain per unit of applied voltage) can be achieved for both composites with CCTO

particles. For the determined optimum composites, the main properties are interpolated in

Table 4.3.

Table 4.2 Material characterization of prepared dielectric composites.

Material Composition	ε_r (−) @10Hz	Y (MPa)	E_B (V/µm)	FOM (DEA) normalized	FOM (Strain) normalized	Tensile Strength σ_{max} (MPa)	Maximum Strain δ_{max} (%)	Maximum Actuation Thickness ε_t (%) [a]
Sylgard 184 (15:1 mix ratio)	2.82	0.673	90.3	1	1	0.984	174	30.8
BaTiO₃ 0.42 µm — 2%	2.91	0.676	90.0	0.986	0.992	1.18	172	30.3
5%	3.03	0.746	89.4	0.961	0.977	1.04	156	29.6
10%	3.29	0.749	87.8	0.912	0.951	0.999	147	28
15%	3.35	0.815	85.7	0.857	0.926	1.06	139	26.3
20%	3.61	1.03	84.9	0.798	0.903	1.06	133	24.5
30%	4.49	1.17	80.7	0.673	0.862	1.32	134	20.7
40%	5.07	1.44	72.4	0.543	0.829	1.43	125	16.7
CCTO 0.72 µm — 2%	2.95	0.656	89.5	1.01	1.02	1.06	152	31.1
5%	2.89	0.655	88.5	1.02	1.05	1.06	154	31.3
10%	3.2	0.671	86.8	1.02	1.09	1.09	154	31.3
15%	3.29	0.666	85.2	0.998	1.12	1.16	149	30.7
20%	3.49	0.720	83.0	0.964	1.14	1.18	141	29.6
30%	3.94	0.823	77.3	0.86	1.15	1.58	140	26.4
40%	4.52	0.935	72.9	0.728	1.12	1.49	131	22.4
CCTO 1.8 µm — 2%	2.94	0.661	89.8	0.995	1.01	0.628	132	30.6
5%	2.98	0.667	87.6	0.987	1.03	0.676	133	30.3
10%	3.03	0.686	85.8	0.962	1.06	1.06	154	29.6
15%	3.18	0.711	83.8	0.922	1.08	1.04	147	28.3
20%	3.38	0.716	79.6	0.87	1.09	1.16	148	26.7
30%	3.78	0.795	75.1	0.736	1.09	1.31	143	22.6
40%	3.98	0.881	66.1	0.582	1.07	1.42	138	17.9

[a] Calculated assuming linear elasticity (Wissler & Mazza, 2005b).

4.3.5. Prestretched Composite DEA Testing

The composite with 25.7 wt.% of small CCTO particles was actuated and compared

to the plain silicone DEA to validate its higher actuation efficiency (Figure 4.10a–c).

Figure 4.11b shows that the actuation strain per unit of electric field (voltage in case of

equally thick films) is higher for the optimized CCTO composite, which validates that

FOM was improved. Experimental improvement varies from approximately 15% at lower

electric fields to the decreased performance of 8% towards the breakdown. Theoretical

improvement should be 15% according to calculated FOM (Table 4.3).

Table 4.3 Interpolated materials properties of dielectric composites with the optimum particle loading.

Material Composition	ε_r (−) @10H:	Y (MPa)	E_B (V/μm)	FOM (DEA) normalized	FOM $(Strain)$	Tensile Strength σ_{max} (MPa)	Maximum Strain δ_{max} (%)	Maximum Actuation Thickness Strain ε_t (%)
Sylgard 184 (15:1 mix ratio)	2.82	0.673	90.3	1	1	0.984	174	30.8
CCTO 0.72 μm 6.8 wt.%	3.02	0.666	88.0	1.015	1.07	1.07	154	31.4
CCTO 0.72 μm 25.7 wt.%	3.75	0.761	80.2	0.905	1.15	1.41	146	28
CCTO 1.8 μm 25.1 wt.%	3.53	0.756	77.5	0.802	1.09	1.23	145	24.8

This trend can be explained by the nonlinear elasticity of the materials, which is

intentionally neglected in FOMs calculations for uncomplicated material comparisons.

The tested composites' nonlinear material behavior can be conveniently presented in

terms of the tangent moduli (Figure 4.12). According to Figure 4.12b, at 45% of strain

(equivalent to 22.5% of biaxial film pre-stretch), actuation of DEA leads to softening of

plain silicone but stiffening of the optimized 25.7 wt.% small-CCTO composite (an

imaginary curve could be drawn between the 20 and 30 wt.% curves). This behavior of

the materials led to the difference between the predicted optimum FOM and the

experimental result.

Table 4.4 Experimental results of the biaxial electromechanical testing.

Material Composition	Thickness t (µm)	Applied E (V/µm) and (its % of the Material E_B)	Max Thickness Actuation Strain Reached ε_t (%)
Sylgard 184 (15:1 mix ratio)	78.6	80.2 (88.8%)	−17.3
CCTO 0.72 µm 25.7 $wt.\%$	89.6	66.3 (83.0%)	−13.5
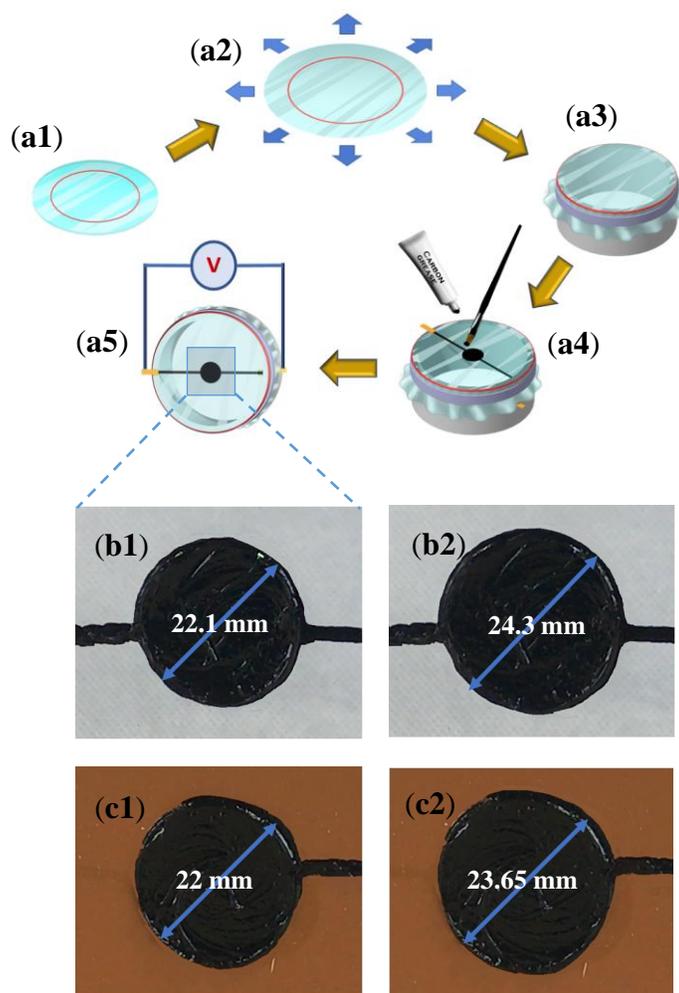
Figure 4.10 Prestretched DEA testing. (a1) A circle (sized according to the desired prestretch) was marked on a silicone or dielectric composite film, (a2) the film was manually prestretched until the pre-marked circle matched the circular frame, (a3) pre-stretched film was fixed on the frame, (a4) carbon grease electrodes were brushed on both sides of the prestretched film, (a5) voltage was applied to electrodes while monitoring the actuation. Plain silicone and optimized CCTO/PDMS dielectric composite DEAs (b1, c1) at 0 V and (b2, c2) at maximum voltage applied, respectively.
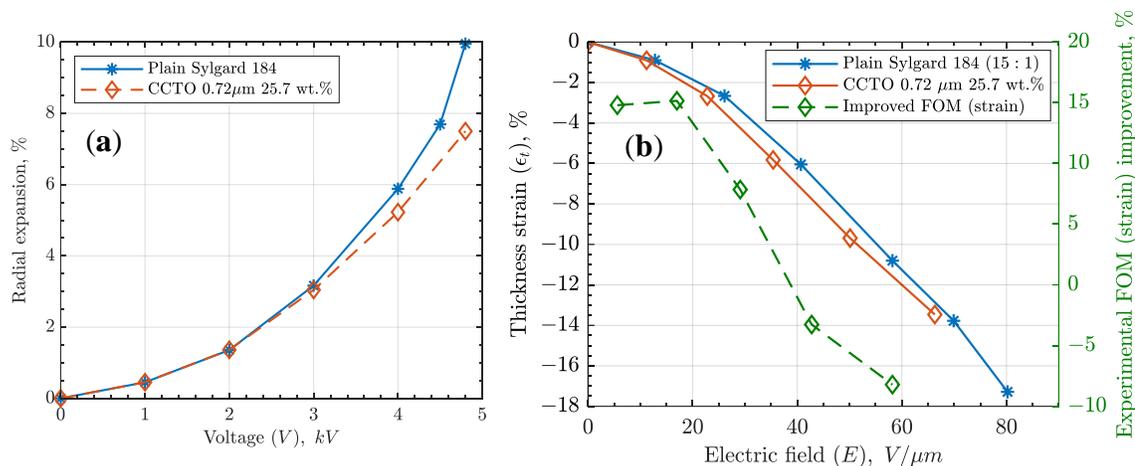
Figure 4.11 Prestretched DEA test results (a) as observed, (b) converted to representative parameters (thickness actuation vs electric field) of both DEAs and improved FOM (strain) of optimized CCTO/PDMS over plain PDMS. Thickness strain and electric field are calculated from the observed electrode radial expansion vs. applied voltage (Figure 4.11a), assuming incompressibility and linear elasticity of the silicone and composite (Wissler & Mazza, 2005b).

In addition, the tangent moduli allow for further analysis of the CCTO and BaTiO$_3$ stiffening effects. Similar to the Young's modulus, the CCTO particle size does not considerably affect stiffening at all strains. It is seen that as the particle loading increases, the tangent moduli vary in relatively smaller ranges, causing BaTiO$_3$ composites to behave more linearly. On the other hand, CCTO composites maintain their nonlinearity. While higher strain results in tangent moduli similar to that observed at lower values for BaTiO$_3$ composites, tangent moduli of CCTO composites are relatively higher at high strains compared to initial values (Young's moduli). However, the higher stiffness of CCTO composites towards its stretchability limit can hardly be considered a significant drawback, as DEAs typically operate at strains far from the maximum elongation of the elastomer material. In fact, this behavior contributes towards the DEA's electromechanical stability. Therefore, the tangent modulus can be used not only for

correcting performance prediction using conventional FOMs, but also for choosing the optimum degree of pre-stretch so that DEA operates in its lowest stiffness range.
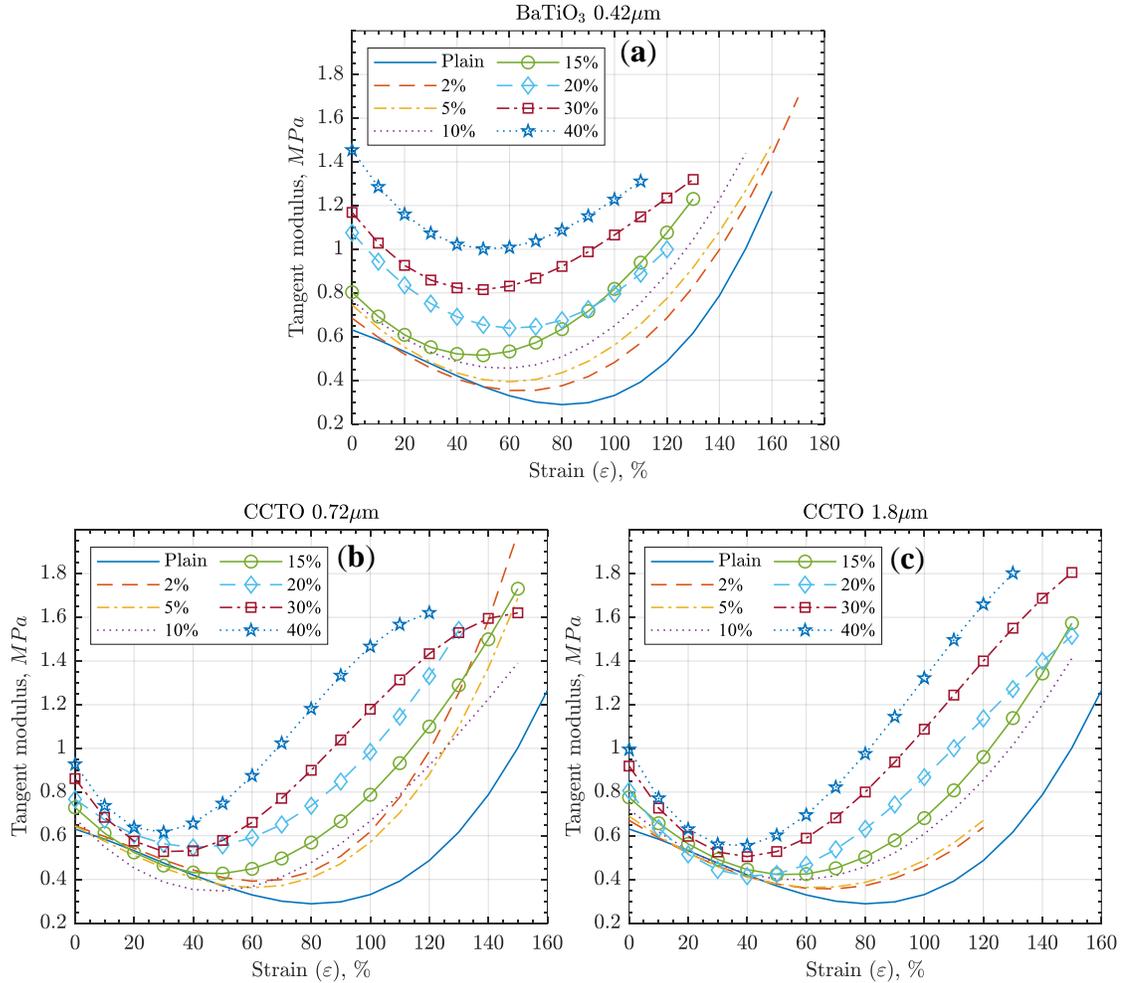
Figure 4.12 Tangent moduli as functions of strain of dielectric composites with different particle loadings of (a) BaTiO₃, (b) small CCTO, and (c) large CCTO particles.

4.4. 3D Printed Composite DEA

As demonstrated in the previous subsection, the experimental performance improvement of composite DEAs matches the analytically predicted FOM (strain) at lower electric fields. Therefore, loading DE material with dielectric particles is a more

appropriate approach to enhance actuation performance for 3D printed than for conventionally fabricated DEAs due to the absence of the prestretch.

To investigate printability of the composite DEA through contact dispensing, an attempt was undertaken to 3D print a single-layer unimorph DEA with the composite DEA consisting of Sylgard 184 (mixed in 15:1 ratio) with the optimum 25.7 wt.% filler loading of 0.72 µm CCTO particles using the nScrypt 3Dn Series printer with the 125 µm printing tip. A typical convention to enable printing with particulate composite materials for the utilized apparatus is to keep filler size at least an order of magnitude smaller than the printing tip diameter. While this relation is satisfied with a great margin for the selected 125 µm printing tip and 0.72 µm average effective diameter CCTO filler (even considering the largest particles of 2.5 µm), the printed composite DE layer did not possess sufficiently uniform thickness for effective DEA operation. The thickness non-uniformity was attributed to the variable viscous properties of the composite material due to the micro scale size of particles and certain agglomeration. Hence, application of smaller size particles and implementing more sophisticated particle dispersing methods are seen as the major future work on 3D printed composite DEAs.

Meanwhile, a single-layer unimorph composite DEA with the decreased CCTO filler loading (the optimum 6.8 wt.% according to the FOM(DEA)) was successfully fabricated and tested (Figure 4.13). As before, different initial curvatures greatly complicate direct comparison of the maximum actuation deformation for the printed DEAs with composite and plain silicone DE layers. Nevertheless, the composite DEA showed an even higher achieved electric field of 34.6% of the composite breakdown strength with the actuation

deformation comparable to the plain silicone DEAs. The higher achieved electric field

was attributed to thicker DE layer contributing towards DE film thickness uniformity.
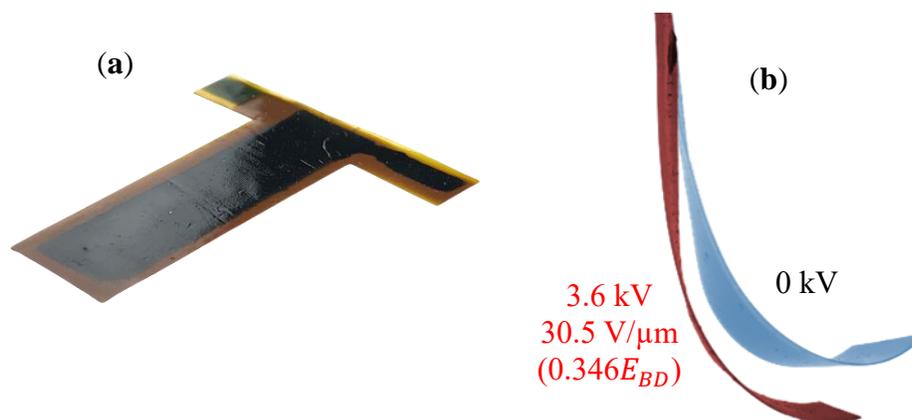
Figure 4.13 Single-layer unimorph DEA with the composite DE layer (6.8 wt.% of 0.72 µm CCTO particles) (a) as printed with nScrypt 3Dn Series contact dispensing printer and 125 µm printing tip, and (b) in actuation testing (cantilevered vertically).
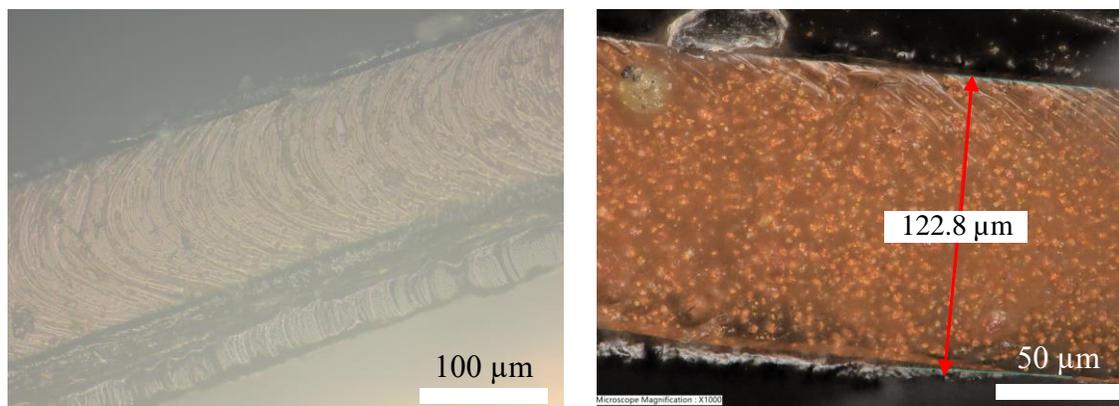
Figure 4.14 Cross-section of the single-layer unimorph DEA with the composite DE layer (6.8 wt.% of 0.72 µm CCTO particles) showing (a) uniform thickness across the actuator (image taken with a digital microscope Olympus) and (b) particle distribution inside the printed composite DE layer (image taken with a digital microscope Keyence VHX-7000 Series (Itasca, IL, United States)).

4.5. Summary of Composite DEA

This chapter studied the effects of particle loading and size on CCTO/PDMS

dielectric composites for DEA applications and compared them to conventionally used

BaTiO$_3$ particles. Relative dielectric permittivity, Young's modulus, and breakdown strength were experimentally determined to characterize the tested composites. Compared to other studies on CCTO/PDMS composites, current results with Sylgard 184 showed lower permittivity values but higher breakdown strength, emphasizing the importance of the compatibility of matrix and particles. The CCTO composites' Young's moduli started increasing at about 15 wt.% of filler loading and, overall, showed lower stiffening effects than BaTiO$_3$. It allowed CCTO-based DEA to achieve significantly better performance, as shown by FOMs, even though the BaTiO$_3$/PDMS composite had higher permittivity and breakdown strength. It was shown that for CCTO, even moderately smaller particles achieved considerably greater performance in permittivity and breakdown strength, while having minor effects on Young's modulus.

FOMs were used to determine the optimum filler loading for dielectric composites with CCTO and BaTiO$_3$ particles. While no optimum filler loading was found for BaTiO$_3$, both types of CCTO composites maximized their performance at filler loadings. Particularly, in this study, the optimum filler loading for CCTO was found to be 25.1–25.7 wt.% depending on the particle size. Electromechanical testing of the DEA made of the optimized composite with small CCTO particles solidified the improved material performance, while highlighting differences between theoretical FOM and actual DEA performance. Composites' elasticity was further studied through tangent moduli, which revealed the reasons behind the differences in theoretical FOM and results of electromechanical testing.

Finally, optimized composites were utilized to additively fabricate unimorph DEAs and validate material printability. Overall, dielectric composites are seen as an effective and promising method to boost 3D printed DEAs performance due to:

- Improved electromechanical properties, particularly at lower strains (demonstrated through FOMs, electromechanical testing, and composites' tangent moduli).

- Lower actuation voltage even if the FOM (DEA) is not improved due to decreased breakdown strength of the composite.

5. Compliant Electrode for DEA

This chapter is split into two sections. The first section presents the characterization of the conductive polymer-based (PEDOT:PSS) electrode replicated from a study on the stretchable electrode, for which a considerable softening was achieved through adding a small-molecule surfactant plasticizer (Triton X-100) (Sikulskyi et al., 2020). Furthermore, the characterized electrode material was utilized for printing the unimorph actuator through microdispensing in Chapter 4. The second section of the present chapter is dedicated to further improvement of electro-mechanical properties of the electrode material, particularly compliance and its printability.

5.1. First Electrode Composition for Validating Printing Methodology

As described in the literature review, some works of blending PEDOT:PSS with small-molecule plasticizers or polymers already resulted in materials with Young's modulus of the same order of magnitude as of common materials for soft actuators (10^0 MPa) (Oh et al., 2016; C. Teng, Lu, Zhu, Wan, & Jiang, 2013). Therefore, considering the additive manufacturability of the material and its simple mixing and handling, a PEDOT:PSS electrode softened with a small-molecule surfactant plasticizer Triton X-100 is chosen as an initial candidate for compliant actuator's electrode material (Oh et al., 2016). In the original study, the primary conductive material was mixed with the plasticizer in different weight fractions. An optimal mixture with a weight fraction of 70 wt.% of Triton X-100 was chosen based on its highest conductivity and comprehensively studied. Meantime, a mixture with 80 wt.% of Triton showed to have lower Young's modulus (~0.9 MPa) without a significant drop in conductivity. Thus, this dissertation aims to analyze the PEDOT:PSS-Triton X-100 electrode with 80 wt.% of the plasticizer,

focusing on the main properties of interest for soft actuator application. This includes mechanical (stretchability and stiffness), electrical (conductivity and its dependence on deformation and temperature), and thermal (resistive heating). Then, fully printed DEAs with PEDOT:PSS-Triton X-100 electrodes are manufactured through the microdispensing technique and tested as a unimorph actuator (Chapter 4).

5.1.1. Experimental Setup

This subsection describes materials, mixing procedures, and material characterization methods used for the first electrode composition (replicated electrode) for checking its printability and ensuring electro-mechanical properties.

5.1.1.1. Materials

- PEDOT:PSS (MilliporeSigma, Burlington, MA, United States), surfactant-free, high-conductivity aqueous 1.1 wt.% solution of PEDOT:PSS served as a primary electrode material.

- Triton X-100 (MilliporeSigma, Burlington, MA, United States), surfactant plasticizer ($C_{14}H_{22}O(C_2H_4O)_n$), where (n=9-10), was used to improve electrode's mechanical and electrical characteristics.

- Sylgard 184 (Dow Inc., Midland, MI, United States, part #4019862), used as a DEA dielectric material for a unimorph bending actuator and supporting PDMS material for the electrodes in conductivity and thermal tests (measured properties can be found in Chapter 4).

- Kapton (Kaptontape Interstate Group Inc., Torrance, CA, United States), 1 mil (25.4 µm) Kapton tape was used as a substrate for a unimorph bending actuator.

5.1.1.2. Material Mixing and Test Coupons Preparation

Electrode material was prepared by mixing PEDOT:PSS 1.1 wt.% aqueous solution with Triton X-100 in 22.7:1 ratio to achieve 80 wt.% of the surfactant plasticizer in the cured electrode. Mixing was performed utilizing a planetary mixer, THINKY ARM-310 (Laguna Hills, CA, United States), at 2000 rpm for 5 min. Two different methods were used to prepare testing coupons; molding on top of PDMS film and microdispensing on top of pre-printed and cured PDMS film. In order to increase the electrical conductivity of PEDOT:PSS, curing and consequent annealing of electrodes (to increase the electrical conductivity) was performed on heating beds at 70 °C for 2 h for both methods (Oh et al., 2016). Finally, films were cut into 70 mm by 10 mm coupons with an approximated mean thickness of 50 µm. The thickness of each coupon was measured using a scanning electron microscope (SEM) (Figure 5.1). PDMS-supported electrodes were used for conductivity and thermal tests, while free-standing (unsupported) electrodes were used for the mechanical characterization.
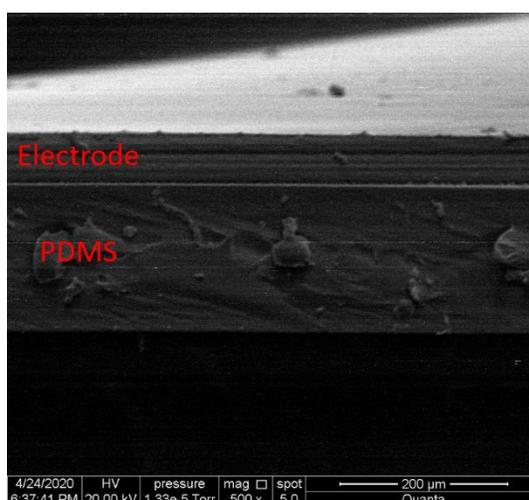
Figure 5.1 SEM figure of a testing coupon consisted of a PEDOT:PSS - Triton X-100 electrode on top of PDMS supporting film.

Two-component silicone Sylgard 184 was used to fabricate PDMS film mixed in a 15 (base) to 1 (curing agent) ratio by weight. For molded electrode coupons, PDMS film was applied on PET film using applicator Zehntner ZUA2000. PDMS film served as supporting material for electrodes in conductivity and thermal testing. In addition, PDMS film allowed smooth peeling of the electrode film without dealing damage and to perform mechanical testing with a free-standing electrode.

5.1.1.3. Electrode Material Characterization

When the DEA undergoes deformation, the electrodes are subjected to a considerably large tension when the DEA is operated in a pre-stretched configuration. Therefore, the effects of deformation on the properties of electrodes must be evaluated.

- *Conductivity.* The four-point probe method was used to find the electrical conductivity of the electrode material. Custom-built setup applied specific amounts of elongation to the PDMS-supported electrode samples while applying a current through the outer probes (power supply Keysight U8001A) and measuring the voltage through the inner probes (digital multimeter Greenlee DM-810A).

- *Mechanical test.* A tensile test was performed using AMETEK CS225 with a 1 kg load cell on a free-standing electrode coupon at an extension rate of 30 mm/min (50% of strain per min).

- *Thermal test.* Resistive heating of the PDMS-supported electrode samples was studied utilizing thermal camera FLIR E95-24-NIST. During the heating process, changes in electrical conductivity were monitored using the four-point probe method.

5.1.2. Results and Discussion

Electrode characterization starts with the mechanical testing of the free-standing electrode samples to investigate the material's stretchability and stiffness. The stress-strain curve (Figure 5.2a) shows the maximum deformation of the free-standing electrode, almost reaching 35%. None of the tested coupons reached strain of the initial study on the electrode (~55%), which is partially due to thinner coupons used (50 µm versus 0.5 mm in the initial study) and higher thickness variation. The corresponding tangent modulus is plotted against strain in Figure 5.2b showing a considerable softening effect during the deformation. Tangent modulus at zero strain represents Young's modulus and shows almost an order of magnitude higher value than in the original study (Oh et al., 2016). Such a value of Young's modulus is especially high compared with dielectric elastomers commonly used for DEAs. Thus, PEDOT:PSS-based electrode needs to be softened even more to be used more effectively for the DEA application.
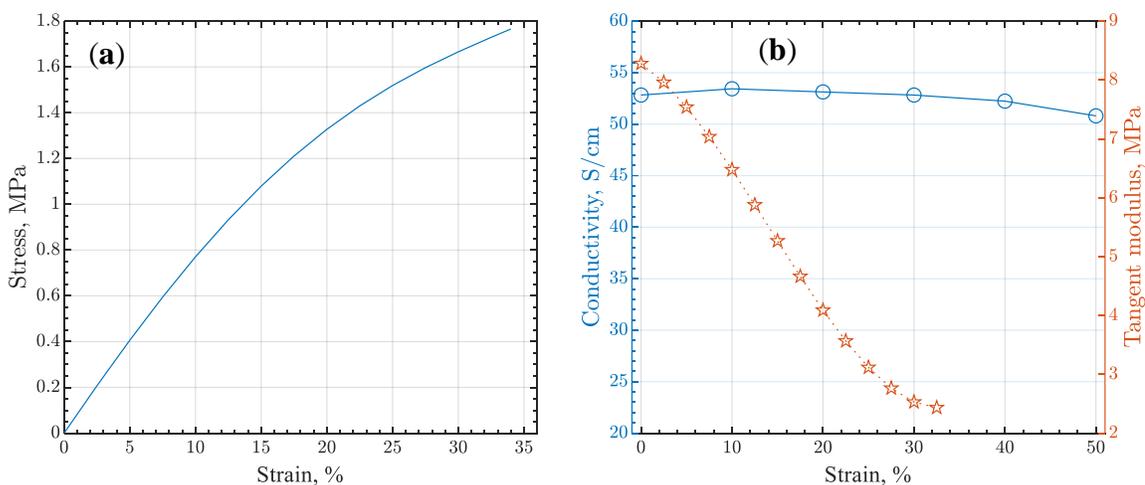
Figure 5.2 Electrode's (a) stress-strain curve and (b) conductivity and tangent modulus as a function of tensile strain.

While the free-standing electrodes broke before 35% of strain, PDMS-supported electrodes used in conductivity testing stretched up to 55%. Thus, when embedded with elastomers to form soft actuators, PEDOT:PSS - Triton X-100 electrodes can withstand larger deformations. Figure 5.2b shows how electrode material maintains relatively steady conductivity throughout the entire deformation. Particularly at $\varepsilon = 50\%$ (which is about 90% of maximum material strain), the electrode's conductivity is about 0.96 of the initial conductivity in an undeformed state. Repeatedly tested samples showed minimum to non-change in conductivity. Interestingly, a slight increase in conductivity was noticed at low strains (5-15%) for all samples tested, which was not the case for the material composition with 70 wt.% of the plasticizer in the original study on PEDOT:PSS – Triton X-100 electrode (Oh et al., 2016).
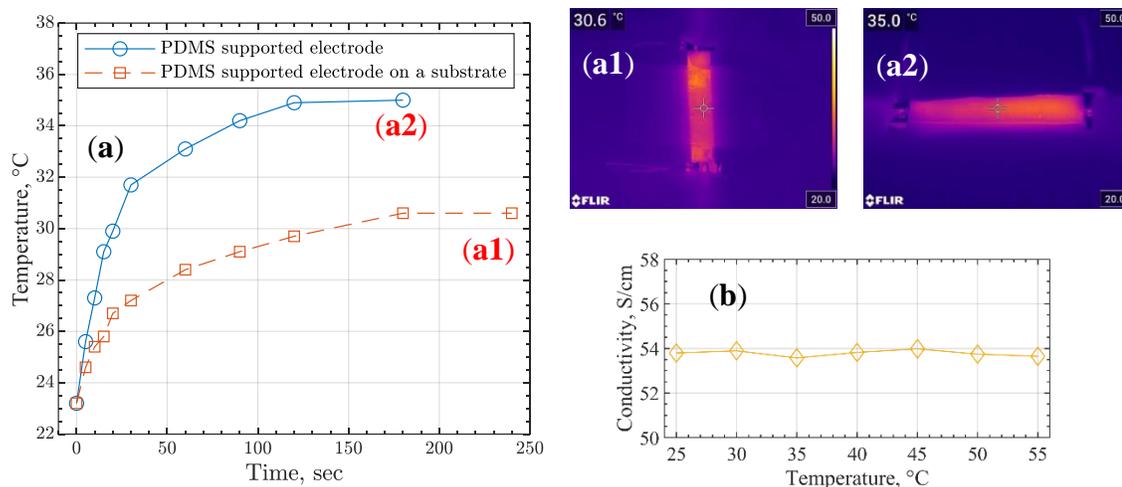
Figure 5.3 Electrode's (a) resistive heating (@ current I=0.1 Amp) and thermal images at steady-states (a1) and (a2), (b) conductivity as function of temperature.

Thermal testing of the PDMS supported electrode was performed for two cases of resistive heating. The sample was hung on the tips allowing a more effective natural convection air cooling in the first case. The second case simulated an actuator attached to

the surface by adding a substrate as a heat sink to the PDMS supported electrode. The results of the test are shown in Figure 5.3a. The graph demonstrates clear trends of temperature change and approximate steady-state points for both considered cases. Figure 5.3(a1) and Figure 5.3(a2) demonstrate temperature distribution in electrodes at steady-states for the sample with and without a heat sink, respectively. Figure 5.3(a1) shows uniform heat distribution across the sample, validating uniform conductivity in the sample. The variation in temperature seen in Figure 5.3(a2) is due to a slightly smaller thickness measured at the right edge of the tested sample. When electrodes are used for the DEA, the current does not continuously flow through the electrodes. However, the heating of DEA elastomer and electrode layers still occurs due to the materials' electrical and mechanical losses. Thus, the effect of temperature on conductivity was studied within the range of typical operational temperatures. The results show great stability of the electrode's conductivity (Figure 5.3b).

Lastly, a self-clearing effect of the electrode was observed during testing of 3D printed unimorph actuators when the DE thickness was decreased to less than 50 µm resulting in breakdown happening at lower voltages (Figure 5.4). After experiencing multiple minor breakdowns, actuators with a thin DE layer still demonstrated actuation with a degraded performance due to the burnt (inactive) electrode area.
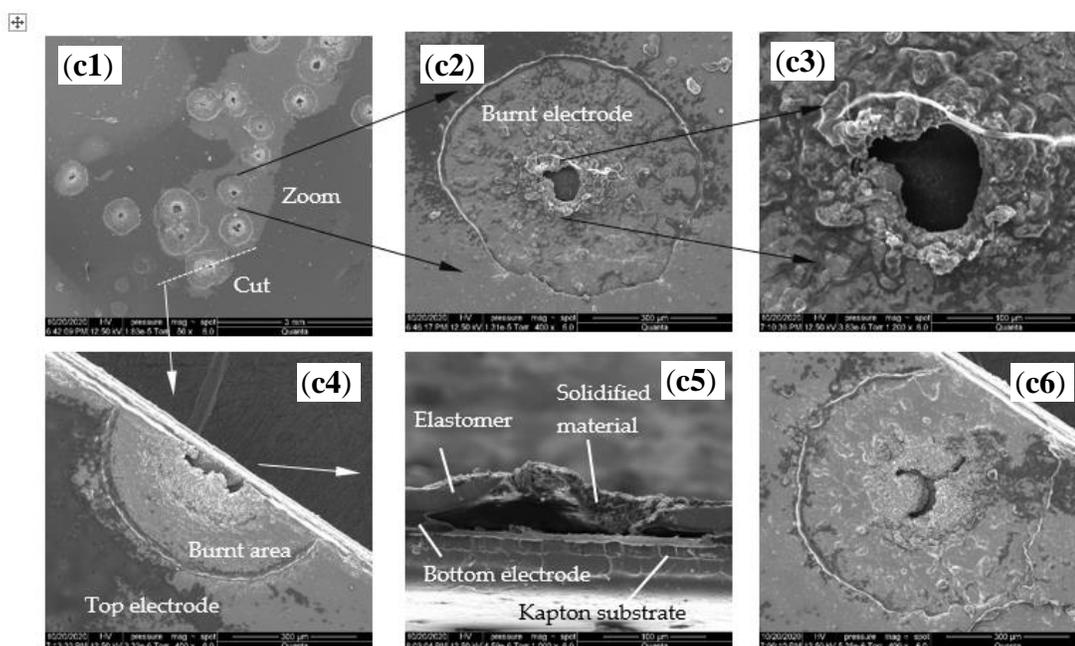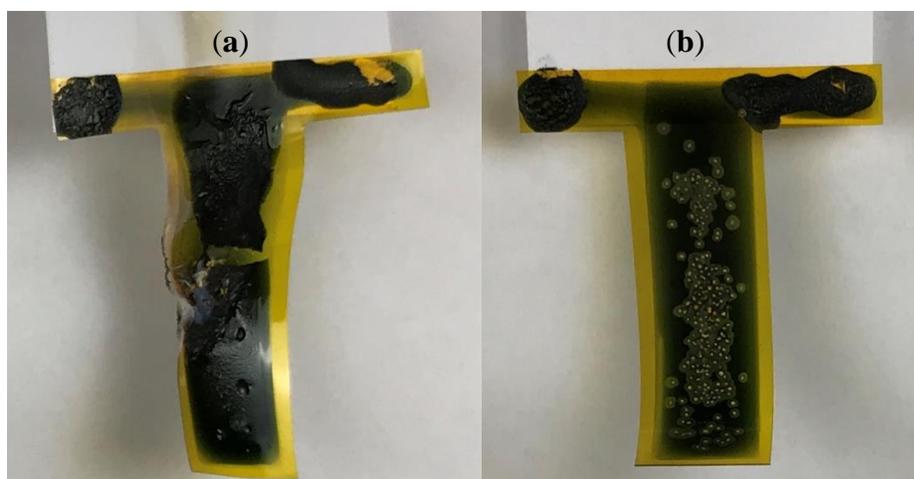
Figure 5.4 Tested 3D printed unimorph DEAs with the elastomer layer thickness of (a) 80-90 µm, showing a single major breakdown, and (b) less than 50 µm showing numerous minor breakdowns (c1-c6) examined with SEM.

5.1.3. Summary of the First Electrode Composition

Based on the performed material characterization, the electrode is stretchable enough

for most soft actuators with moderate deformation (<50%). Particularly for DEA, a tested

electrode application for DEAs without prestretch is possible. Compared to the original

study, electrode material matched the conductivity and stretchability values (when

supported by a PDMS layer). However, it showed almost an order of magnitude greater

Young's modulus than reported. Therefore, further investigation and effort to soften the

material was required. Nonetheless, printing with a low-concentrated solution of

conductive material allows to easily achieve low electrode thickness, which partially

mitigates its stiffening effect. As a result, the unimorph actuator testing showed a

considerable bending capability even though the actuator was not optimized for a

maximum deformation. Furthermore, the electrode material possesses sufficient

printability forming an even layer on top of the elastomer.

5.2. Second Electrode Composition for Improved DEA Actuation

The absence of a clear and quantitative correlation between major electrode

properties and DEA actuation performance restricts the comprehensive optimization of

electrode material for DEA application. However, the studied effect of electrode

properties on short-term actuator performance can be presented in Table *5.1*.

Table 5.1 Correlation between DEA parameters and electrode properties.

Electrode properties	DEA parameter
Material modulus ↑, thickness ↓	Stiffness↑
Conductivity ↑, thickness ↓	Voltage across the DE layer (due to a better charge distribution) ↑

The stiffening effect of the electrode is apparent and can be estimated with various

models for multilayer unimorph actuators with unevenly thick layers. Regarding

conductivity, current and past studies typically state that electrodes are required to be

"highly conductive". Recent studies have shown that higher conductivity and lower

thickness of the electrodes positively affect charge distribution, and consequently voltage,

across the DE layer (J. Zhang et al., 2020). Thus, the need for a comprehensive,

quantitative performance estimation tool, i.e., FOM, for DEA electrodes is evident and is among the main objectives of future work. Meanwhile, electrodes prepared from the aqueous solution of PEDOT:PSS can be very thin, positively contributing to both stiffness and voltage across the DE layers. Appropriate conductivity values can be controlled in terms of the sheet resistance compared to the existing well-performing but relatively low-conductivity carbon grease electrodes. Mainly, commercial carbon grease electrodes with a maximum conductivity of 0.02 S/cm (Chemicals, 2015) are typically 100-500 µm thick, providing 1000-5000 Ω/sq sheet resistance. As will be shown, the sheet resistance of all the prepared electrode material compositions in the following sections is lower than the reference. Thus, stiffness is seen as the main disadvantage of the first electrode composition used in the present study, making material modulus and minimum printable thickness the main parameters for electrode improvement.

To further improve electrode performance, several techniques can be used. Additional softening is possible by controllably increasing the amount of plasticizer. As previously shown, further increase in Triton X-100 concentration inevitably leads to reduced conductivity (Oh et al., 2016). To mitigate the effect of decreasing conductivity at high plasticizer concentrations, doping by EG or dimethylsulfoxide (DMSO) can be utilized to reduce the ionic bond between PEDOT and PSS (Yoon & Khang, 2016). Furthermore, while DMSO typically has a stiffening effect on conductive polymers (Guo, Glavas, & Albertsson, 2013; Savagatrup et al., 2014) (but not always (Dauzon et al., 2019; P. Li et al., 2015)), EG showed various effects (P. Li et al., 2015; Luo et al., 2019). Thus, investigating the effect of potential further softening of EG on PEDOT:PSS-Triton X-100 electrodes is of great interest. Lastly, hydrogel formation is another approach to achieve

compliance in conductive electrodes due to the material structure change. The common concerns regarding material stability, manufacturability, and handling properties will be closely monitored.

5.2.1. Validating Proper Materials for Further Analysis

Serving as base materials for all the methods to improve electrode performance in this work, PEDOT:PSS and Triton X-100 were carefully selected. Several factors were considered when selecting the materials for the second electrode composition.

Firstly, a lower PEDOT to PSS component ratio (5:8) was checked as the conductive component for compliant electrodes with 80 wt.% Triton X-100. Coupons, prepared similarly to the first electrode composition study, showed unchanged elasticity while the conductivity decreased from 53 S/cm to about 20 S/cm. This result agrees with the literature in both elasticity and conductivity properties. While a higher ratio of conductive PEDOT to insulative PSS should lead to a less conductive electrode, both components of the conductive material (PEDOT and PSS) have comparable stiffness close to the one of PEDOT:PSS (Lipomi et al., 2012). Thus, different ratios of PEDOT to PSS should not affect the elasticity of the electrode. Hence, PEDOT:PSS with the higher ratio was kept for further experimental investigation.

Secondly, Triton X molecular weight affects electrical conductivity and, most notably, its solubility in PEDOT:PSS can be found in the literature (S. Kim et al., 2017). Triton X-100 and X-114 (with 9.5 and 7.5 repeatable units, respectively) showed the best solubility with no phase separation at 90 wt.% of the plasticizer in PEDOT:PSS. While the molecular weight of Triton X showed a considerable effect on the conductivity of electrodes at lower concentrations (0-40 wt.%), the effect was shown to be much less

considerable at concentrations above 60 wt.%. Despite the absence of mechanical

properties investigation in the study, Triton X-100 and X-114 assumably have a

comparable effect on electrode elasticity due to their close number of repeatable units

(molecular weight). Lastly, to the author's knowledge, higher concentrations of the

plasticizer are not described within the literature and would be another new contribution

of the present work.

5.2.2. Experimental Setup

This subsection presents material and methods utilized for the second electrode

composition with a focus on new implementations.

5.2.2.1. Materials

Same 1.1 wt.% high-conductivity, surfactant-free aqueous solution of PEDOT:PSS

and surfactant small-molecule plasticizer Triton X-100 as in the sub-section 6.1.1.1. were

used. Additional materials for the second electrode composition included:

- Dimethyl Sulfoxide (Fisher Scientific, Waltham, MA, United States, BP231-100),

  a > 99.7 % pure DMSO was used to dope PEDOT:PSS-Triton X-100 electrodes

  and to prepare the first hydrogel composition.

- Ethylene glycol (MilliporeSigma, Burlington, MA, United States), a 99.8 % pure

  EG was used to dope PEDOT:PSS-Triton X-100 electrodes.

- Methanol (Duda Diesel, Decatur, AL, United States), a 99.65 % pure methanol

  was used in preparation of the second hydrogel composition.

5.2.2.2. Material Mixing, Films Preparation, and Heat Treatment

Two mixing techniques with different timings were applied to ensure proper

distribution of PEDOT:PSS and Triton X-100 phases (materials were taken out of

refrigeration and passively warmed up to room temperature before mixing). To quantify effects of mixing on electrode material, elasticity and conductivity at strains were investigated for coupon mixed through different procedures to judge the sufficient mixing. The mixing processes included mixing with a magnetic stirrer or a planetary mixer THINKY ARM-310 (Laguna Hills, CA, United States). The stirring process consisted of 2.5h at 300 rpm (also referred to as "stirred" in present research), while three different processes were tested with the planetary mixer. The first process consisted of mixing at 5 min at 2000 rpm (also referred to as "fast-mixed" in present research). The second process consisted of 5 min at 1200 rpm, 2 min at 2000 rpm, and again 5 min at 1200 rpm (also referred to as "5+2+5" in present research). Finally, the third process consisted of 20 min at 2000 rpm (also referred to as "well-mixed" in present research). All the combinations of mixed materials were molded into 50x50 mm PDMS molds to prepare films. Then, the molds were placed on a hot plate and cured according to the procedures described below.

Similarly to mixing effects on final electrode properties, the effects of different curing cycles were studied. Four heat treatment (curing and annealing) processes on a hot plate were applied as follows. Firstly, curing was performed at 60°C until all the water from the PEDOT:PSS aqueous solution evaporated. Then annealing process was executed in four ways: no annealing after curing, 3h at 60°C and 90°C, and 2h at 70°C. Once the annealing was finished, the films were cut with a laboratory scalpel into the testing coupons. The final thickness of the coupons varied in a range of 50-150 µm, with an average width of 5 mm and length of 45 mm.

5.2.2.3. Electrode Material Characterization

- *Conductivity.* The four-point probe method was used to find the electrical conductivity of the electrode material. An in-house built setup applied specific amounts of elongation to the PDMS-supported electrode samples while applying a current through the outer probes (power supply Keysight U8001A) and measuring the voltage through the inner probes (digital multimeter Greenlee DM-810A). Additionally, a four-point probe Ossila (Sheffield, UK) was used as a precise commercial apparatus to validate the conductivity at zero strain measured through the in-house built setup.

- *Mechanical test.* A tensile test was performed using a universal test machine AMETEK CS225 (Berwyn, PA, United States) with a 10 kg load cell ANYLOAD 101AH-10kg (Fairfield, NJ, United States) on a free-standing electrode coupon at different extension rates based on coupon length but equal to 50% of strain per min. All the tests were performed in the same lab environment with a room temperature of 21.6±0.5°C and relative humidity of 50±2% to ensure repeatable results for PEDOT:PSS-based electrodes. Young's modulus of each mixed electrode composition was measured as a slope on the stress-strain curve between 0 and 1% of strain.

5.2.3. Results and Discussion

The initial experimental testing aimed to find the most suitable mixing and heat treatment process for PEDOT:PSS-Triton X-100 electrodes. As such, it was found that for all analyzed mixing processes, the latter did not have a considerable effect on electrode conductivity. In contrast, the mixing process has a considerable effect on the

materials' elasticity. The common trend showed that longer, more intensive mixing provided a greater softening effect. Particularly, the sample stirred for 2.5h achieved the highest stiffness with Young's modulus of Y=8.6 MPa (Figure 5.5a) and largely limited the stretchability. Close stiffness was achieved by samples mixed in the planetary mixer for 5 min at 2000 rpm (fast-mixed), while for 20 min mixing at the same speed (well-mixed) stiffness was decreased to 5.53 MPa. However, the 20 min of intensive mixing resulted in small particles of solidified PEDOT:PSS due to the viscous heating, sometimes clogging the printing tip (Figure 5.6). A filtration process, e.g., by means of 0.45 µm PTFE filter (Du et al., 2018; Pasha, Roy, Murugendrappa, Al-Hartomy, & Khasim, 2016), is typical for removing solidified particles from the PEDOT:PSS aqueous solutions. However, in the present procedure, solidified particles are created during the mixing process after adding plasticizer Triton X-100. By filtering the modified material, it was observed that the process is complicated by adding the plasticizer and using filters with larger cell sizes. Furthermore, the PEDOT:PSS to Triton X-100 ratio can be uncontrollably altered by the filtration process if a considerable amount of PEDOT:PSS solidifies and is filtered from the electrode material.

To avoid the need for filtration of the prepared material while benefitting from the reduced Young's modulus of the adequately mixed electrode material, the approach to optimize the mixing process was undertaken. It was observed that a slower speed of the planetary mixer can provide similar results with a sufficient amount of mixing time. Thus, a combined "5+2+5" cycle was tested, showing very close Young's modulus to the well-mixed samples while not resulting in considerable solidified pieces clogging the printing tip and reducing the mixing time almost by half. Interestingly, while stirred

matching in Young's modulus, "5+2+5" demonstrated higher stiffness at strains greater than 10% and slightly smaller stretchability (Figure 5.5b). Lastly, no improvements in material mechanical properties were observed for more prolonged mixing.
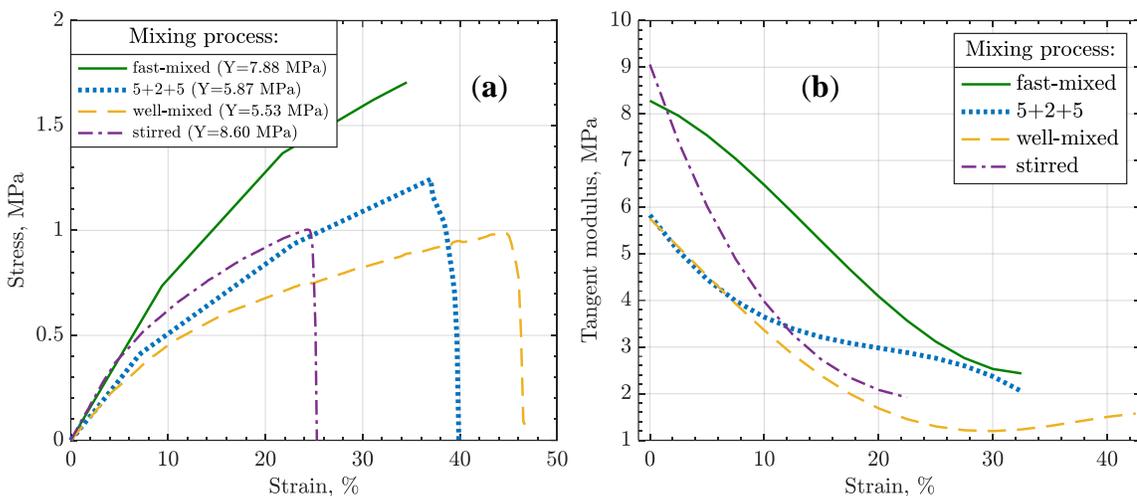
Figure 5.5 Effect of mixing on (a) stress-strain curves and (b) tangent moduli of differently mixed PEDOT:PSS-Triton X-100 (80 wt.%) electrodes.
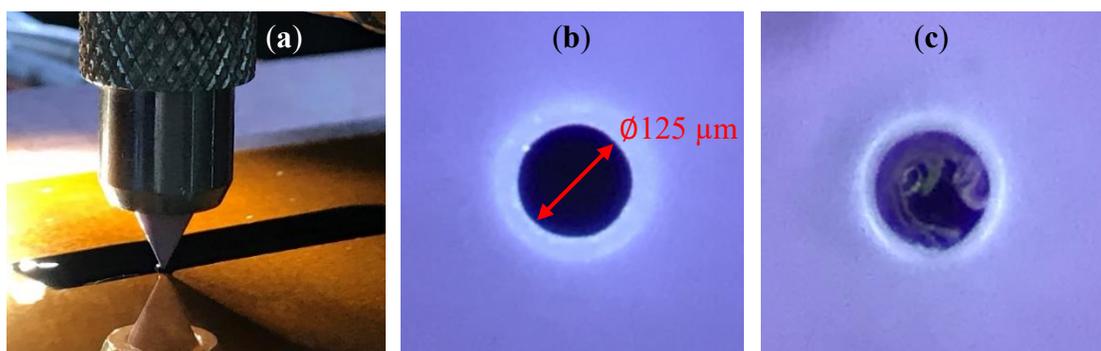
Figure 5.6 nScrypt ceramic printing tip with 125 µm channel (a) during printing and observed using an optical microscope when (b) clean and (c) clogged.

The second tested parameter of material preparation was the heat treatment. In contrast to the mixing process, the difference in heat treatment insignificantly altered mechanical properties of the electrodes with almost unchanged Young's modulus (Figure

5.7a). Meanwhile, the heat treatment process has a major impact on the electrode's conductivity. It was observed that conductivity increases for heat treating the sample up to 3h at temperature up to 85-90°C., while additional treatment did not provide noticeable improvement. For DEA printing, heat treating of electrodes layer inevitably subjects elastomer materials to increased temperature. Depending on elastomer material, long exposure to increased temperatures can degrade the material. Thus, heat treatment processes with lower temperatures were tested to investigate their effectiveness in terms of conductivity increase (Figure 5.7b). As shown in the figure, heat treating the electrode for 2h at 70°C provides a much greater effect than 3h heat treating at 60°C. Therefore, temperatures around 70-80°C can be utilized to achieve most of the heat treatment effect on PEDOT:PSS-Triton X-100 electrode while the heat treatment timing can be improved.
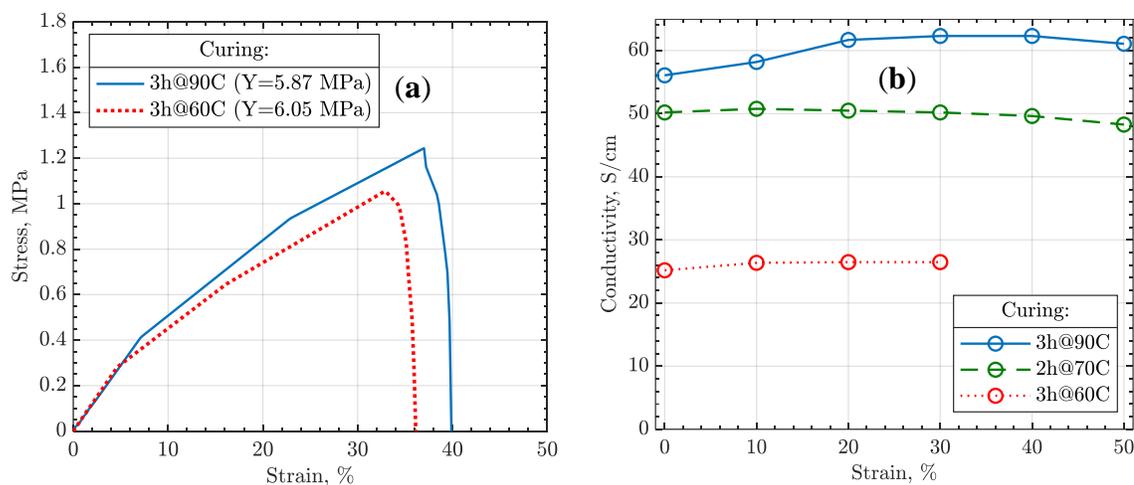
Figure 5.7 Effect of curing on (a) stress-strain (the least and most stretched samples out of tested for 3h@90°C heat treatment are shown) and (b) conductivity-strain curves of PEDOT:PSS-Triton X-100 (80 wt.%) electrodes.

5.2.3.1. Improved Electrode Through Increased Concentration of Plasticizer

Based on the performed analysis, all following samples modified with different approaches (further softening with Triton X-100, doping with DMSO and EG, and forming hydrogels) were mixed according to the "5+2+5" process and heat treated for 3h at 90°C. The "5+2+5" mixing process was chosen to expedite the mixing process of all the material compositions and batches. At the same time, longer heat treatment was applied to multiple molds on the hot plate to achieve the highest electrical performance. The coupons prepared through the first approach to further soften electrode material by increasing the concentration of Triton X-100 are shown in Figure 5.8 and characterized in Figure 5.9 and Figure 5.10.

(a)   **(b)**   **(c)**   **(d)**
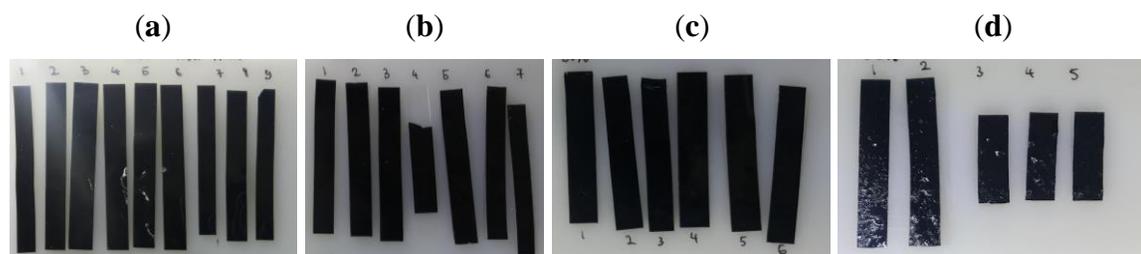
Figure 5.8 Prepared PEDOT:PSS-based electrode samples with increased concentrations of plasticizer Triton X-100: (a) 80 wt.%, (b) 85 wt.%, (c) 90 wt.%, (d) 95 wt.%.

Material characterization has shown that as additional Triton X-100 was mixed into the electrodes, the electrode's stiffness was effectively decreased. Particularly at Triton X-100 concentrations of 90 wt.% and above, a noticeable change in mechanical response is noticed. The most eye-catchy difference is almost the ideal linear response of the materials. In addition, there is a smaller softening effect and stretchability when the concentration of Triton X-100 is increased from 90 to 95 wt.%. The softening effect and decreased stretchability can be explained by exceeding the limit of solubility of Triton X-

100 in PEDOT:PSS. Indeed, the phase separation in the material with 95 wt.% of the plasticizer could be noticed through a simple visual inspection in the form of free-standing Triton X-100 on the prepared films/testing coupons. Although the 90 wt.% material films did not show visible phase separation, the linear response suggests that complete saturation of PEDOT:PSS with Triton X-100 could take place. Nonetheless, thanks to the obtained linearity, stiffness of 90 wt.% Triton X-100 electrodes at low strains was greatly lowered below the Young's modulus of the most utilized PDMS in this study, Sylgard 184, with the modulus of Y=1.2 MPa when mixed in the standard ratio (10:1 Part A to Part B) (Figure 5.10a).
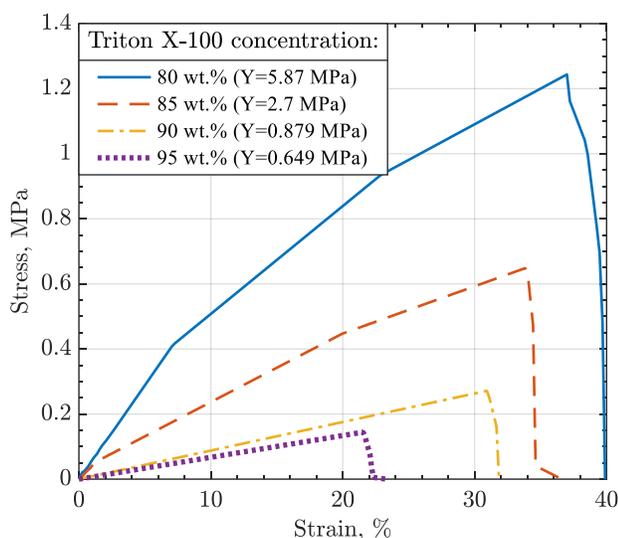
Figure 5.9 Stress-strain curves of PEDOT:PSS-Triton X-100 with various concentrations of the plasticizer.

Regarding the conductivity, Figure 5.10b illustrates a more gradual decrease in conductivity with increased concentration of the plasticizer. Thus, a more predictable variation of conductivity provides some flexibility in optimizing the amount of the plasticizer between 85 wt.% and 90 wt.%. Sufficient stretchability of 30% for non-

prestretched 3D printed DEAs, Young's modulus about 1 MPa, and conductivity above 20 S/cm would allow such an electrode to stand out against other compliant electrodes within the literature. Lastly, the viscoelastic and fatigue characteristics of the electrodes need to be investigated.
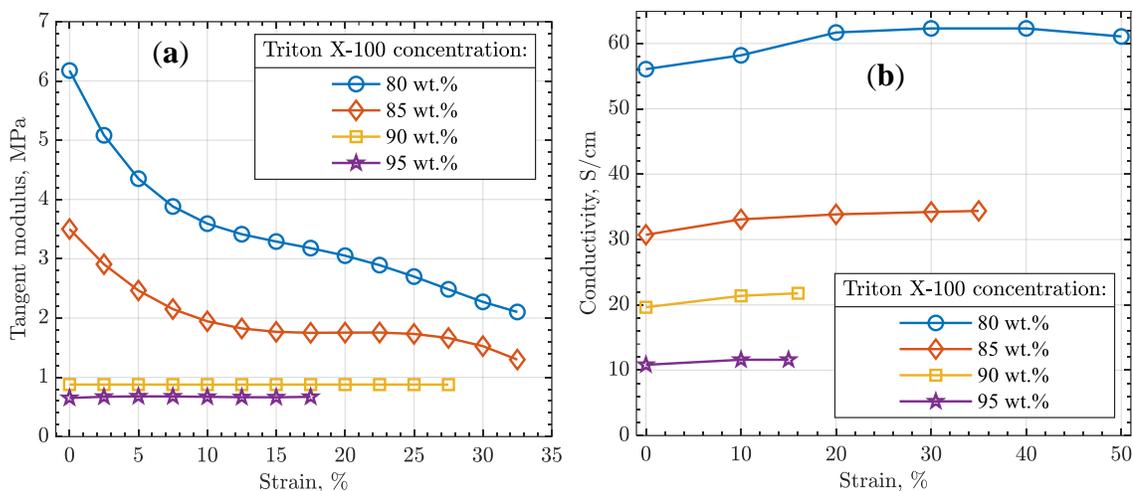
Figure 5.10 (a) Tangent moduli and (b) conductivity-strain curves of PEDOT:PSS electrodes with various concentration of Triton X-100. The tangent moduli were obtained from the stress-strain curves (*Figure 5.9*).

5.2.3.2. Improved Electrode Through Doping with DMSO and EG

Doping the first formulation of electrode consisting of 80 wt.% Triton X-100 and 20 wt.% PEDOT:PSS in a cured state was the second approach to boost electromechanical performance. Considering that DMSO evaporates from the mixed composition, it was added directly to the premixed PEDOT:PSS-Triton X-100 electrode and mixed in the planetary mixer for an additional 5 min at 1200 rpm before molding. When cured at 90°C, material experience great shrinkage with the increased content of DMSO (Figure 5.11a). To reduce the shrinkage, the material was first cured at 60°C for 2h to evaporate

most of DMSO at a slower rate and then cured for 90°C for 3h as for the rest of the electrodes to boost the conductivity (Figure 5.11b).

Meanwhile, EG does not evaporate and thus alters the ratio of electrode components. To maintain the same amount of conductive polymer for comparable results, the amount of EG added to the mixture substituted Triton X-100, i.e., two prepared material compositions with EG had components ratio of PEDOT:PSS to Triton X-100 to EG as 20:79:1 and 20:75:5, respectively. When preparing electrodes doped with EG, all components were added and mixed all at once. The appearance and behavior of the coupons doped with EG during curing was similar to the undoped electrode.
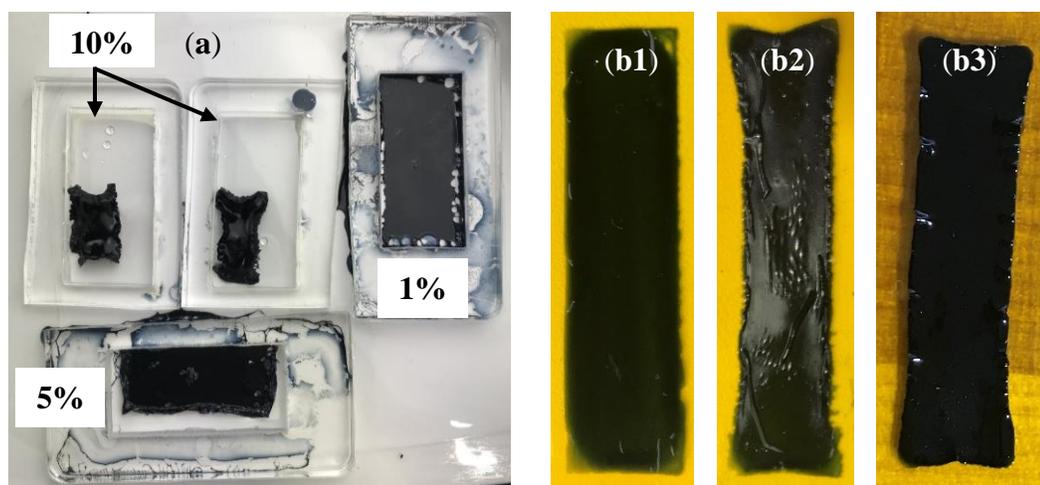
Figure 5.11 PEDOT:PSS – Triton X-100 (20-80 wt.%) electrode material: (a) doped with various amounts (wt.%) of DMSO, molded, and cured for 3h at 90°C; printed on PDMS (b1) without DMSO doping and cured for 3h at 90°C, (b2) doped with 5 wt.% DMSO and cured for 3h at 90°C, and (b3) doped with 5 wt.% DMSO and cured for 2h at 60°C and then for 3h at 90°C.

DMSO doping had a substantial effect on both the mechanical and electrical properties of the electrode. Firstly, a great stiffening effect is evident from stress-strain curves (Figure 5.12). Moreover, for electrodes doped with DMSO, a certain region at 0-

5% of strain characterized by particularly increased stiffness can be noticed. While 1%

doped material increased its stretchability, 5% doped material decreased its stretchability

below 30% of strain. Simultaneously, the conductivity of the material was effectively

boosted, as shown in Table *2.1*. However, the relative increase in conductivity is smaller

compared to the relatively increased Young's modulus. Additionally, obtaining a film

with acceptable quality testing coupons was much harder for material doped with DMSO.
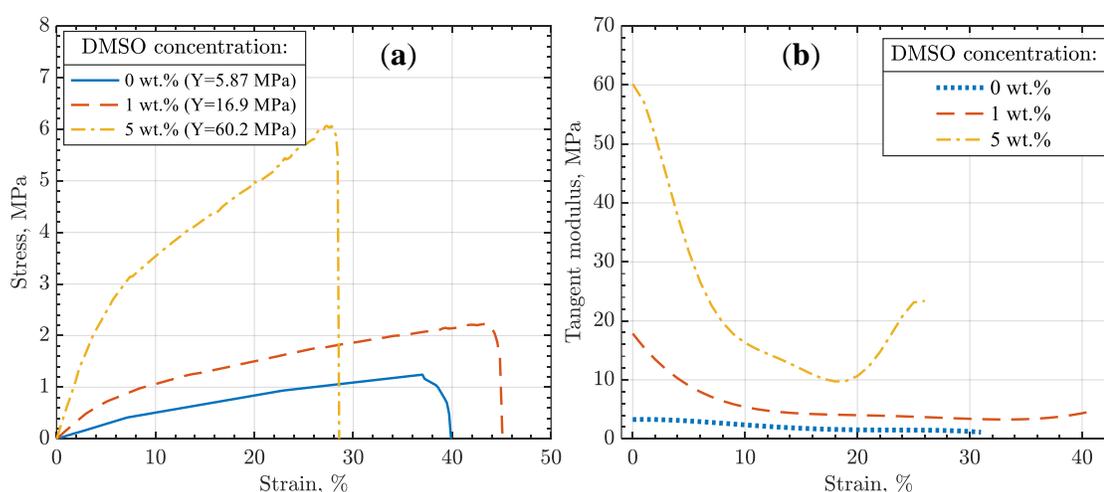
Figure 5.12 (a) Stress-strain curves and (b) tangent moduli of PEDOT:PSS-Triton X-100 (80 wt.%) doped with DMSO.

Table 5.2 Young's modulus and conductivity of PEDOT:PSS-Triton electrode doped with DMSO vs the benchmark PEDOT:PSS-Triton X-100 (80 wt.%) electrode.

Triton X-100 DMSO	Young's modulus, MPa	Conductivity, S/cm
0 wt.%	5.87	56.1
1 wt.%	16.9	80.3
5 wt.%	60.2	180.5

Doping with the second material, EG, resulted in much smoother coupons with a

high-quality appearance. Nevertheless, both mechanical and electrical testing showed

substantial deviation in results across testing coupons. Overall, EG doped materials

showed degraded electromechanical performance with reduced stretchability,

conductivity, and slightly increased stiffness, particularly at lower strain. While an

increase in stiffness was expected due to the reduced concentration of Triton X-100 being

a better plasticizing material, a decrease in conductivity was untrivial as PEDOT:PSS-

Triton X-100 electrode has the highest conductivity at about 70 wt.% of the plasticizer.

This suggests that EG interfered Triton X-100 in dissolving PEDOT:PSS.
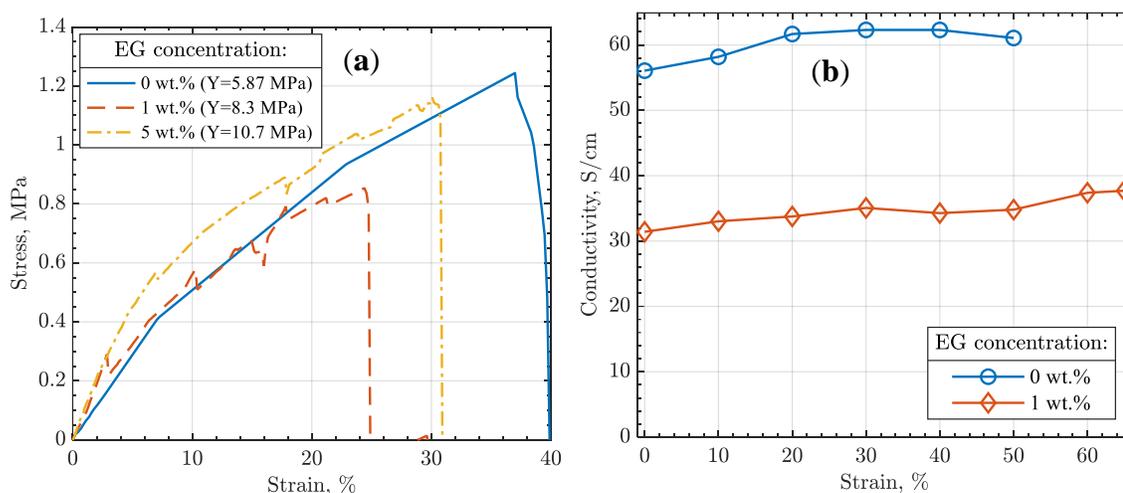
Figure 5.13 (a) Stress-strain and (b) conductivity-strain curves of PEDOT:PSS electrodes with various concentration of Ethylene glycol (EG).

5.2.3.3. Improved Electrode Through Forming Hydrogels

Hydrogel formation was the last approach utilized in this dissertation to achieve

compliant conductive materials suitable for 3D printed DEAs. Firstly, DMSO was added

to the 1.1 wt.% aqueous solution of PEDOT:PSS and stirred for 8h. This hydrogel recipe

(including further curing cycles and rehydration) was already described in the literature

and demonstrated superior conductivity and Young's modulus within the same order of

magnitude with PDMS. Then, in an attempt to further soften the hydrogel, Triton X-100

was added in a 4:1 ratio to PEDOT:PSS to obtain 80 wt.% Triton X-100 in the final cured

hydrogel and mixed in the planetary mixer with the "5+2+5" process. The material was

cast into silicone molds and cured as in the reference study, 24 h at 60ºC and then three

cycles of 30 min at 130ºC with 30 min breaks in-between. The cured hydrogel experience

even more considerable shrinkage than DMSO doped electrodes, but the film possessed

uniform thickness across most of the sample. When the testing coupons were cut from

films, some of them were rehydrated by submerging into DI water for different amounts

of time ranging from 30 sec to 10 min (Figure 5.14). The rehydration time did not alter

the properties of the hydrogel.

Figure 5.14 Hydrogel material (a) after curing, (b) cut to the coupon and swelled.

Figure 5.15 shows the mechanical response of both non-hydrated (unswelled) and

hydrated (swelled) hydrogel electrodes. Conductivities at zero strain are stated in Table

5.3 and compared along with Young's moduli with the benchmark 80 wt. % Triton X-100

electrode. The unswelled electrode demonstrates characteristics close to the benchmark

with higher main parameters (stiffness, stretchability, and conductivity). Interestingly,

DMSO activated hydrogel resulted in very different properties than the electrode doped with 5 wt.% DMSO, namely somewhat lower conductivity and superior stiffness and stretchability. Mainly, stretchability is the highest among all the developed electrode formulations.

When swelled, testing coupons increased their size by almost 90% in thickness, 45% in width, and 40% in length. After rehydration, hydrogel achieved the lowest stiffness from the materials studied in this research and considerably decreased but greater than 30% stretchability. The conductivity of the swelled coupons decreased approximately proportionally to the cross-section area increase (Table *5.3* and Figure 5.14b). While conductivity showed to be stable at 10 % of strain, further stretching material squeezed the DI water out of the material, interfering with the measurements. Lastly, utilization of hydrogel in DEA 3D printing brings certain inconveniences like the need to rehydrate each electrode layer and print hydrophobic elastomer materials on top of hydrophilic electrodes with the swelled (likely uneven) surface.

Table 5.3 Young's modulus and conductivity of the first hydrogen formulation (PEDOT:PSS – 13 wt.% DMSO – 80 wt.% Triton X-100) vs the benchmark PEDOT:PSS-Triton X-100 (80 wt.%) electrode.

Triton X-100 / Hydrogel	Young's modulus, MPa	Conductivity, S/cm
No DMSO	5.87	56.1
Unswelled	8.60	56
Swelled	0.383	17.3
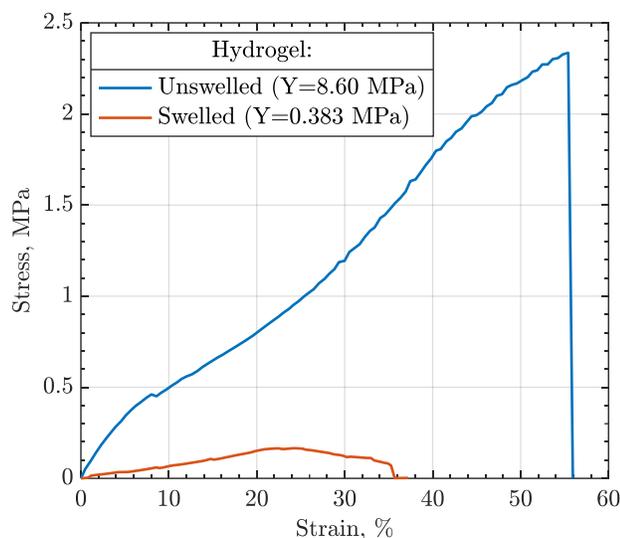
Figure 5.15 Stress-strain curves of the first hydrogel formulation (PEDOT:PSS - 13 wt.% DMSO – 80 wt.% Triton X-100).

Another issue with the prepared hydrogel is the DMSO rate of evaporation during the curing. For the DEA 3D printing process, this would result in waiting for anywhere between 30 min and few hours for curing a single layer of the electrode, which makes utilization of such hydrogel impractical.

An attempt was made to solve this issue by utilizing a different, more volatile solvent. As such, methanol was chosen as a PDMS-compatible solvent with a faster rate of evaporation. In addition, it was assumed that the high content of Triton X-100 in the first hydrogel formulation limited the degree of rehydration. Thus, smaller amounts of Triton X-100 were added after mixing PEDOT:PSS with methanol. However, this approach did not result in a stable hydrogel. Submerged in DI water for 10-15 sec, the material was completely losing its structural integrity. Thus, it was rehydrated by spraying DI water on the samples. The samples swelled considerably less than the first hydrogel formulation with DMSO, and their conductivity went down proportionally to a cross-section area increase. Samples were too delicate to perform tensile or conductivity at strains

measurements. Table *5.4* shows the conductivity measuring data for the unswelled

hydrogel. It shows the growing conductivity with the amount of Triton X-100 but lower

than for the first hydrogel with 80 wt.% of Triton X-100.

Table 5.4 Conductivity of the unswelled hydrogel prepared with methanol.

Triton X-100 / Hydrogel	0 wt.%	21.7 wt.%	50 wt.%
Conductivity, S/cm	3.5	~12	~17

5.2.4. Summary of the Second Electrode Composition

Effects of various mixing and heat treatment processes were studied, and various

strategies were presented (plasticizing, doping, and forming hydrogel) for greatest

electromechanical performance and printability of the electrode. Using the selected

mixing and heat treatment procedures for the benchmark PEDOT:PSS-Triton X-100 (80

wt.%), electrodes were meant to be improved through the three approaches.

Table 5.5 Most compliant electrode candidates and their performance.

Prepared electrode material	Young's modulus (Y), MPa	Conductivity (σ), S/cm	Stretchability (ε_{max}), %	Minimum printable thickness[a], μm	Sheet resistance, Ω/sq
80 wt.% Triton X-100 (5+2+5 mix)	5.87	56	~50	5	35.7
90 wt.% Triton X-100	0.879	19.8	~30	10	50.5
Hydrogel with DMSO (swelled)	0.383	17.3	~30-35	~10	57.8

[a] Practically achievable minimum thickness for a 50x10 mm electrode utilizing nScrypt 3Dn Series contact dispensing printer.

While no certain material showed the best performance for all three main parameters, PEDOT:PSS electrode with increased concentration of Triton X-100 and especially the hydrogel with DMSO demonstrated PDMS-like compliance with stretchability above 30% and conductivity of about 20 S/cm (Table *5.5*). Both electrodes doubled their minimum printable thickness; however, the softening effect is still more significant. Meanwhile, all the electrodes maintained their sheet resistance far below the typical values of carbon grease electrodes. As Table *5.5* shows, prepared hydrogel overperformed the highly plasticized electrode. However, when the manufacturability and stability of the electrodes are considered (Table *5.6*), the plasticized electrode with 90 wt.% of Triton X-100 is seen as a better candidate for the compliant DEA electrode.

Table 5.6 Printability and stability of the most compliant electrode candidates.

Prepared electrode material	Curing time for the electrode before next layer can be printed[a]	Additional steps	Stability
90 wt.% Triton X-100	5-10 min[b]	n/a	Stable as per remeasured properties one and two months after the initial tests
Hydrogel with DMSO (swelled)	> 10 h	Swelling (e.g., in DI water)	Dries in 2-3 days

[a] Estimated for the electrode with its minimum printable thickness. [b] Time varies based on the temperature raise time (counted from the start of heating bed to dry electrode).

6. Novel Bending DEA Configuration

As a single-layer, planar DEA produces only one-dimensional deformation, i.e., contraction-expansion, with a moderate actuation force, different actuation mechanisms, such as rolling or stacking DEAs, have been implemented to obtain larger deformations and higher actuation forces. However, these DEA configurations do not alter the fundamental type of thickness-wise deformation. In some applications, DEA's out-of-plane actuation motion, such as bending, is often desired for effective system operation. Currently, the desired types of DEA deformation are generally attained by implementing additional members or mechanisms using various means, e.g., stiff frames, unimorph or bimorph, multistable structures, preloaded mechanisms. Although the methods above enable DEAs to achieve desired motions, they can considerably constrain deformation and actuation force and mostly require manual assemblies. This chapter demonstrates a novel DEA capable of generating the needed range of motions without introducing additional elements within the actuator. This was accomplished by tailoring the electrode-elastomer pattern and thereby deforming the elastomer in the desired manner. Studied DEA design was first developed using theoretical basics about flat capacitors and then verified through finite element analysis. The designed actuator was additively manufactured using a contact microdispensing 3D printer and tested to validate its bending due to the tailored electric field.

6.1. Proposed Approach

As discussed earlier, most of the current methods to achieve out-of-plane DEA motion introduce additional stiffness and/or weight to actuating systems, often reducing their achievable deformations or specific energies. A new approach to produce out-of-

plane motions without adding non-integral components of DEA is desired to overcome

these drawbacks. Additionally, it is beneficial to maintain the planar shape of DEA to

enable its manufacturing through AM techniques. Therefore, this chapter proposes a

method of achieving out-of-plane motion through special DEA electrode-elastomer

patterns designed based on the fundamental DEA principle of work.

DEA operates utilizing an electrostatic field and is often explained through an

analogy of an infinite flat capacitor with dielectric material and electrodes replaced by an

elastomer and compliant conductive material. When voltage is applied to opposite

electrodes, one electrode receives an excess of electrons and becomes negatively charged,

while the second electrode experiences a lack of electrons and becomes positively

charged. In the infinite capacitor, such distribution of charges generates a uniform electric

field across the dielectric proportional to the applied voltage and attracts the electrodes.

In this fashion, the electrostatic force is utilized by DEAs to produce their thickness-wise

contraction and in-plane expansion due to the compliance and low compressibility of

typical DEA materials. However, real capacitors (and DEAs) are finite and do not have a

uniform electric field across all the dielectric, but the fringing effect at the edges of

electrodes, as illustrated in Figure 6.1a. The charges at the edges of electrodes are then

attracted to each other along the curved electric field lines. Furthermore, unevenly wide

electrodes would produce an even more distorted electric field due to the size difference

of electrodes and uneven charge density, as shown in Figure 6.1b. Observing electric

field distribution, it can be assumed that unevenly sized electrodes can lead to a "joint-

like" folding or bending of the DEA towards the smaller electrode due to the attraction of

electrode edges. Therefore, the current study aims to experimentally investigate the

possibility of such a "joint-like" bending due to the fringing field and numerically

evaluate the effect of DEA design parameters on the magnitude of the bending.
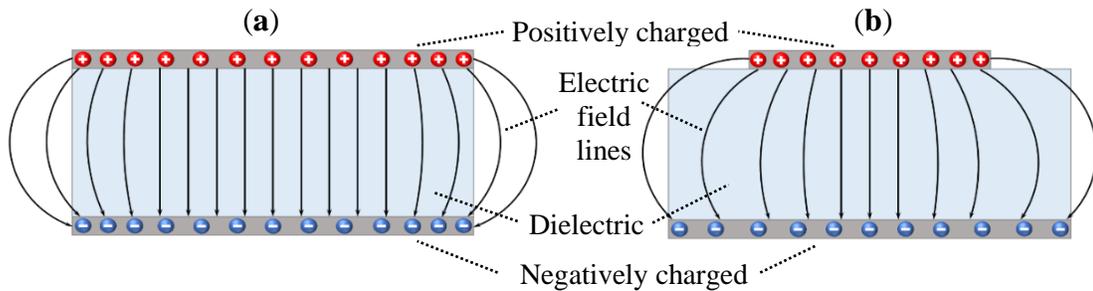
Figure 6.1 Schematics of an electric field in a finite capacitor with (a) even and (b) variable electrode width.

Employing the fringing effect is not novel for electromechanical devices. Particularly, it was successfully adopted to maximize the electroadhesive force for a DEA gripper by interdigitating its electrodes (Jun Shintake et al., 2016). While looking for an optimum design, the authors checked for electrodes' positioning with respect to each other to maximize the desired electroadhesion. Therefore, the effect of electrodes' positioning (spacing) on the "joint-like" bending was also addressed in the following analysis.

6.2. Numerical Evaluation of the Proposed Approach

To evaluate DEA design's effect on the "joint-like" bending due to the fringe field, a numerical parametric study is carried out in COMSOL Multiphysics v5.3. However, to ensure accurate analysis, the FEM simulation is firstly validated by comparing it with published experimental results of a similar DEA configuration (3D printed cantilever unimorph bending DEA) (Haghiashtiani et al., 2018).

6.2.1. Model Validation

A previous study on unimorph DEA is selected to validate the numerical analysis of this chapter as the study provides complete descriptions of the tested actuators and their material characteristics information sufficient for this work (Haghiashtiani et al., 2018). To enable electrostatic forces in DEA, the simulation is performed in Electromechanics Physics of COMSOL while modeling dielectric elastomer as a linear elastic dielectric, and electrodes and passive layer as linear elastic materials. After the actuator's geometry is fully replicated with the assigned materials, a fixed boundary condition (BC) is applied to one end of the beam. To simulate potential difference on electrodes, Ground BC is applied to the elastomer area in contact with the bottom electrode, and Terminal BC is applied to the elastomer area in contact with the top electrode. Integer values of electric potential between 1 and 5 kV, and then the maximum value of 5.44 kV, are applied on the Terminal BC to replicate the conducted reference testing. The beam tip deflection results are plotted with the experimental values in Figure 6.2.

As the comparison suggests, the numerical model matches the actuator's behavior well with acceptable accuracy, despite utilizing the linear material model. It can be explained by a relatively small electric field applied to a ~0.5 mm thick elastomer layer causing relatively small near-linear material deformation in the reference experiment. Hence, the numerical model can legitimately be used to simulate DEA behavior at relatively low electric fields, typical of most 3D printed DEAs (Kadooka et al., 2016a; Sikulskyi et al., 2020).
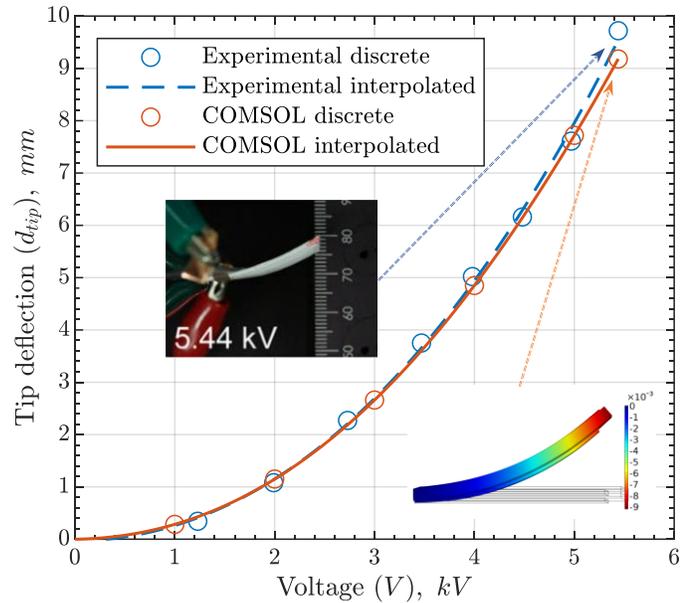
Figure 6.2 Validation of the COMSOL DEA model by comparing tip deflection of the reference actuator and its simulation.

6.2.2. Parametric Study

As described in Introduction, unevenly sized electrodes and other DEA design parameters can cause and affect the amount of the "joint-like" bending. Therefore, a numerical parametric study is carried out on a cantilever elastomer beam and a single pair of electrodes with varying geometrical parameters, as shown in Figure 6.3. Mainly, the parameters are electrodes' width ratio w_{bot}/w_{top}, electrodes' width $w_{top} = aw_{bot} = b$ (where a and b are arbitrary parameters), elastomer thickness t, and electrode spacing s. An elastomer beam is modeled as PDMS Sylgard 184 with Part A elastomer base mixed with Part B curing agent in a 15:1 ratio by weight (Young's modulus $Y = 0.673\ MPa$, dielectric permittivity $\varepsilon_r = 2.82$, breakdown strength $E_{BD} = 90.3\ V/\mu m$) (Sikulskyi et al., 2020). As simulation demonstrated, uneven electrode pairs result in bending motion of the novel DEA design towards the smaller electrode (Figure 6.4). Both setups were

tested to verify bending due to the electrode pair. Further numerical analysis was

conducted with a smaller top electrode.
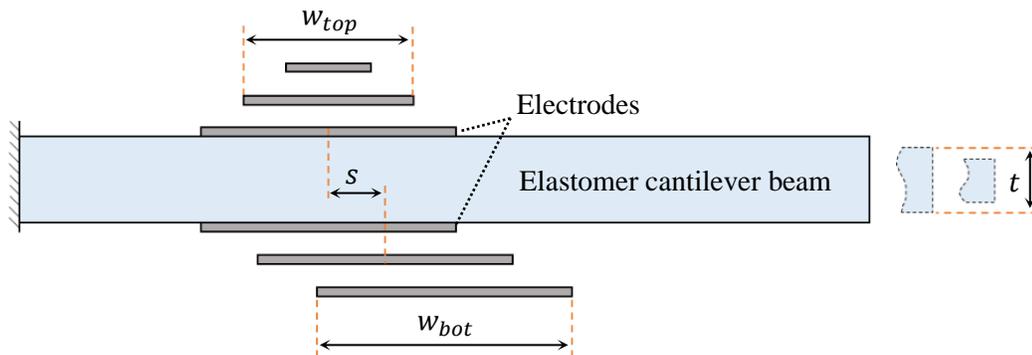
Figure 6.3 Schematics of an elastomer cantilever beam with a single pair of electrodes and variable parameters used in the numerical study. The beam is 20 mm in length and 5 mm in depth, with the common center of gravity of the electrode pair fixed at 5 mm from the cantilevered edge (including the case of variable electrodes' spacing).
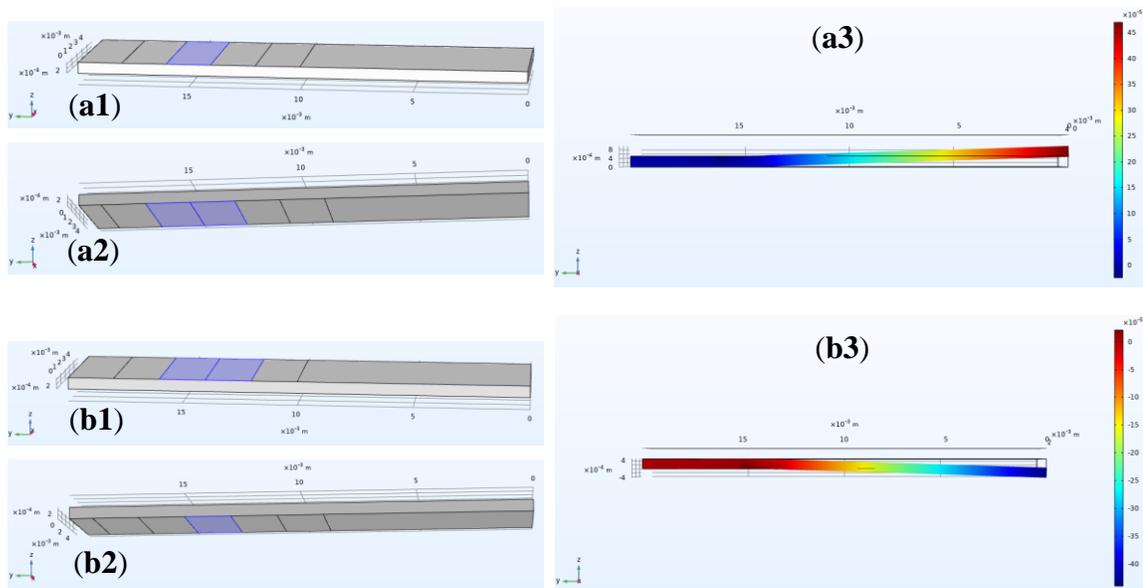
Figure 6.4 COMSOL models of the novel bending DEA uneven electrodes and their bending towards the smaller electrode. The actuator model with a smaller electrode (a1-a2) on the top results in (a3) upward actuator deflection. The actuator model with a smaller electrode (b1-b2) on the bottom results in (b3) downward actuator deflection.
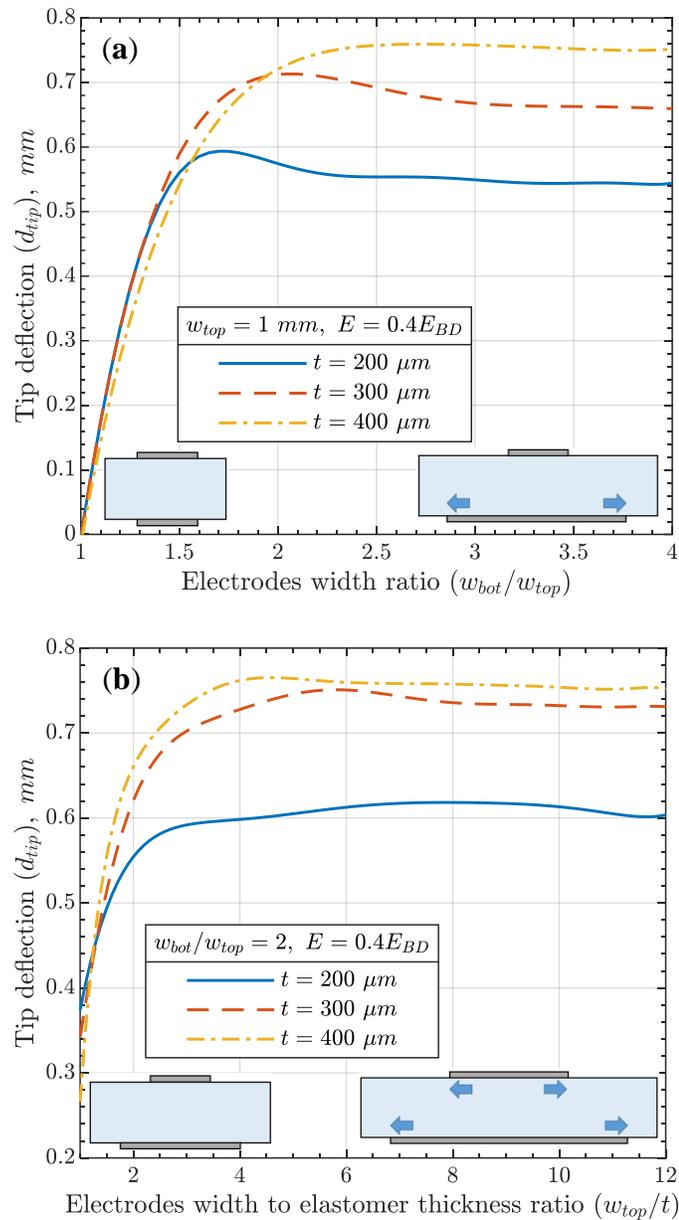
Figure 6.5 Parametric study results showing tip deflection of the elastomeric cantilever beam with a single pair of electrodes, varying (a) top and bottom electrodes width ratios, (b) elastomer thicknesses for fixed electrodes' width.

The parametric study output (beam tip deflection) is shown in Figure 6.5 and Figure 6.6 as functions of considered design variables. Firstly, the electrode width ratio is increased, starting from the even electrodes that do not provide any bending (Figure 6.5a). As the width ratio increases, the beam's capability to deflect grows drastically and then flattens.

The similar deflection behaviors are noticed with proportionally increasing electrodes'

width (Figure 6.5b). Both cases show that the elastomer thickness affects the maximum

deflection amount and electrodes' width ratio at which the curves flatten. Therefore, the

elastomer thickness effect is also studied for fixed-size electrodes (Figure 6.6a).
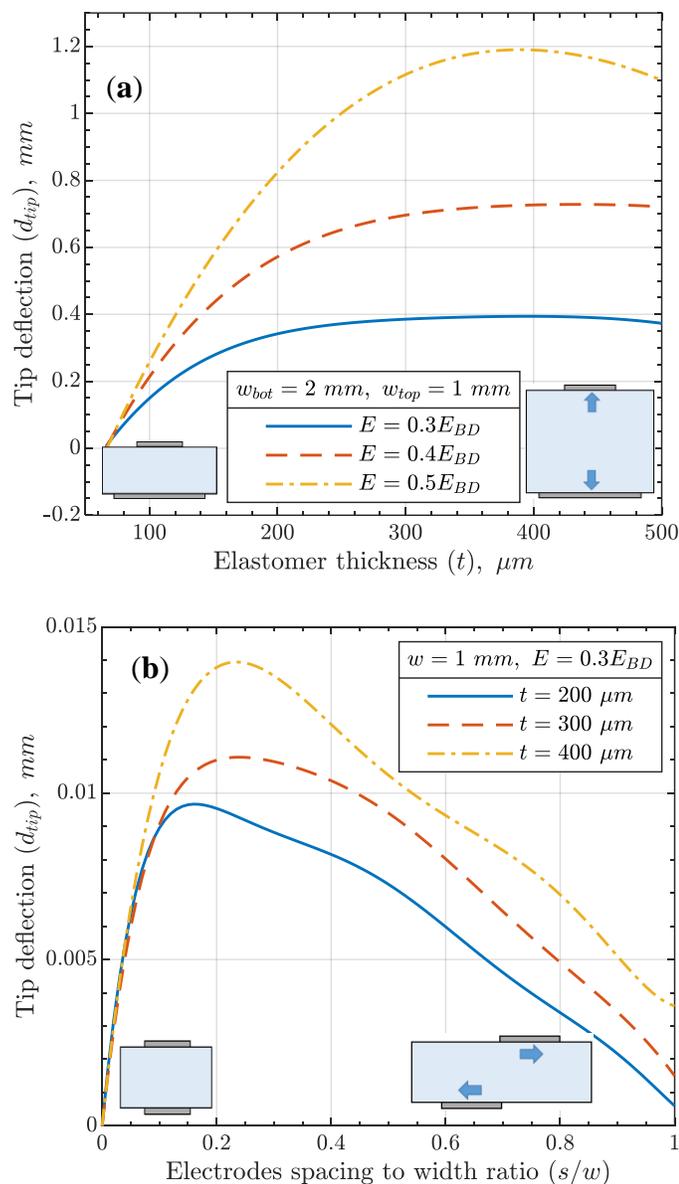
Figure 6.6 Parametric study results showing tip deflection of the elastomeric cantilever beam with a single pair of electrodes, varying (a) electrode width for fixed elastomer thicknesses, (b) electrodes spacing.

For the given electrode dimensions, the most extensive bending performance is achieved at top electrode width to elastomer thickness ratio of about $w_{top}/t = 3$, which corresponds to about 333 μm elastomer thickness. Interestingly, a thin elastomer can considerably degrade the proposed actuator's bending capability, which is not a trivial case for DEAs. Lastly, electrode spacing is checked as a potential approach to achieve actuator's bending; however, it does not show considerable effects yielding two orders less than the deflections caused by other parameters (Figure 6.6b).

Overall, the numerical parametric study showed that the "joint-like" bending of the proposed electrode pattern is possible. It can be recommended to choose a sufficient electrodes width and their width ratio to enable the "joint-like" bending, e.g., $w_{top}/w_{bot} \geq 2$ and $w_{top}/t \geq 4$ for actuators with a single electrode pair. If multiple electrode pairs are installed along the structure to obtain its continuous bending, the ratios should be wisely limited to fit more electrode pairs. Additionally, more attention should be paid to selecting the elastomer thickness to maximize DEA's bending.

6.3. Experimental Validation of the Proposed Approach

Based on the conducted numerical parametric study, a well-performing and suitable for the utilized AM method/apparatus actuator design was selected and fabricated through the system nScrypt 3Dn Series with the SmartPump contact microdispensing head. Actuation test was conducted on the fully printed novel bending DEA to validate the proposed concept experimentally.

6.3.1. Fabrication of the Novel Bending DEA Design

An actuator with a single pair of uneven electrodes is additively manufactured and tested in a cantilever configuration to validate the proposed concept experimentally. The

actuator's design is chosen so that it produces noticeable bending and can be adequately replicated using nScrypt 3Dn Series system with a SmartPump contact microdispensing head. For the final T-shaped actuator (Figure 6.7a), the stem part represents the actuator's bending portion meant to be cantilevered, and the arms represent elastomer-supported electrode connections. As the figure shows, two to one electrode width ratio ($w_{bot}/w_{top} = 2$) is employed for the elastomer thickness of $t = 250\ \mu m$, and top electrode width of 2 mm is used so that $w_{top}/t = 8$. In agreement with the numerical model, the elastomer part is 20 mm in length. However, its width is increased to 8 mm to accommodate the 5 mm depth electrode pair located 5 mm from the cantilever side. The actuator's materials include Sylgard 184 (15:1 mixing ratio) for the elastomer layer and 1.1 wt.% aqueous solution of PEDOT:PSS doped with a surfactant plasticizer Triton X-100 for the compliant and printable electrodes (Sikulskyi et al., 2020).

While searching for a way to peel off printed soft actuators from the printing bed safely, moderate adhesion is noticed between Sylgard 184 and BoPET, or Mylar. Therefore, fabrication of the designed bending actuator is performed according to the following procedure (Figure 6.7c). The first step is to flatten and tape a 2 μm thick Mylar film on the printing bed. The film is then covered with a thin auxiliary layer (<40 μm) of PDMS that enables peeling off the actuator, followed by printing the designed DEA. Another auxiliary layer of PDMS is coated on top of the DEA to maintain the actuator's symmetry and validate bending due to the proposed electrode pattern. Each printed layer is coated with parameters stated in Table *6.1* and finished by curing at 70°C for 5 min (for electrodes) and 10 min (for elastomer) and then the final curing at 70°C for 2 h.
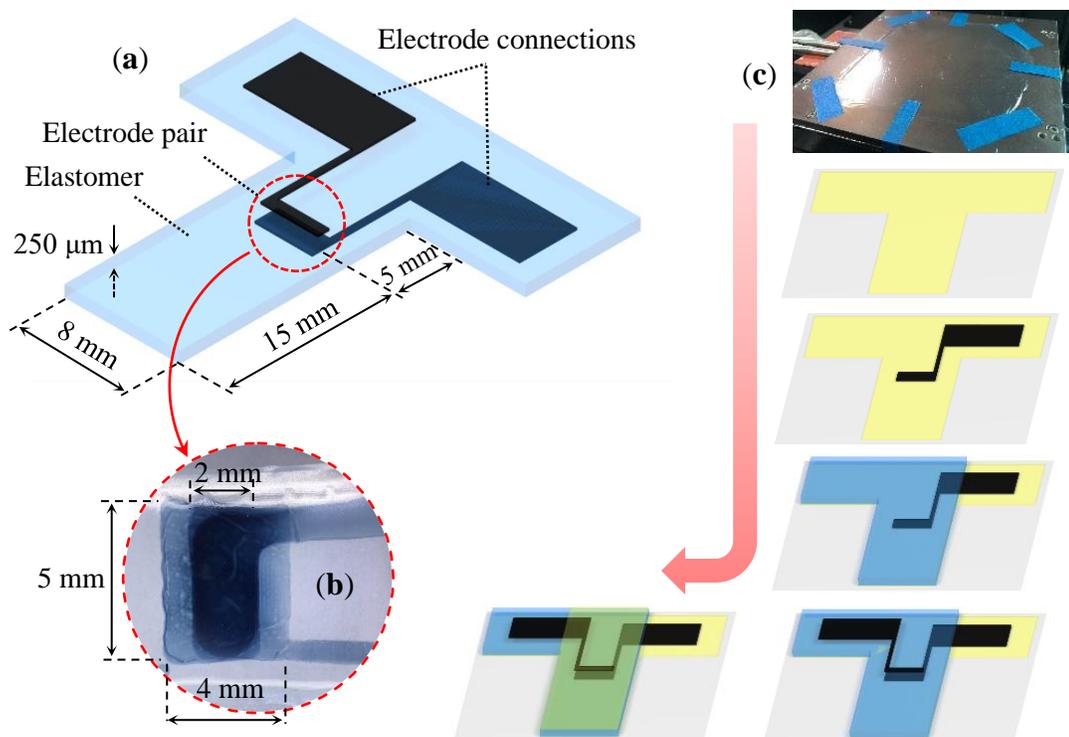
Figure 6.7 Bending DEA's (a) design (without auxiliary layers), (b) top view of the printed electrode pair, and (c) the fabrication process (the first picture represents flattening and taping 2 μm Mylar film; the rest of the pictures represent the successive printing of (following the arrow): bottom auxiliary elastomer layer, bottom electrode, dielectric elastomer, top electrode, top auxiliary elastomer layer).

Table 6.1 nScrypt 3Dn Series printing settings for the bending DEA.

	Nozzle diameter, μm	Printing height, μm	Printing speed, mm/s	Pressure, psi	Thickness, μm	
					Planned	Measured [b]
Electrode	125	90	10	1.3	5 [a] per layer (10 total)	8-10
Auxiliary layers		40	20		<40	25-30
Dielectric	250	110	12	3.2	125 per layer (250 total)	238-245

[a] Dry thickness (wet coated layer was estimated to be about 200 μm). [b] Each layer was measured at three locations across the actuator using an optical microscope.

6.3.2. Testing of the Novel Bending DEA Design

After the final curing, the actuator is peeled off from the Mylar film. Electrode connections are supported by a piece of Kapton tape from the elastomer side to ensure their structural integrity during handling and testing. Two copper electrodes are attached to the compliant electrode connections to apply voltage through TREK® 20/20CH-S amplifier. The actuator is then cantilevered and positioned vertically on the fixture. Figure 6.8 shows the actuator at 0 and 5.2 kV voltage applied. For the dielectric elastomer's thickness of 238 μm, the maximum reached electric field is ~22.3 V/μm that corresponds to ~$0.245E_{BD}$ (using the value of 91 V/μm for the breakdown strength of Sylgard 184 with components A and B mixed in a 15:1 ratio).

A "joint-like" bending of the elastomer beam can be noticed. Observing the actuator's overlapped states (Figure 6.8c), a left-directed (towards the smaller electrode), linearly increasing deflection can be seen starting from the electrode pair down to the beam's tip. Despite the auxiliary elastomer layers and the lower achieved electric field in the experiment than the $0.3E_{BD}$ used in numerical analysis, the actuator achieved larger deformation than predicted numerically. Additionally, a torsional deformation was noticed. As the layers' thicknesses are inspected to be relatively uniform not to cause an undesired deformation, it is assumed that the source of the torsional motion is the top electrode connection overlapping with the bottom electrode (Figure 6.7b). When the bending DEA is actuated, the uneven electrode pair tends to fold. The overlapped connection weakens the fringing field effect at the electrode's corner leading to the actuator's torsional motion. While the described design flaw likely decreases the

actuator's bending, a potential approach to achieve torsional motion through the electrodes' asymmetry is found.

5.2 kV
(~0.245E_{BD})

0.55 mm
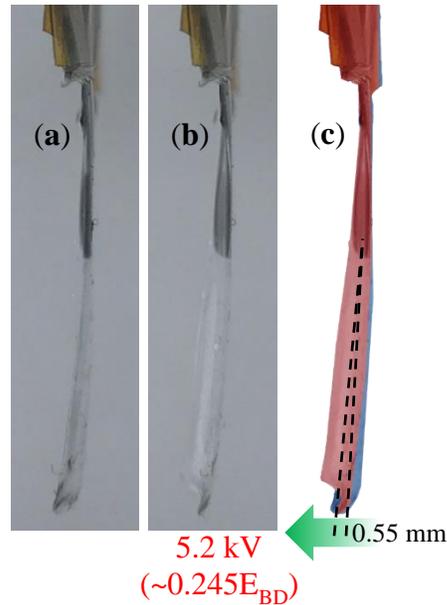
Figure 6.8 Actuation testing of the 3D printed DEA with the special electrode pattern: (a) at rest, (b) actuated, and (c) both states.

6.3.3. Novel Bending DEA with Multiple Electrode Pairs

After validating the concept and printability for the novel bending DEA, an actuator with multiple electrode pairs was fabricated and tested to achieve a larger deflection. To further remove uncertainties regarding the structural asymmetry due to auxiliary elastomer layer and potential stiffness difference in top and bottom electrodes, actuators were fabricated through a different procedure. A 450 µm elastomer film (Sylgard 182, 20:1 mix ratio) was applicated according to the procedure utilized in Chapter 4. Six electrode pairs sized as for the previous actuator with traces and connections were fabricated on both sides of the elastomer film by spraying carbon black dispersed in isopropanol through paper masks (Figure 6.9). Electrode material spraying was

performed utilizing airbrush Harder & Steenbeck ULTRA (Norderstedt, Germany) with

compressor PointZero 175X (Tamarac, FL, United States).
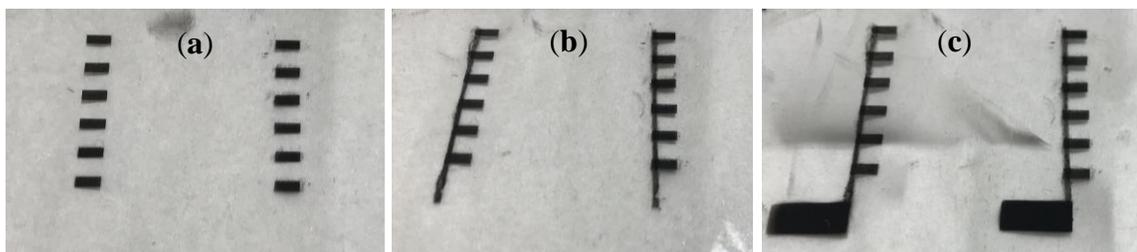
Figure 6.9 Fabrication process for carbon black electrodes (dispersed in isopropanol) on PDMS consisting of spraying (a) electrodes, (b) conductive traces, and (c) electrode connections.
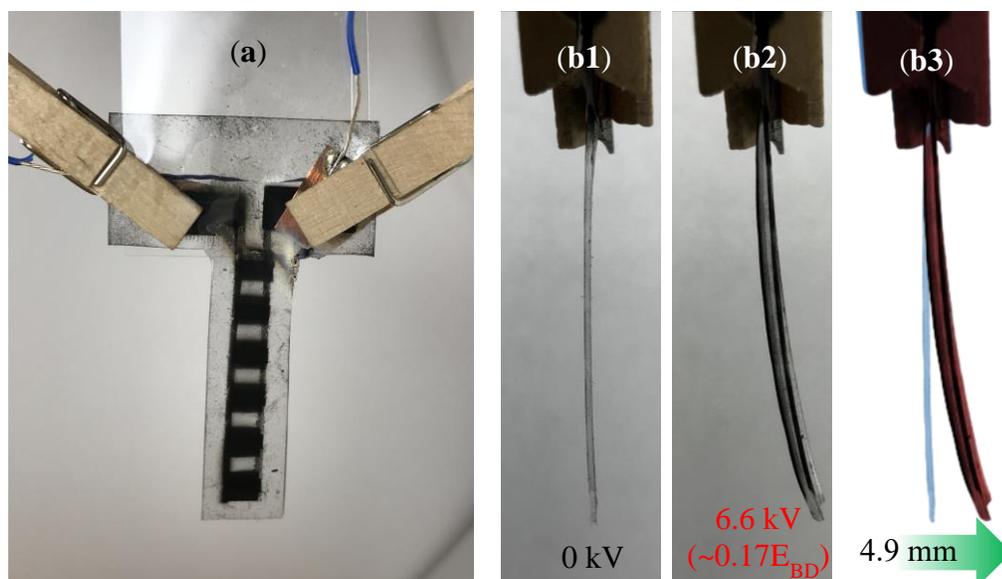
Figure 6.10 Actuation test (a) setup and the novel bending DEA with multiple electrode pairs (b1) at rest, (b2) actuated, and (b3) both states.

Fabricated actuators were cut to the desired shape and tested in the vertically

cantilevered mode (similarly to the subsection 6.3.2) as shown in Figure 6.10a. Tested

bending DEAs with six electrode pairs demonstrated larger tip deflections with the

relatively uniform curvature along the actuator (Figure 6.10b). As for the single-electrode

pair actuator, achieved deformation is greater at lower electric field than numerically predicted. Therefore, a more fundamental analysis is desired to thoroughly investigate potential reasons behind the better experimental performance of the actuators, such as special charge distribution across the electrode pairs and corresponding electric field.

6.4. Conclusions on the Novel Bending DEA

The novel principle of special electric field utilization to create bending motions in DEA without stiffening layers proved to be feasible through the 3D printed actuator with auxiliary elastomer layers and a completely unstiffened actuator fabricated through conventional methods. The study presented initial analysis and sizing of electrode pairs, elastomer, and actuator to increase the resultant DEA deflection. The results for both actuators with a single and multiple electrode pairs showed greater bending capabilities at lower electric field than numerically predicted, requiring a further investigation of the fringing field for the finite DEA with uneven electrodes.

7. Conclusions and Future Work

This chapter summarizes the essential conclusions and results of this research. Additionally, performed studies clearly direct future work for additively manufactured DEAs.

7.1. Conclusions

DEAs are promising smart materials driving soft actuator technology due to their superior performance. Considering DEAs' bi-material layered structure and compliant nature, their transition from conventional to additive manufacturing is not easy. Moreover, DEA's configuration, geometry, material selection, and fabrication techniques are interdependent and must be thoroughly considered to achieve high-quality DEA soft actuators. Nevertheless, as a recognized manufacturing approach for fabricating state-of-the-art DEA devices, 3D printing has recently experienced extensive development.

As a method of fabricating finished devices without intermediate manual steps, 3D printing focuses on fully printed non-prestretched DEAs. Thus, unimorph DEAs are often employed due to their ability to generate large bending deformations at relatively low strains without prestretch. As discussed, the absence of prestretch and low actuation strain allows a simple (linear) material model to fit experimental results. Meanwhile, geometrical nonlinearities should be considered in the modeling of DEA soft robots due to their large deflection and thickness. Thus, there is still considerable room for improvement to enable accurate modeling of the multimorph soft actuator.

Regardless of DEA configuration, the thickness of DE layers needs to be balanced to minimize the driving voltage while producing repetitive high-quality DEAs using the AM method and apparatus. Proper material selection, technological aspects, and DEA design

considerations are essential to avoid typical DEA defects, especially in stacked configurations. By analyzing various AM methods for fabricating DEAs, particular dispensing techniques such as contact dispensing, inkjet, and polyjet printing possess the capabilities to fully fabricate DEA soft actuators of various designs. Being the most flexible and currently utilized method, contact dispensing was employed in this research for fabricating DEAs with the derived recommendations. Through the testing of fabricated DEAs, it was shown that the quality of the actuators achieved by utilizing the derived recommendations was the highest within actuators fabricated through contact dispensing.

Considerable work was accomplished regarding enhancing the performance of printable DEA materials. DE properties were improved by integrating micro-sized highly dielectric fillers (BaTiO$_3$ and CCTO) into a PDMS (Sylgard 184) matrix to form composite DEA. While the fillers affected DE elasticity and dielectric characteristics, the DEA application's performance was evaluated through figures of merit to determine optimum filler loadings for various DEA objectives. Composite DEA with optimum CCTO loading was used for a prestretched DEA configuration, and 3D printed unimorph DEA to experimentally validate improved actuation performance and printability of the composite through contact dispensing.

The work on compliant conductive material for DEA electrodes was accomplished in two steps. The first step was choosing a strategy of employing intrinsically conductive polymers due to their ability to be greatly modified as a foundation for compliant electrode materials. Based on this decision, a modification of a conductive polymer (PEDOT:PSS with non-ionic surfactant plasticizer Triton X-100) with the compliance

suitable for DEA was replicated, further studied, and validated for the printed DEA application. For the second step, several techniques were employed to further soften the material while maintaining other interest properties within an appropriate range. These techniques included high plasticizer concentration, doping with solvents, and formation of hydrogels. Material characterization showed that increasing the content of Triton X-100 in PEDOT:PSS resulted in the lowest electrode stiffness.

Lastly, a novel 3D printable bending DEA configuration that does not employ stiffening elements in its design was proposed, numerically studied, fabricated, and experimentally validated. The method proposed utilizing the fringing field in the finite DEAs and modifying it through the special electrode-elastomer patterns such that it bends the actuator. Numerical parametric study helped choose the initial sizing for the actuator, which was fabricated and tested to show the concept's capabilities. In addition, the testing unveiled the potential to produce torsional deformations through the asymmetry of the modified electrodes.

7.2. Future Work

Despite single-layer DEAs printed according to the derived methodology achieved at least twice higher electric field than DEA fabricated through contact dispensing within the literature, considerable further improvement is possible implementing the recommendations, particularly micron-level precision leveling of flat printing beds. In addition, utilizing dielectric fillers with a smaller particle size in a composite DEA would be a practical approach to improve the properties of 3D printed DEAs, particularly their deflection capability and blocked force. However, this would require additional safety

considerations and possibly more sophisticated particle dispersing approaches. Thus, the most relevant future work on 3D printed DEAs is seen in the following aspects.

- *Stacked DEAs.* So far in the literature, the largest stacked 3D printed DEA had 10 DE layers and operated at about 8 % of its breakdown strength only. Configurations of DEA with numerous layers of elastomer and electrode require more efforts to maintain uniformity of each DE layer within the actuator, solve the issue of material spread, and accelerate the printing process. Some potential solutions include polymers that are highly viscous when uncured yet compliant when cured, to print the border of the actuator for each layer, fast curable UV sensitive DE and electrode materials, and likely increased DE thickness.

- *DEA electrode material.* While electrode performance was greatly increased in the present research, there is still no reliable quantitative relation between DEA actuation performance and some of the main electrode properties and parameters, namely conductivity and thickness (in terms of charge distribution). A fundamental study on DEA electrodes to establish these relations is desired. Having a quantitative tool to comprehensively evaluate electrode performance based on its properties for various DEA applications, i.e., DEA electrode figure of merit, researchers would be able to select and design DEA electrodes more methodically.

- *Novel bending DEA.* Further investigation of the fringing field in finite DEAs is needed to explain higher deflection capabilities and establish proper modeling. While printability of the concept was proven by using auxiliary elastomer layers to enable peeling off the actuator from printing bed, these thin isolative layers

allowed actuator reaching higher electric field compared to the tested non-isolated actuator with multiple electrode pairs. The solution is seen in benefitting from thin auxiliary elastomer layers, e.g., 20-30 µm, enabling printability and providing marginal stiffening effect for optimized DEA designed with larger DE thickness, e.g., 400 µm. Finally, a comprehensive comparison of optimized novel and unimorph actuators is in the scope of future work.

- *New and hybrid AM methods for 3D printed DEAs.* Another direction besides contact dispensing to approach high-quality 3D printed DEAs with a wide range of available material is polyjet printing. Thanks to its commercialization, high printing speed, sufficiently small layer thickness, and capability to utilize the range of materials comparable with contact dispensing, polyjet printing can become a solution for complex three-dimensional soft actuators and biomimetic soft robots. Lastly, the implementation of hybrid systems consisted of contact dispensing, or polyjet, head printing elastomer (for wide range of printable elastomers) and inkjet head printing electrodes (for fast printing thin electrodes) would also enable fast printing of high-quality DEA with complex three-dimensional geometry.

REFERENCES

Ahmadipour, M., Ain, M. F., & Ahmad, Z. A. (2016). A Short Review on Copper Calcium Titanate (CCTO) Electroceramic: Synthesis, Dielectric Properties, Film Deposition, and Sensing Application. *Nano-Micro Letters, 8*(4), 291-311. doi:10.1007/s40820-016-0089-1

Araromi, O., Gavrilovich, I., Shintake, J., Rosset, S., Richard, M., Gass, V., & Shea, H. (2015). Rollable Multisegment Dielectric Elastomer Minimum Energy Structures for a Deployable Microsatellite Gripper. *IEEE/ASME Transactions on Mechatronics, 20*, 438-446. doi:10.1109/TMECH.2014.2329367

Araromi, O., Rosset, S., & Shea, H. (2015). *Versatile fabrication of PDMS-carbon electrodes for silicone dielectric elastomer transducers.* Paper presented at the 18th International Conference on Solid-State Sensors, Actuators and Microsystems (Transducers).

Araromi, O. A., & Burgess, S. C. (2012). A finite element approach for modelling multilayer unimorph dielectric elastomer actuators with inhomogeneous layer geometry. *Smart Materials and Structures, 21*(3), 032001. doi:10.1088/0964-1726/21/3/032001

Araromi, O. A., Conn, A. T., Ling, C. S., Rossiter, J. M., Vaidyanathan, R., & Burgess, S. C. (2011). Spray deposited multilayered dielectric elastomer actuators. *Sensors and Actuators A: Physical, 167*(2), 459-467. doi:10.1016/j.sna.2011.03.004

Arruda, E. M., & Boyce, M. C. (1993). A three-dimensional constitutive model for the large stretch behavior of rubber elastic materials. *Journal of the Mechanics and Physics of Solids, 41*(2), 389-412. doi:10.1016/0022-5096(93)90013-6

Babu, S., Singh, K., & Govindan, A. (2012). Dielectric properties of CaCu3Ti4O12–silicone resin composites. *Applied Physics A, 107*. doi:10.1007/s00339-012-6885-7

Baechler, C., Gardin, S., Abuhimd, H., & Kovacs, G. (2016). Inkjet printed multiwall carbon nanotube electrodes for dielectric elastomer actuators. *Smart Materials and Structures, 25*(5), 055009. doi:10.1088/0964-1726/25/5/055009

Barber, P., Balasubramanian, S., Anguchamy, Y., Gong, S., Wibowo, A., Gao, H., . . . zur Loye, H.-C. (2009). Polymer Composite and Nanocomposite Dielectric Materials for Pulse Power Energy Storage. *Materials, 2*(4), 1697-1733. doi:10.3390/ma2041697

Bele, A., Tugui, C., Asandulesa, M., Daniela, I., Vasiliu, L., Stiubianu, G., . . . Cazacu, M. (2018). Conductive stretchable composites properly engineered to develop highly compliant electrodes for dielectric elastomer actuators. *Smart Materials and Structures, 27*, 105005. doi:10.1088/1361-665X/aad977

Benslimane M Y, K. H. E., & Tryson, M. J. (2010). Dielectric electro-active polymer push actuators: performance and challenges. *Polymer International, 59*, 415. Retrieved from doi:10.1002/pi.2768

Bhattacharjee, N., Parra-Cabrera, C., Kim, Y., Kuo, A., & Folch, A. (2018). Desktop-Stereolithography 3D-Printing of a Poly(dimethylsiloxane)-Based Material with Sylgard-184 Properties. *Advanced Materials, 30*. doi:10.1002/adma.201800001

Branwood, A., Hurd, J. D., & Tredgold, R. H. (1962). Dielectric breakdown in barium titanate. *British Journal of Applied Physics, 13*(10), 528-528. doi:10.1088/0508-3443/13/10/123

Brochu, P., & Pei, Q. (2010). Advances in dielectric elastomers for actuators and artificial muscles. *Macromolecular Rapid Communications, 31*, 10. Retrieved from doi:10.1002/marc.v31:1

Çabuk, O., Wegener, M., Gruber, B., Seidel, S.-O., & Maas, J. (2020). *Inkjet printing and characterization of applied electrodes for dielectric elastomer transducer.* Paper presented at the SPIE Smart Structures + Nondestructive Evaluation.

Cacucciolo, V., Shintake, J., Kuwajima, Y., Maeda, S., Floreano, D., & Shea, H. (2019). Stretchable pumps for soft machines. *Nature, 572*(7770), 516-519. doi:10.1038/s41586-019-1479-6

Cai, Z., Wang, X., Luo, B., Hong, W., Wu, L., & Li, L. (2017). Dielectric response and breakdown behavior of polymer-ceramic nanocomposites: The effect of nanoparticle distribution. *Composites Science and Technology, 145*, 105-113. doi:doi.org/10.1016/j.compscitech.2017.03.039

Carpi, F., Anderson, I., Bauer, S., Frediani, G., Gallone, G., Gei, M., . . . Shea, H. (2015). Standards for dielectric elastomer transducers. *Smart Materials and Structures, 24*(10), 105025. doi:10.1088/0964-1726/24/10/105025

Carpi, F., Salaris, C., & Rossi, D. D. (2007). Folded dielectric elastomer actuators. *Smart Materials and Structures, 16*(2), S300-S305. doi:10.1088/0964-1726/16/2/s15

Chemicals, M. (2015). Carbon Conductive Greases. Retrieved from https://www.mgchemicals.com/downloads/pdf/flyers/Carbon_Conductive_Greases_flyer.pdf. Retrieved 6.26.2021

Chen, F., Liu, K., & Zhu, X. (2019, 3-8 Nov. 2019). *Buckling-induced Shape Morphing using Dielectric Elastomer Actuators Patterned with Spatially-varying Electrodes.* Paper presented at the 2019 IEEE/RSJ International Conference on Intelligent Robots and Systems (IROS).

Chen, Y., Zhao, H., Mao, J., Chirarattananon, P., Helbling, E., Hyun, N.-s., . . . Wood, R. (2019). Controlled flight of a microrobot powered by soft artificial muscles. *Nature, 575*. doi:10.1038/s41586-019-1737-7

Cheng, B., Lin, Y.-H., Deng, W., Cai, J., Lan, J., Nan, C.-W., . . . He, J. (2012). Dielectric and nonlinear electrical behaviors of Ce-doped CaCu3Ti4O12 ceramics. *Journal of Electroceramics, 29*(4), 250-253. doi:10.1007/s10832-012-9768-6

Choi, S., Park, J., Hyun, W., Kim, J., Kim, J., Lee, Y. B., . . . Kim, D.-H. (2015). Stretchable Heater Using Ligand-Exchanged Silver Nanowire Nanocomposite for Wearable Articular Thermotherapy. *ACS Nano, 9*(6), 6626-6633. doi:10.1021/acsnano.5b02790

Choi, S. T., Kwon, J. O., & Bauer, F. (2013). Multilayered relaxor ferroelectric polymer actuators for low-voltage operation fabricated with an adhesion-mediated film transfer technique. *Sensors and Actuators A: Physical, 203*, 282-290. doi:10.1016/j.sna.2013.08.049

Chortos, A., Hajiesmaili, E., Morales, J., Clarke, D. R., & Lewis, J. A. (2020). 3D Printing of Interdigitated Dielectric Elastomer Actuators. *Advanced Functional Materials, 30*(1), 1907375. doi:10.1002/adfm.201907375

Chun, K.-Y., Oh, Y., Rho, J., Ahn, J.-H., Kim, Y.-J., Choi, H., & Baik, S. (2010). Highly conductive, printable and stretchable composite films of carbon nanotubes and silver. *Nature nanotechnology, 5*, 853-857. doi:10.1038/nnano.2010.232

Church, K. (2020). Microdispensing Processes. In D. L. Bourell, W. Frazier, H. Kuhn, & M. Seifi (Eds.), *Additive Manufacturing Processes* (Vol. 24, pp. 0): ASM International.

Coulter, F., Coulter, B., Marks, J., & Ianakiev, A. (2018). Production Techniques for 3D Printed Inflatable Elastomer Structures: Part I—Fabricating Air-Permeable Forms and Coating with Inflatable Silicone Membranes via Spray Deposition. *3D Printing and Additive Manufacturing, 5*(1), 5-16. doi:10.1089/3dp.2017.0068

Coulter, F., Coulter, B., Papastavrou, E., & Ianakiev, A. (2018). Production Techniques for 3D Printed Inflatable Elastomer Structures: Part II—Four-Axis Direct Ink Writing on Irregular Double-Curved and Inflatable Surfaces. *3D Printing and Additive Manufacturing, 5*(1), 17-28. doi:10.1089/3dp.2017.0069

Creegan, A., & Anderson, I. (2014). *3D Printing for Dielectric Elastomers.* Paper presented at the Electroactive Polymer Actuators and Devices.

Cui, Z. (2019). *Silver Nanowire-based Flexible and Stretchable Devices: Applications and Manufacturing.* (Doctor of Philosophy). North Carolina State University.

Dandan Satia, M. S., Jaafar, M., & Julie, M. (2014). Properties of calcium copper titanate and barium titanate filled epoxy composites for electronic applications: effect of filler loading and hybrid fillers. *Journal of Materials Science: Materials in Electronics, 25*, 4923-4932. doi:10.1007/s10854-014-2253-z

Dauzon, E., Mansour, A., Khan niazi, M., Munir, R., Smilgies, D. M., Sallenave, X., . . . Amassian, A. (2019). Conducting and Stretchable PEDOT:PSS Electrodes: Role of Additives on Self-Assembly, Morphology and Transport. *ACS Applied Materials & Interfaces, 11*. doi:10.1021/acsami.9b00934

Della-Schiava, N., Thetpraphi, K., Le, M.-Q., Lermusiaux, P., Millon, A., Capsal, J.-F., & Cottinet, P.-J. (2018). Enhanced Figures of Merit for a High-Performing Actuator in Electrostrictive Materials. *Polymers, 10*, 263. doi:10.3390/polym10030263

Du, Y., Cui, X., Li, L., Tian, H., Yu, W.-X., & Zhou, Z.-X. (2018). Dielectric Properties of DMSO-Doped-PEDOT:PSS at THz Frequencies. *physica status solidi (b), 255*(4), 1700547. doi:doi:10.1002/pssb.201700547

Duan, L., Wang, G., Zhang, Y., Zhang, Y., Wei, Y., Wang, Z., & Zhang, M. (2016). High dielectric and actuated properties of silicone dielectric elastomers filled with magnesium-doped calcium copper titanate particles. *Polymer Composites*, n/a-n/a. doi:10.1002/pc.23986

Duduta, M., Clarke, D. R., & Wood, R. J. (2017, 29 May-3 June 2017). *A high speed soft robot based on dielectric elastomer actuators.* Paper presented at the 2017 IEEE International Conference on Robotics and Automation (ICRA).

Duduta, M., Hajiesmaili, E., Zhao, H., Wood, R., & Clarke, D. (2019). Realizing the potential of dielectric elastomer artificial muscles. *Proceedings of the National Academy of Sciences, 116*, 201815053. doi:10.1073/pnas.1815053116

Duduta, M., Wood, R., & Clarke, D. (2016). Multilayer Dielectric Elastomers for Fast, Programmable Actuation without Prestretch. *Advanced Materials, 28*. doi:10.1002/adma.201601842

Ertuğ, B. (2013a). Electrical Conductivity and Hysteresis Characteristic of BaTiO3-Based Sensors with Polymethyl metacrylate (PMMA) Pore Former. *Sensors and Materials, 25*, 309-321.

Ertuğ, B. (2013b). The Overview of the Electrical Properties of Barium Titanate. *American Journal of Engineering Research, 2*, 01-07.

Fan, X., Nie, W., Tsai, H., Wang, N., Huang, H., Cheng, Y., . . . Xia, Y. (2019). PEDOT:PSS for Flexible and Stretchable Electronics: Modifications, Strategies, and Applications. *Advanced Science, 6*(19), 1900813. doi:10.1002/advs.201900813

Fisk, W. J., Faulkner, D., Sullivan, D., & Mendell, M. J. (2000). Particle Concentrations and Sizes with Normal and High Efficiency Air Filtration in a Sealed Air-Conditioned Office Building. *Aerosol Science and Technology, 32*(6), 527-544. doi:10.1080/027868200303452

Fralick, B. S., Gatzke, E. P., & Baxter, S. C. (2012). Three-dimensional evolution of mechanical percolation in nanocomposites with random microstructures. *Probabilistic Engineering Mechanics, 30*, 1-8. doi:doi.org/10.1016/j.probengmech.2012.02.002

Franke, M., Ehrenhofer, A., Lahiri, S., Henke, E.-F. M., Wallmersperger, T., & Richter, A. (2020). Dielectric Elastomer Actuator Driven Soft Robotic Structures With Bioinspired Skeletal and Muscular Reinforcement. *Frontiers in Robotics and AI, 7*(178). doi:10.3389/frobt.2020.510757

Fu, S.-Y., Feng, X.-Q., Lauke, B., & Mai, Y.-W. (2008). Effects of particle size, particle/matrix interface adhesion and particle loading on mechanical properties of particulate–polymer composites. *Composites Part B: Engineering, 39*(6), 933-961. doi:doi.org/10.1016/j.compositesb.2008.01.002

Gent, A. N. (1996). A New Constitutive Relation for Rubber. *Rubber Chemistry and Technology, 69*(1), 59-61. doi:10.5254/1.3538357

Gul, J. Z., Sajid, M., Rehman, M. M., Siddiqui, G. U., Shah, I., Kim, K.-H., . . . Choi, K. H. (2018). 3D printing for soft robotics – a review. *Science and Technology of Advanced Materials, 19*(1), 243-262. doi:10.1080/14686996.2018.1431862

Guo-Ying, G., Jian, Z., Li-Min, Z., & Xiangyang, Z. (2017). A survey on dielectric elastomer actuators for soft robots. *Bioinspiration & Biomimetics, 12*(1), 011003.

Guo, B., Glavas, L., & Albertsson, A.-C. (2013). Biodegradable and electrically conducting polymers for biomedical applications. *Progress in Polymer Science, 38*(9), 1263-1286. doi:10.1016/j.progpolymsci.2013.06.003

Gupta, U., Qin, L., Wang, Y., Godaba, H., & Zhu, J. (2019). Soft robots based on dielectric elastomer actuators: a review. *Smart Materials and Structures, 28*(10), 103002. doi:10.1088/1361-665x/ab3a77

Ha, S. M., Yuan, W., Pei, Q., Pelrine, R., & Stanford, S. (2006). Interpenetrating Polymer Networks for High-Performance Electroelastomer Artificial Muscles. *Advanced Materials, 18*(7), 887-891. doi:10.1002/adma.200502437

Haghiashtiani, G., Habtour, E., Park, S.-H., Gardea, F., & McAlpine, M. C. (2018). 3D printed electrically-driven soft actuators. *Extreme Mechanics Letters, 21*, 1-8. doi:10.1016/j.eml.2018.02.002

Hajiesmaili, E., & Clarke, D. (2019). Reconfigurable shape-morphing dielectric elastomers using spatially varying electric fields. *Nature Communications, 10*. doi:10.1038/s41467-018-08094-w

He, B., Yang, S., Qin, Z., Wen, B., & Zhang, C. (2017). The roles of wettability and surface tension in droplet formation during inkjet printing. *Scientific Reports, 7*(1), 11841. doi:10.1038/s41598-017-12189-7

Hines, L., Petersen, K., Lum, G. Z., & Sitti, M. (2017). Soft Actuators for Small-Scale Robotics. *Advanced Materials, 29*(13), 1603483. doi:10.1002/adma.201603483

Hong, S., Lee, S., & Kim, D. (2019). Materials and Design Strategies of Stretchable Electrodes for Electronic Skin and its Applications. *Proceedings of the IEEE, 107*(10), 2185-2197.

Hosford, W. F. (2009). *Mechanical Behavior of Materials* (2 ed.). Cambridge: Cambridge University Press.

Huang, J., Shian, S., Diebold, R. M., Suo, Z., & Clarke, D. R. (2012). The thickness and stretch dependence of the electrical breakdown strength of an acrylic dielectric elastomer. *Applied Physics Letters, 101*(12), 122905. doi:10.1063/1.4754549

Huang, S., Liu, Y., Zhao, Y., Ren, Z., & Guo, C. F. (2019). Flexible Electronics: Stretchable Electrodes and Their Future. *Advanced Functional Materials, 29*(6), 1805924. doi:10.1002/adfm.201805924

Imamura, H., Kadooka, K., & Taya, M. (2017). A variable stiffness dielectric elastomer actuator based on electrostatic chucking. *Soft Matter, 13*(18), 3440-3448. doi:10.1039/C7SM00546F

ISO. (2020). Air quality - General aspects - Vocabulary. In *ISO 4245:2020*: International Organization for Standardization.

Jeerapan, I., & Poorahong, S. (2020). Review—Flexible and Stretchable Electrochemical Sensing Systems: Materials, Energy Sources, and Integrations. *Journal of The Electrochemical Society, 167*(3), 037573. doi:10.1149/1945-7111/ab7117

Ji, X., Liu, X., Cacucciolo, V., Imboden, M., Civet, Y., El Haitami, A., . . . Shea, H. (2019). An autonomous untethered fast soft robotic insect driven by low-voltage dielectric elastomer actuators. *Science Robotics, 4*(37), eaaz6451. doi:10.1126/scirobotics.aaz6451

Jiyu, C. (2016). *4D Printing Dielectric Elastomer Actuator Based Soft Robots.* (Master of Science Dissertation). University of Arkansas, Fayetteville, AR.

John, A., Nadia, C., Sami, F., & Culley, B. (2016). Soft Robotics Commercialization: Jamming Grippers from Research to Product. *Soft Robotics, 3*(4), 213-222. doi:10.1089/soro.2016.0021

Jung rag, Y., Han, J.-W., & Lee, K.-M. (2009). Dielectric Properties of Polymer-ceramic Composites for Embedded Capacitors. *Transactions on Electrical and Electronic Materials, 10*, 116-120. doi:10.4313/TEEM.2009.10.4.116

Kadooka, K. (2017). *Modeling, processing, and characterization of dielectric elastomer actuators and sensors.* (Doctor of Philosophy Dissertation). University of Washington, Seattle, WA.

Kadooka, K., Imamura, H., & Taya, M. (2016a). Experimentally verified model of viscoelastic behavior of multilayer unimorph dielectric elastomer actuators. *Smart Materials and Structures, 25*(10), 105028. doi:10.1088/0964-1726/25/10/105028

Kadooka, K., Imamura, H., & Taya, M. (2016b). *Tactile sensor integrated dielectric elastomer actuator for simultaneous actuation and sensing.* Paper presented at the SPIE Smart Structures and Materials + Nondestructive Evaluation and Health Monitoring.

Kaneto, K. (2016). Research Trends of Soft Actuators based on Electroactive Polymers and Conducting Polymers. *Journal of Physics: Conference Series, 704*, 012004. doi:10.1088/1742-6596/704/1/012004

Kaur, G., Adhikari, R., Cass, P., Bown, M., & Gunatillake, P. (2015). Electrically conductive polymers and composites for biomedical applications. *RSC Advances, 5*(47), 37553-37567. doi:10.1039/C5RA01851J

Kayser, L. V., & Lipomi, D. J. (2019). Stretchable Conductive Polymers and Composites Based on PEDOT and PEDOT:PSS. *Advanced Materials, 31*(10), 1806133. doi:10.1002/adma.201806133

Keplinger, C., Li, T., Baumgartner, R., Suo, Z., & Bauer, S. (2011). Harnessing snap-through instability in soft dielectrics to achieve giant voltage-triggered deformation. *Soft Matter, 8*, 285-288. doi:10.1039/C1SM06736B

Kim, J., Kim, J. W., Kim, H. C., Zhai, L., Ko, H.-U., & Muthoka, R. M. (2019). Review of Soft Actuator Materials. *International Journal of Precision Engineering and Manufacturing, 20*(12), 2221-2241. doi:10.1007/s12541-019-00255-1

Kim, S., Cho, S., Lee, S. J., Lee, G., Kong, M., Moon, S., . . . Jeong, U. (2017). Boosting up the electrical performance of low-grade PEDOT:PSS by optimizing non-ionic surfactants. *Nanoscale, 9*(41), 16079-16085. doi:10.1039/C7NR05584F

Kim, W. J., Taya, M., & Nguyen, M. N. (2009). Electrical and thermal conductivities of a silver flake/thermosetting polymer matrix composite. *Mechanics of Materials, 41*(10), 1116-1124. doi:10.1016/j.mechmat.2009.05.009

Klug, F., Solano-Arana, S., Mößinger, H., Foerster-Zuegel, F., & Schlaak, H. (2017). *Fabrication of dielectric elastomer stack transducers (DEST) by liquid deposition modeling*.

Kollosche, M., Kofod, G., Suo, Z., & Zhu, J. (2015). Temporal evolution and instability in a viscoelastic dielectric elastomer. *Journal of the Mechanics and Physics of Solids, 76*, 47-64. doi:10.1016/j.jmps.2014.11.013

Koo, I., Jung, K., Koo, J., Nam, J., Lee, Y., & Choi, H. R. (2006, 18-21 Oct. 2006). *Wearable Fingertip Tactile Display.* Paper presented at the 2006 SICE-ICASE International Joint Conference.

Kovacs, G., During, L., Michel, S., & Terrasi, G. (2009). Stacked dielectric elastomer actuator for tensile force transmission. *Sensors and Actuators, A: Physical, 155*(2), 299-307. doi:10.1016/j.sna.2009.08.027

Kovacs, G., Düring, L., Michel, S., & Terrasi, G. (2009). Stacked dielectric elastomer actuator for tensile force transmission. *Sensors and Actuators A: Physical, 155*(2), 299-307. doi:doi.org/10.1016/j.sna.2009.08.027

Kraft, U., Molina-Lopez, F., Son, D., Bao, Z., & Murmann, B. (2020). Ink Development and Printing of Conducting Polymers for Intrinsically Stretchable Interconnects and Circuits. *Advanced Electronic Materials, 6*(1), 1900681. doi:10.1002/aelm.201900681

Lai, W., Bastawros, A., & Hong, W. (2012). *Out-of-plane motion of a planar dielectric elastomer actuator with distributed stiffeners.* Paper presented at the SPIE Smart Structures and Materials + Nondestructive Evaluation and Health Monitoring.

Lang, U., Naujoks, N., & Dual, J. (2009). Mechanical characterization of PEDOT:PSS thin films. *Synthetic Metals, 159*, 473-479. doi:10.1016/j.synthmet.2008.11.005

Li, J., Godaba, H., Zhang, Z. Q., Foo, C. C., & Zhu, J. (2018). A soft active origami robot. *Extreme Mechanics Letters, 24*, 30-37. doi:10.1016/j.eml.2018.08.004

Li, P., Sun, K., & Ouyang, J. (2015). Stretchable and Conductive Polymer Films Prepared by Solution Blending. *ACS Applied Materials & Interfaces, 7*. doi:10.1021/acsami.5b04492

Li, T., Chen, Z., Chang, F., Hao, J., & Zhang, J. (2009). The effect of Eu2O3 doping on CaCu3Ti4O12 varistor properties. *Journal of Alloys and Compounds, 484*(1), 718-722. doi:doi.org/10.1016/j.jallcom.2009.05.025

Lipomi, D. J., Lee, J. A., Vosgueritchian, M., Tee, B. C. K., Bolander, J. A., & Bao, Z. (2012). Electronic Properties of Transparent Conductive Films of PEDOT:PSS on Stretchable Substrates. *Chemistry of Materials, 24*(2), 373-382. doi:10.1021/cm203216m

Lotz, P., Matysek, M., Lechner, P., Hamann, M., & Schlaak, H. (2008). Dielectric elastomer actuators using improved thin film processing and nanosized particles. *Electroactive Polymer Actuators and Devices (EAPAD); San Diego*. doi:10.1117/12.776197

Lotz, P., Matysek, M., & Schlaak, H. (2011). Fabrication and Application of Miniaturized Dielectric Elastomer Stack Actuators. *Mechatronics, IEEE/ASME Transactions on, 16*, 58-66. doi:10.1109/TMECH.2010.2090164

Lu, N., & Kim, D.-H. (2014). Flexible and Stretchable Electronics Paving the Way for Soft Robotics. *Soft Robotics, 1*, 53-62. doi:10.1089/soro.2013.0005

Lu, T., Huang, J., Jordi, C., Kovacs, G., Huang, R., Clarke, D. R., & Suo, Z. (2012). Dielectric elastomer actuators under equal-biaxial forces, uniaxial forces, and uniaxial constraint of stiff fibers. *Soft Matter, 8*(22), 6167-6173. doi:10.1039/C2SM25692D

Luan, Y., Wang, H., & Zhu, Y. (2010). Design and Implementation of Cone Dielectric Elastomer Actuator with Double-Slider Mechanism. *Journal of Bionic Engineering, 7*, S212-S217. doi:10.1016/S1672-6529(09)60237-7

Luo, R., Li, H., Du, B., Zhou, S., & Zhu, Y. (2019). A simple strategy for high stretchable, flexible and conductive polymer films based on PEDOT:PSS-PDMS blends. *Organic Electronics, 76*, 105451. doi:10.1016/j.orgel.2019.105451

Ma, Z., Kong, D., Pan, L., & Bao, Z. (2020). Skin-inspired electronics: emerging semiconductor devices and systems. *Journal of Semiconductors, 41*(4), 041601. doi:10.1088/1674-4926/41/4/041601

Madsen, F. B., Daugaard, A. E., Hvilsted, S., & Skov, A. L. (2016). The Current State of Silicone-Based Dielectric Elastomer Transducers. *Macromolecular Rapid Communications, 37*(5), 378-413. doi:10.1002/marc.201500576

Maffli, L., Rosset, S., Ghilardi, M., Carpi, F., & Shea, H. (2015). Ultrafast All-Polymer Electrically Tunable Silicone Lenses. *Advanced Functional Materials, 25*(11), 1656-1665. doi:10.1002/adfm.201403942

Mamunya, Y. P., Valeriy, D., Pissis, P., & Lebedev, E. V. (2002). Electrical and thermal conductivity of polymers filled with metal powders. *European Polymer Journal, 38*, 1887-1897. doi:10.1016/S0014-3057(02)00064-2

Matsuhisa, N., Chen, X., Bao, Z., & Someya, T. (2019). Materials and structural designs of stretchable conductors. *Chemical Society Reviews, 48*(11), 2946-2966. doi:10.1039/C8CS00814K

Mayumi, K., Liu, C., Nakai, T., Ishida, M., Takeuchi, H., Inoue, K., . . . Ito, K. (2019). *Mechanical properties of slide-ring materials for dielectric elastomer actuators.* Paper presented at the SPIE Smart Structures + Nondestructive Evaluation.

McCoul, D., Rosset, S., Schlatter, S., & Shea, H. (2017). Inkjet 3D printing of UV and thermal cure silicone elastomers for dielectric elastomer actuators. *Smart Materials and Structures, 26*(12), 125022. doi:10.1088/1361-665x/aa9695

Mekonnen, D., Sikulskyi, S., Ren, Z., Holyoak, A., & Kim, D. (2021). Additively Manufactured Unimorph Dielectric Elastomer Actuators for Morphing Structures: Materials, Design, and Fabrication. *International Journal of Aviation, Aeronautics, and Aerospace (submitted).*

Mikkonen, R., Puistola, P., Jönkkäri, I., & Mäntysalo, M. (2020). Inkjet Printable Polydimethylsiloxane for All-Inkjet-Printed Multilayered Soft Electrical Applications. *ACS Applied Materials & Interfaces, 12*(10), 11990-11997. doi:10.1021/acsami.9b19632

Molberg, M., Crespy, D., Rupper, P., Nüesch, F., Månson, J.-A. E., Löwe, C., & Opris, D. M. (2010). High Breakdown Field Dielectric Elastomer Actuators Using Encapsulated Polyaniline as High Dielectric Constant Filler. *Advanced Functional Materials, 20*(19), 3280-3291. doi:10.1002/adfm.201000486

Nawanil, C., Makcharoen, W., Khaosa-Ard, K., Maluangnont, T., Vittayakorn, W., Isarakorn, D., & Vittayakorn, N. (2019). Electrical and dielectric properties of barium titanate – polydimethylsiloxane nanocomposite with 0-3 connectivity modified with carbon nanotube (CNT). *Integrated Ferroelectrics, 195*(1), 46-57. doi:10.1080/10584587.2019.1570043

Nguyen, C. T., Phung, H., Nguyen, T. D., Jung, H., & Choi, H. R. (2017). Multiple-degrees-of-freedom dielectric elastomer actuators for soft printable hexapod robot. *Sensors and Actuators A: Physical, 267*, 505-516. doi:10.1016/j.sna.2017.10.010

Ogden, R. W., & Hill, R. (1972). Large deformation isotropic elasticity: on the correlation of theory and experiment for compressible rubberlike solids. *Proceedings of the Royal Society of London. A. Mathematical and Physical Sciences, 328*(1575), 567-583. doi:doi:10.1098/rspa.1972.0096

Oh, J. Y., Kim, S., Baik, H.-K., & Jeong, U. (2016). Conducting Polymer Dough for Deformable Electronics. *Advanced Materials, 28*(22), 4455-4461. doi:10.1002/adma.201502947

Okuzaki, H., & Ishihara, M. (2003). Spinning and Characterization of Conducting Microfibers. *Macromolecular Rapid Communications, 24*, 261-264. doi:10.1002/marc.200390038

Panahi-Sarmad, M., Zahiri, B., & Noroozi, M. (2019). Graphene-based composite for dielectric elastomer actuator: A comprehensive review. *Sensors and Actuators A: Physical, 293*, 222-241. doi:doi.org/10.1016/j.sna.2019.05.003

Pandey, R. (2014). *Photopolymers in 3D printing applications.* (Bachelor's Thesis). Arcada, Helsinki, Finland.

Pang, H., Xu, L., Yan, D.-X., & Li, Z.-M. (2014). Conductive polymer composites with segregated structures. *Progress in Polymer Science, 39*(11), 1908-1933. doi:10.1016/j.progpolymsci.2014.07.007

Papageorgiou, D. G., Kinloch, I. A., & Young, R. J. (2015). Graphene/elastomer nanocomposites. *Carbon, 95*, 460-484. doi:10.1016/j.carbon.2015.08.055

Pasha, A., Roy, A. S., Murugendrappa, M. V., Al-Hartomy, O. A., & Khasim, S. (2016). Conductivity and dielectric properties of PEDOT-PSS doped DMSO nano composite thin films. *Journal of Materials Science: Materials in Electronics, 27*(8), 8332-8339. doi:10.1007/s10854-016-4842-5

Pei, Q., Rosenthal, M., Stanford, S., Prahlad, H., & Pelrine, R. (2004). Multiple-degrees-of-freedom electroelastomer roll actuators. *Smart Materials and Structures, 13*(5), N86-N92. doi:10.1088/0964-1726/13/5/n03

Pelrine, R., Kornbluh, R., Joseph, J., Heydt, R., Pei, Q., & Chiba, S. (2000). High-field deformation of elastomeric dielectrics for actuators. *Materials Science and Engineering: C, 11*, 89-100. doi:10.1016/S0928-4931(00)00128-4

Pelrine R, K. R. P. Q., & Joseph, J. (2000). High-speed electrically actuated elastomers with strain greater than 100%. *Science, 287*, 836. Retrieved from doi:10.1126/science.287.5454.836

Pelrine, R. E., Kornbluh, R. D., & Joseph, J. P. (1998). Electrostriction of polymer dielectrics with compliant electrodes as a means of actuation. *Sensors and Actuators A: Physical, 64*(1), 77-85. doi:10.1016/S0924-4247(97)01657-9

Phung, H., Nguyen, C. T., Jung, H., Nguyen, T. D., & Choi, H. R. (2020). Bidirectional tactile display driven by electrostatic dielectric elastomer actuator. *Smart Materials and Structures, 29*(3), 035007. doi:10.1088/1361-665x/ab675b

Pitaru, A. A., Lacombe, J. G., Cooke, M. E., Beckman, L., Steffen, T., Weber, M. H., . . . Rosenzweig, D. H. (2020). Investigating Commercial Filaments for 3D Printing of Stiff and Elastic Constructs with Ligament-Like Mechanics. *Micromachines, 11*(9). doi:10.3390/mi11090846

Poulin, A., Rosset, S., & Shea, H. R. (2015). Printing low-voltage dielectric elastomer actuators. *Applied Physics Letters, 107*(24), 244104. doi:10.1063/1.4937735

Qiu, Y., Zhang, E., Plamthottam, R., & Pei, Q. (2019). Dielectric Elastomer Artificial Muscle: Materials Innovations and Device Explorations. *Accounts of Chemical Research, 52*(2), 316-325. doi:10.1021/acs.accounts.8b00516

Ramírez, M., Parra, R., Reboredo, M., Varela, J., Castro, M. M., & Ramajo, L. (2010). Elastic modulus and hardness of CaTiO3, CaCu3Ti4O12 and CaTiO3/CaCu3Ti4O12 mixture. *Materials Letters, 64*, 1226-1228. doi:10.1016/j.matlet.2010.02.058

Risner, J. (2008). *Investigation of dielectric elastomer actuation for printable mechatronics.* (Dissertation). University of California, Berkeley, Berkeley, CA.

Rivlin, R. S., & Taylor, G. I. (1948). Large elastic deformations of isotropic materials. I. Fundamental concepts. *Philosophical Transactions of the Royal Society of London. Series A, Mathematical and Physical Sciences, 240*(822), 459-490. doi:doi:10.1098/rsta.1948.0002

Rogers, J. A. (2013). A Clear Advance in Soft Actuators. *Science, 341*(6149), 968-969. doi:10.1126/science.1243314

Romasanta, L., Leret, P., Casaban, L., Hernández, M., Rubia, M., Fernández, J., . . . Verdejo, R. (2012). Towards materials with enhanced electro-mechanical response: CaCu3Ti4O12–polydimethylsiloxane composites. *Journal of Materials Chemistry, 22*, 24705-24712. doi:10.1039/C2JM34674E

Rosenblatt-Weinberg, F. (2013). *Modelling and optimisation of Electro-Active Polymer (EAP) devices.* (Doctor of Philisiphy). Imperial College of Science, Technology and Medicine, London, UK.

Rosset, S., Araromi, O., Schlatter, S., & Shea, H. (2015). Fabrication Process of Silicone-based Dielectric Elastomer Actuators. *Journal of Visualized Experiments, 2016*. doi:10.3791/53423

Rosset, S., & Shea, H. R. (2013). Flexible and stretchable electrodes for dielectric elastomer actuators. *Applied Physics A, 110*(2), 281-307. doi:10.1007/s00339-012-7402-8

Rosseta, S., Gebbersa, P., O'Brien, B., & Shea, H. (2012). The need for speed. *Proc. of SPIE, Electroactive Polymer Actuators and Devices (EAPAD), 8340*, 834004. Retrieved from doi:10.1117/12.914623

Rossiter, J., Walters, P., & Stoimenov, B. (2009). *Printing 3D dielectric elastomer actuators for soft robotics*.

Rus, D., & Tolley, M. T. (2015). Design, fabrication and control of soft robots. *Nature, 521*(7553), 467-475. doi:10.1038/nature14543

Sakakibara, T., Izu, H., Kura, T., Shinohara, W., Iwata, H., Kiyama, S., & Tsuda, S. (1994, October 2-4). Paper presented at the IEEE 5th International Symposium on Micro Machine and Human Science.

Samarakoon, D. P., Govindaraju, N., & Singh, R. N. (2019). Dielectric Properties of Calcium Copper Titanate Ceramics Exposed to Air and Dry Nitrogen Atmospheres. *Transactions of the Indian Institute of Metals, 72*(8), 2035-2041. doi:10.1007/s12666-018-1551-1

Santiago-Alvarado, A., Cruz-Felix, A., Iturbide, F., & Licona-Morán, B. (2014). Physical-chemical properties of PDMS samples used in tunable lenses. *International Journal of Engineering Science and Innovative Technology, 3*, 563-571.

Sappati, K. k., & Bhadra, S. (2020, 25-28 May 2020). *0-3 Barium Titanate-PDMS Flexible Film for Tactile Sensing*. Paper presented at the 2020 IEEE International Instrumentation and Measurement Technology Conference (I2MTC).

Savagatrup, S., Chan, E., Renteria-Garcia, S., Printz, A., Zaretski, A., O'Connor, T., . . . Lipomi, D. (2014). Plasticization of PEDOT:PSS by Common Additives for Mechanically Robust Organic Solar Cells and Wearable Sensors. *Advanced Functional Materials, 25*. doi:10.1002/adfm.201401758

Schaffner, M., Rühs, P. A., Coulter, F., Kilcher, S., & Studart, A. R. (2017). 3D printing of bacteria into functional complex materials. *Science Advances, 3*(12), eaao6804. doi:10.1126/sciadv.aao6804

Schlatter, S., Grasso, G., Rosset, S., & Shea, H. (2020). Inkjet Printing of Complex Soft Machines with Densely Integrated Electrostatic Actuators. *Advanced Intelligent Systems, n/a*(n/a), 2000136. doi:10.1002/aisy.202000136

Schlatter, S., Rosset, S., & Shea, H. (2017). *Inkjet printing of carbon black electrodes for dielectric elastomer actuators.* Paper presented at the SPIE Smart Structures and Materials + Nondestructive Evaluation and Health Monitoring.

Schmidt, V. H., Polasik, J., Lediaev, L., & Hallenberg, J. (2005). *Actuators based on PVDF sheets with flexible PEDOT polymer electrodes.* Paper presented at the 12th International Symposium on Electrets, Salvador, Brazil.

Schönfelder, T., Kemper, F., Pohle, L., Reif, M., Tienken, M., Beckert, E., & Tünnermann, A. (2021). *Inkjet printing of dielectric layers with high relative permittivity for digital microfluidics.* Paper presented at the Microfluidics, BioMEMS, and Medical Microsystems.

Scott, J. F., Azuma, M., Paz de Araujo, C. A., McMillan, L. D., Scott, M. C., & Roberts, T. (1994). Dielectric breakdown in high-ε films for ULSI DRAMs: II. barium-strontium titanate ceramics. *Integrated Ferroelectrics, 4*(1), 61-84. doi:10.1080/10584589408018661

Sebastian, R., Michael, G., Philip, S., Philipp, T., Maximilian, L., & Jörg, F. (2016). *Aerosol-Jet-Printing silicone layers and electrodes for stacked dielectric elastomer actuators in one processing device.* Paper presented at the Proc.SPIE.

Sebastian, R., Sina, M., Florian, N., Thomas, S., Duc, P., & Jörg, F. (2020). *Accelerated aerosol-jet-printing of stretchable rGO-electrodes for stacked dielectric elastomers by using a new hybrid atomizer.* Paper presented at the Proc.SPIE.

Sekitani, T., Nakajima, H., Maeda, H., Fukushima, T., Aida, T., Hata, K., & Someya, T. (2009). Stretchable active-matrix organic light-emitting diode display using printable elastic conductors. *Nature materials, 8*, 494-499. doi:10.1038/nmat2459

Sengupta, R., Bhattacharya, M., Bandyopadhyay, S., & Bhowmick, A. K. (2011). A review on the mechanical and electrical properties of graphite and modified graphite reinforced polymer composites. *Progress in Polymer Science, 36*(5), 638-670. doi:10.1016/j.progpolymsci.2010.11.003

Sertoglu, K. (2020). nScrypt Succeeds in Microdispensing Consistent 50 Micron Dots for 3D Printed Electronics. Retrieved from https://3dprintingindustry.com/news/nscrypt-succeeds-in-microdispensing-consistent-50-micron-dots-for-3d-printed-electronics-168582/.

Shian, S., Bertoldi, K., & Clarke, D. (2015). Dielectric Elastomer Based "Grippers" for Soft Robotics. *Advanced materials (Deerfield Beach, Fla.), 27*. doi:10.1002/adma.201503078

Shigemune, H., Sugano, S., Nishitani, J., Yamauchi, M., Hosoya, N., Hashimoto, S., & Maeda, S. (2018). Dielectric Elastomer Actuators with Carbon Nanotube Electrodes Painted with a Soft Brush. *Actuators, 7*(3), 51.

Shintake, J., Cacucciolo, V., Floreano, D., & Shea, H. (2018). Soft Robotic Grippers. *Advanced Materials*, 1707035. doi:10.1002/adma.201707035

Shintake, J., Matsuno, K., Baba, K., & Takeuchi, H. (2019). *Characterization of dielectric elastomer actuators made of slide ring materials.* Paper presented at the SPIE Smart Structures + Nondestructive Evaluation.

Shintake, J., Rosset, S., Schubert, B., Floreano, D., & Shea, H. (2016). Versatile Soft Grippers with Intrinsic Electroadhesion Based on Multifunctional Polymer Actuators. *Advanced Materials, 28*(2), 231-238. doi:10.1002/adma.201504264

Shintake, J., Schubert, B., Rosset, S., Shea, H., & Floreano, D. (2015, 28 Sept.-2 Oct. 2015). *Variable stiffness actuator for soft robotics using dielectric elastomer and low-melting-point alloy.* Paper presented at the 2015 IEEE/RSJ International Conference on Intelligent Robots and Systems (IROS).

Shintake, J., Shea, H., & Floreano, D. (2016, 9-14 Oct. 2016). *Biomimetic underwater robots based on dielectric elastomer actuators.* Paper presented at the 2016 IEEE/RSJ International Conference on Intelligent Robots and Systems (IROS).

Shrestha, M., Lu, Z., & Lau, G. K. (2018). Transparent Tunable Acoustic Absorber Membrane Using Inkjet-Printed PEDOT:PSS Thin-Film Compliant Electrodes. *ACS Applied Materials & Interfaces, 10*. doi:10.1021/acsami.8b12368

Sikulskyi, S., Mekonnen, D. T., El Atrache, A., Divo, E., & Kim, D. (2021). Effects of Ferroelectric Fillers on Composite Dielectric Elastomer Actuator. *Actuators, 10*(7), 137.

Sikulskyi, S., Yu, S. L., Rojas-Nastrucci, E., & Kim, D. (2021). *On the electrode-elastomer patterns in dielectric elastomer actuator motion.* Paper presented at the SPIE Smart Structures + Nondestructive Evaluation.

Sikulskyi, S., Yu, S. L., Rojas-Nastrucci, E., Park, J., & Kim, D. (2020). *Soft and printable electrodes for flexible elastomer actuators.* Paper presented at the SPIE Smart Structures + Nondestructive Evaluation.

Sim, K., Rao, Z., Ershad, F., & Yu, C. (2020). Rubbery Electronics Fully Made of Stretchable Elastomeric Electronic Materials. *Advanced Materials, 32*(15), 1902417. doi:10.1002/adma.201902417

Sommer-Larsen, P., & Larsen, A. (2004). *Materials for dielectric elastomer actuators.* Paper presented at the Smart Structures and Materials.

Son, S., Pugal, D., Hwang, T., Choi, H., Koo, J., Lee, Y., . . . Nam, J.-D. (2012). Electromechanically driven variable-focus lens based on transparent dielectric elastomer. *Applied optics, 51*, 2987-2996. doi:10.1364/AO.51.002987

Spitalsky, Z., Tasis, D., Papagelis, K., & Galiotis, C. (2010). Carbon nanotube–polymer composites: Chemistry, processing, mechanical and electrical properties. *Progress in Polymer Science, 35*(3), 357-401. doi:10.1016/j.progpolymsci.2009.09.003

Srinivasaraghavan Govindarajan, R., Xu, X., Sikulskyi, S., Madiyar, F., Rojas-Nastrucci, E., & Kim, D. (2021). *Additive manufacturing of flexible nanocomposite SAW sensor for strain detection.* Paper presented at the SPIE Smart Structures + Nondestructive Evaluation.

Subramanian, M., Li, D., Duan, N., Reisner, B., & Sleight, A. (2000). High dielectric constant in a ACu3Ti4O12 and ACu3Ti3FeO12 phases. *Journal of Solid State Chemistry - J SOLID STATE CHEM, 151*, 323-325. doi:10.1006/jssc.2000.8703

Sun, K., Zhang, S., Li, P., Xia, Y., Zhang, X., Du, D., . . . Ouyang, J. (2015). Review on application of PEDOTs and PEDOT:PSS in energy conversion and storage devices. *Journal of Materials Science: Materials in Electronics, 26*(7), 4438-4462. doi:10.1007/s10854-015-2895-5

Suo, Z. (2010). Theory of Dielectric elastomers. *Acta Mech. Solida Sin., 23*, 549. Retrieved from doi:10.1016/S0894-9166(11)60004-9

Tang, Z., Wu, K., Huang, Y., & Li, J. (2017). High Breakdown Field CaCu3Ti4O12 Ceramics: Roles of the Secondary Phase and of Sr Doping. *Energies, 10*, 1031. doi:10.3390/en10071031

Teng, C., Lu, X., Zhu, Y., Wan, M., & Jiang, L. (2013). Polymer in situ embedding for highly flexible, stretchable and water stable PEDOT:PSS composite conductors. *RSC Adv., 3*, 7219-7223. doi:10.1039/C3RA41124A

Teng, H. (2010). Stiffness properties of particulate composites containing debonded particles. *International Journal of Solids and Structures, 47*(17), 2191-2200. doi:doi.org/10.1016/j.ijsolstr.2010.04.004

Treloar, L. R. G. (1975). *The Physics of Rubber Elasticity*: Oxford University Press, USA.

Tunkasiri, T., & Rujijanagul, G. (1996). Dielectric strength of fine grained barium titanate ceramics. *Journal of Materials Science Letters, 15*(20), 1767-1769. doi:10.1007/BF00275336

Vaicekauskaite, J., Mazurek, P., Vudayagiri, S., & Ladegaard Skov, A. (2019). *Silicone elastomer map: design the ideal elastomer.* Paper presented at the SPIE Smart Structures + Nondestructive Evaluation.

Vudayagiri, S., & Skov, A. L. (2014). Methods to ease the release of thin polydimethylsiloxane films from difficult substrates. *Polymers for Advanced Technologies, 25*, 249. Retrieved from doi:10.1002/pat.v25.3

Vudayagiri, S., Zakaria, S., Yu, L., Hassouneh, S., Benslimane, M., & Skov, A. (2014). High breakdown-strength composites from liquid silicone rubbers. *Smart Materials and Structures, 23*, 105017. doi:10.1088/0964-1726/23/10/105017

Wan, W., Luo, J., Huang, C.-e., Yang, J., Feng, Y., Yuan, W.-X., . . . Qiu, T. (2017). Calcium copper titanate/polyurethane composite films with high dielectric constant, low dielectric loss and super flexibility. *Ceramics International*. doi:10.1016/j.ceramint.2017.12.108

Wang, G., Zhang, Y., Duan, L., Ding, K., Wang, Z., & Zhang, M. (2015). Property reinforcement of silicone dielectric elastomers filled with self-prepared calcium copper titanate particles. *Journal of Applied Polymer Science, 132*, n/a-n/a. doi:10.1002/app.42613

Wang, J., Chao, X., Li, G., Feng, L., & Zhao, K. (2016). Fabrication and enhanced characterization of copper powder filled copper calcium titanate/poly(vinylidene difluoride) composite. *Journal of Materials Science: Materials in Electronics, 28*, 1-5. doi:10.1007/s10854-016-6204-8

Wang, Q.-M., & Cross, L. E. (1998). Performance analysis of piezoelectric cantilever bending actuators. *Ferroelectrics, 215*(1), 187-213. doi:10.1080/00150199808229562

Wang, Y., Zhu, C., Pfattner, R., Yan, H., Jin, L., Chen, S., . . . Bao, Z. (2017). A highly stretchable, transparent, and conductive polymer. *Science Advances, 3*(3), e1602076. doi:10.1126/sciadv.1602076

Wang, Z., Keith Nelson, J., Hillborg, H., Zhao, S., & Schadler, L. S. (2013). Dielectric constant and breakdown strength of polymer composites with high aspect ratio fillers studied by finite element models. *Composites Science and Technology, 76*, 29-36. doi:doi.org/10.1016/j.compscitech.2012.12.014

White, J. R., & De, S. K. (2001). *Rubber Technologist's Handbook*: Smithers Rapra Publishing.

WHO. (1999) Hazard prevention and control in the work environment: : airborne dust. In, *Occupational and environmental health series*. Geneva: World Health Organization, Occupational and Environmental Health, Team.

Wilkinson, N. J., Lukic-Mann, M., Shuttleworth, M. P., Kay, R. W., & Harris, R. A. (2019, 14-18 April 2019). *Aerosol Jet Printing for the Manufacture of Soft Robotic Devices.* Paper presented at the 2019 2nd IEEE International Conference on Soft Robotics (RoboSoft).

Wilkinson, N. J., Smith, M. A. A., Kay, R. W., & Harris, R. A. (2019). A review of aerosol jet printing—a non-traditional hybrid process for micro-manufacturing. *The International Journal of Advanced Manufacturing Technology, 105*(11), 4599-4619. doi:10.1007/s00170-019-03438-2

Wilson, K., Jordan, J., Henke, E.-F. M., Slipher, G., Rosset, S., & Anderson, I. (2019, 03.20.2021). *Ink-jet printed conductive and semi-conductive rubber for dielectric elastomer devices.* Paper presented at the SPIE Smart Structures + Nondestructive Evaluation.

Wissler, M., & Mazza, E. (2005a). Modeling and simulation of dielectric elastomer actuators. *Smart Materials and Structures, 14*(6), 1396-1402. doi:10.1088/0964-1726/14/6/032

Wissler, M., & Mazza, E. (2005b). Modeling of a pre-strained circular actuator made of dielectric elastomers. *Sensors and Actuators A: Physical, 120*(1), 184-192. doi:doi.org/10.1016/j.sna.2004.11.015

Wu, W. (2019). Stretchable electronics: functional materials, fabrication strategies and applications. *Science and Technology of Advanced Materials, 20*(1), 187-224. doi:10.1080/14686996.2018.1549460

Yang, X., Hu, J., Chen, S., & Jinliang, H. (2016). Understanding the Percolation Characteristics of Nonlinear Composite Dielectrics. *Scientific Reports, 6*, 30597. doi:10.1038/srep30597

Yeoh, O. H. (1990). Characterization of Elastic Properties of Carbon-Black-Filled Rubber Vulcanizates. *Rubber Chemistry and Technology, 63*(5), 792-805. doi:10.5254/1.3538289

Yoon, S.-S., & Khang, D.-Y. (2016). Roles of Nonionic Surfactant Additives in PEDOT:PSS Thin Films. *The Journal of Physical Chemistry C, 120*. doi:10.1021/acs.jpcc.6b12043

Yu, L., Madsen, F., Hvilsted, S., & Skov, A. (2015). Dielectric elastomers, with very high dielectric permittivity, based on silicone and ionic interpenetrating networks. *RSC Adv., 5*. doi:10.1039/C5RA07375H

Yun, S., Park, S., Park, B., Nam, S., Park, S. K., & Kyung, K.-U. (2015). A thin film active-lens with translational control for dynamically programmable optical zoom. *Applied Physics Letters, 107*(8), 081907. doi:10.1063/1.4929716

Zhang, J., Liu, L., & Chen, H. (2020). Electromechanical properties of soft dissipative dielectric elastomer actuators influenced by electrode thickness and conductivity. *Journal of Applied Physics, 127*(18), 184902. doi:10.1063/5.0001580

Zhang, Q. M., & Serpe, M. J. (2017). Stimuli-Responsive Polymers for Actuation. *Chemphyschem : a European journal of chemical physics and physical chemistry, 18*(11), 1451-1465. doi:10.1002/cphc.201601187

Zhang, W. (2007). Carbon based conductive polymer composites. *Journal of materials science, v. 42*(no. 10), pp. 3408-3418-2007 v.3442 no.3410. doi:10.1007/s10853-007-1688-5

Zhang, Y.-Y., Min, Y., Wang, G.-L., Wang, Z.-F., Junliang, L., Luo, Z.-W., & Zhang, M. (2019). Design and properties of calcium copper titanate/poly(dimethyl siloxane) dielectric elastomer composites. *Rare Metals*. doi:10.1007/s12598-018-1186-8

Zhang, Y. Y., Wang, G. L., Zhang, J., Ding, K. H., Wang, Z. F., & Zhang, M. (2019). Preparation and properties of core-shell structured calcium copper titanate@polyaniline/silicone dielectric elastomer actuators. *Polymer Composites, 40*(S1), E62-E68. doi:10.1002/pc.24479

Zhao, J., Wang, S., McCoul, D., Xing, Z., Huang, B., Liu, L., & Leng, J. (2016). Bistable dielectric elastomer minimum energy structures. *Smart Materials and Structures, 25*(7), 075016. doi:10.1088/0964-1726/25/7/075016

Zhou, L., & Jiang, Y. (2020). Recent progress in dielectric nanocomposites. *Materials Science and Technology, 36*(1), 1-16. doi:10.1080/02670836.2019.1675335

Zolfagharian, A., Kouzani, A., Khoo, S., Amiri, A., Amiri Moghadam, A. A., Gibson, I., & Kaynak, A. (2016). Evolution of 3D printed soft actuators. *Sensors and Actuators A: Physical, 250*, 258-272. doi:10.1016/j.sna.2016.09.028

LIST OF PUBLICATIONS

Book Chapter:

Kim, D., Sikulskyi, S. (2021). 4D-printed Dielectric Elastomer Soft Robots: Modeling and Fabrications. In Bodaghi, M., Zolfagharian, A. 4D-Printed Smart Materials and Structures. *Elsevier (accepted)*

Journal Publications:

Sikulskyi, S., Mekonnen, D. T., El Atrache, A., Divo, E., & Kim, D. (2021). Effects of Ferroelectric Fillers on Composite Dielectric Elastomer Actuator. Actuators, 10(7), 137.

Sikulskyi, S., Malik, A., & Kim, D. (2021). Magnetorheological Fluid Filled Spring for Variable Stiffness and Damping: Current and Potential Performance. *Smart Materials and Structures (submitted).*

Conference Proceedings:

Sikulskyi, S., Yu, S. L., Rojas-Nastrucci, E., & Kim, D. (2021). On the electrode-elastomer patterns in dielectric elastomer actuator motion. Paper presented at the SPIE Smart Structures + Nondestructive Evaluation.

Srinivasaraghavan Govindarajan, R., Xu, X., Sikulskyi, S., Madiyar, F., Rojas-Nastrucci, E., & Kim, D. (2021). Additive manufacturing of flexible nanocomposite SAW sensor for strain detection. Paper presented at the SPIE Smart Structures + Nondestructive Evaluation.

Sikulskyi, S., Yu, S. L., Rojas-Nastrucci, E., Park, J., & Kim, D. (2020). Soft and printable electrodes for flexible elastomer actuators. Paper presented at the SPIE Smart Structures + Nondestructive Evaluation.

Sikulskyi, S., & Kim, D. (2019). Force optimization and numerical validation of helical dielectric elastomer actuator. Paper presented at the SPIE Smart Structures + Nondestructive Evaluation.

Park, J., Sikulskyi, S., Kim, D., Divo, E., & Martinez, R. (2019). Numerical studies on origami dielectric elastomer actuator using Kresling pattern. Paper presented at the SPIE Smart Structures + Nondestructive Evaluation.

Conference Presentations:

Mekonnen, D., Sikulskyi, S., Ren, Z., Holyoak, A., & Kim, D. (2021). Realizing Wing Morphology Through Additive Manufacturing of Soft and Smart Actuators. *National Council of Undergraduate Research (NCUR).*

Mekonnen, D., Sikulskyi, S., Ren, Z., Holyoak, A., & Kim, D. (2021). Bending Dielectric Elastomer Actuators for Additively Manufactured Morphing Structures. *Florida Undergraduate Research Conference (FURC).*

Mekonnen, D., Sikulskyi, S., Ren, Z., Holyoak, A., & Kim, D. (2020). Additively Manufactured Morphing Structures with Embedded Smart Actuators. *ERAU Student Research Symposium (SRS).*

Sikulskyi, S., Kim, D., & Zhao, Y. (2018). On the Performance of Soft Active Composites with Helical Dielectric Elastomer *Actuators. 26th Annual International Conference on Composites/Nano Engineering (ICCE-26).*